COMPUTATIONAL MODELLING OF LIQUID JET IMPINGEMENT ONTO HEATED SURFACE

Vom Fachbereich Maschinenbau
an der Technischen Universität Darmstadt
zur
Erlangung des Grades eines Doktor-Ingenieurs
(Dr.-Ing.)
genehmigte

Dissertation

vorgelegt von

Maharshi Subhash, M. Tech
from Dehradun, India

Berichterstatter:	Prof. Dr.-Ing. habil. Cameron Tropea
Mitberichterstatter:	apl. Prof. Dr.-Ing. habil. Suad Jakirlic
	apl. Prof. Dr. rer. Nat. Amsini Sadiki
Tag der Einreichung:	30th November, 2015
Tag der mündlichen Prüfung:	17th February, 2016

Darmstadt 2017
D17

Erklärung

Hiermit erkläre ich, dass ich die vorliegende Dissertation selbstständig verfasst und nur die angegebenen Hilfsmittel an den entsprechend gekennzeichneten Stellen verwendet habe. Ich habe bisher noch keinen Promotionsversuch unternommen.

Dehradun, im November 2015

Subhash

Maharshi Subhash

Dedicated to
my supervisor and co-supervisor

Prof. Dr. Ing.Cameron Tropea ,

apl. Prof. Dr. Ing. Suad Jakirlic

and

my parents, my wife Sudha and daughter
Samriddhi

Foreword

One of the joys of completion is to look over the journey past and remember all those, who had helped and supported along this long but fulfilling road. This Ph.D. thesis is the result of a challenging journey, upon which many people have contributed and given their supports.

It would not have been possible without the help, support, and patience of my mentor Prof. Jakirlic, not to mention his advice and unsurpassed knowledge of numerical simulation and turbulence model. My sincere gratitude to my Prof. and head of the Institute, Prof. Tropea for giving the opportunity of research on ‘Computational Modelling of Liquid Jet Impingement onto Heated Surface.' The present work was accomplished during the period June 2008 to March 2012.

This work has been financially supported by the steel company Dillinger Hütte, GTS. The fruitful discussion with research and development head of the company Prof. Karl-Hermann Tacke and other members of research committee Dr. Roland Schorr, Mr. Eberwein Klaus, and Mr. Kirsh Hans-Juergen during the project meeting encouraged me a lot. The fruitful discussion with Dr. Karwa and Prof. Stephan from Institute of Technical Thermodynamics (TTD) brought this research at the good level in terms of findings.

Throughout this research work, the enumerable help from co-supervisor enhanced the quality of the results.

During the research work, time-to-time discussion with Prof. Sadiki helped me to understand the computational error.

I also express gratitude to Dr. Basara the head of Advanced Simulation Technology from AVL List Company, Graz Austria, for providing the CFD code AVL Fire. Thanks to Mr. David Greif, who helped me to learn the tools of this code.

Also, the time-to-time discussion with Dr.-Ing. Ilia Roisman helped to understand the theoretical aspects of the film-boiling model.

Other colleagues Mrs. Gisa Kadavelil, Dr. Samual Chang, Dr. Robert Maduta and others helped me to work with some software tools. Sometimes, Mr. Michael Kron (computer administrator), provided extra computation time which helped me to produce the results for those cases which consumed large computing time.

Mrs. Lath and Mrs. Neuthe had offered great support during my stay in Darmstadt.

Moreover, co-supervisor’s consistent patience on me has created a humble and eternal respect towards him for rest of my life.

At last, but not least, I would like to express my deep respect and love to my parents and my family members for great moral support during the research.

Maharshi Subhash

8

Abstract

Quenching of heated surfaces through impinging liquid jets is of great importance for numerous applications like steel processing, nuclear power plants, automobile industries, etc. Therefore, computational modelling of the surface quenching through circular water jets impinging normally onto a heated flat surface has vital importance in order to reveal the physics of the quenching process.

At first, a numerical model was developed for single jet impingement process. A conjugate heat transfer problem was solved implying consideration of both regions, one occupied by fluid (multi-phase flow consisting of water, vapor and ambient air) and one accommodating the solid surface within the same solution domain.

Numerical simulations were performed in a range of relevant operating parameters: jet velocities (2.5, 5, 7.5 and 10 m/s), water sub-cooling (75 K) and wall-superheat (650 K - 800 K) corresponding closely to those encountered in the industrial water jet cooling banks. Due to the high initial temperature of the surface, the boiling process exhibits strong spatial and temporal fluctuations. Its effect on the boundary layer profiles at the stagnation region at different time intervals are analyzed. The analysis reveals a highly distorted field of both mean flow and turbulence quantities. It represents an important outcome, also with respect to appropriate model improvements. The different boiling characteristics are envisaged in detail to increase the level of understanding of the phenomena. The influence of the turbulent kinetic energy investigated at the boiling front as well as the jet-acceleration region has been studied. The physically relevant results are obtained and analyzed along with reference database provided experimentally by Karwa (2012, '*Experimental Study of Water Jet Impingement Cooling of Hot Steel Plates*,' Dissertation, FG TTD, TU Darmstadt). The intensive quenching process is consistent with the high rate of sub-cooling and high jet velocities. The surface temperature predicted by quenching model within the impingement region and the subsequent wall-jet region agrees reasonably well with the measurements, the outcome being particularly valid at higher jet velocities. However, a steep temperature gradient at the position corresponding to boiling threshold has not been captured under the condition of the numerical grid adopted. On the other hand, a reasonably good prediction of the wetting front propagation phenomena advocates the future development of the model. The high-intensity back motion of the vapor phase in the stagnation region at the earlier times of the water jet impingement can induce an appropriately high turbulence level, which could be accounted well by the turbulence model applied.

The second part of the present work deals with multiple liquid jet impingement. When the multiple jets impact onto the heated surface, the heat flux is extracted from the surface by the mass flow rate. The heat flux is dependent on the several flow conditions and configurations of the nozzle array system. Therefore, one needs to study the nozzle array configuration along with several flow parameters for the better design of the cooling header system. Accordingly, the hydrodynamics of the multiple jets has been studied computationally realizing the need for optimum configuration of the nozzle array. The effects of the mass flow rate, target plate width and the turbulence produced due to the impingement were studied. Afterward, an analytical model is proposed for the quenching of the multiple jets system. It has been realized that, when jet impinges onto the surface at very high initial temperature, the film boiling may play a role in the heat transfer mechanism. Therefore, development has been made in the film-boiling model considering the effect of turbulence at the liquid jet stagnation region at the Leidenfrost point. The Leidenfrost point is the minimum temperature at which the film boiling can sustain. However, the vapor-liquid interface has the dynamic character; it oscillates with high frequency and causes the additional momentum diffusivity. Therefore, the need for introducing the effect of associated turbulence has been felt. The length and velocity scale of the turbulent structure has been approximated by assuming homogeneous turbulence. The new model for the heat flux and wall superheat yielded results agreeing well with published experimental results.

Zusammenfassung

(„Numerische Modellierung des Aufpralls von Flüssigkeitsstrahlen auf beheizte Oberflächen“)

Kühlung der beheizten Oberflächen durch aufprallende Flüssigkeitsstrahlen ist im Fall zahlreicher industrieller Anwendungen von großer Bedeutung: Stahlherstellung, Kernenergiekraftwerke, Fahrzeugindustrie, usw. Das Stellt die Hauptmotivation der vorliegenden Arbeit dar, die die numerische Modellierung der Kühlung von heißen Oberflächen durch runde, senkrecht auf die Fläche aufprallende Wasserstrahlen umfasst.

Zuerst wurde der Aufprall eines einzelnen Wasserstrahls (‘*single jet impingement*’) modelliert. Es wurde ein gekoppeltes Wärmeübertragungsproblem behandelt, indem beide Teilgebiete, das Flüssigkeit (d.h. mehrphasige, das Wasser, den Dampf und die umgebende Luft charakterisierende Strömung) und die feste Wand umfassend, innerhalb des gleichen Lösungsgebietes berücksichtigt wurden. Numerische Simulationen wurden im Bereich der relevanten Arbeitsparameter, bezogen auf Strahlgeschwindigkeiten (2.5, 5, 7.5, 10 *m/s*), Wasserunterkühlungstemperaturen von 75 *K* (*Water subcooling*) und Wandüberhitzungstemperaturen von 650 *K* bis 800 *K* (*wall superheat*), durchgeführt. Diese entsprechen den Betriebsbedingungen der in der industriellen Praxis anzutreffenden Kühlungsanlagen. Infolge der großen Anfangstemperatur der Oberfläche wird das Siedeprozess von starken räumlichen und zeitlichen Schwankungen begleitet. Das beeinflusst entscheidend das temporäre Verhalten der wandnahen Grenzschicht. Die ausführlich durchgeführte Analyse offenbart stark modifizierte Felder der Hauptströmung und der turbulenten Größen. Das stellt eine wichtige Erkenntnis dar, womit ein Beitrag zum weiteren Verständnis des vorliegenden Phänomens geleistet werden konnte. Dabei wurde große Aufmerksamkeit dem Einfluss der kinetischen Turbulenzenergie im Gebiet der Strömungsbeschleunigung geschenkt. Physikalisch relevante Ergebnisse wurden gewonnen und mit der Datenbasis des komplementären, von Karwa durchgeführten Experimenten (2012, ‘*Experimental Study of Water Jet Impingement Cooling of Hot Steel Plate*’, Dissertation, FG TTD, TU Darmstadt) direkt verglichen. Grundlegend betrachtet ist der Kühlungsprozess der glühend heißen Stahlplatte konsistent mit der Intensität der Wärmeabfuhr infolge höher Aufprallgeschwindigkeiten. Die mit dem vorliegenden Berechnungsmodell für die Erfassung der Stahlabkühlung wurden die Ergebnisse gewonnen, die eine gute Übereinstimmung mit den experimentellen Daten im Aufprallgebiet aufweisen; dies trifft insbesondere im Fall höhere Aufprallgeschwindigkeiten zu. Allerdings wurde der steile Temperaturgradient an der der Siedeschwelle (‘*boiling threshold*’) entsprechenden Wandposition unter Bedingungen der verwendeten räumlichen Auflösung nicht erfasst. Trotzdem wurde die Ausbreitung der benetzten Front korrekt vorhergesagt, was für das hohe Potential des Modells im Fall praktischer

Anwendungen spricht. Die intensive Rückströmung innerhalb der Dampfphase im Aufprallgebiet und der damit verbundene Anstieg der Turbulenzintensität im Aufprallgebiet konnten mit dem eingesetzten Turbulenzmodell wiedergegeben werden.
Der Zweite Teil der vorliegenden Arbeit untersucht die Effekte von mehreren, parallel angeordneten, gleichzeitig aufprallenden Wasserstrahlen (*'multiple jets impingement'*). Der im Fall mehrerer auf die beheizte Oberfläche aufprallender Strahlen abgeführte Wärmefluss hängt von unterschiedlichen Strömungsparametern aber auch von der Düsenkonfiguration ab, deren verschiedene Anordnungen eines der Ziele der Untersuchung darstellen. Diesbezüglich lag der Schwerpunkt auf der Hydrodynamik des mehrfachen Aufpralls. Der Wasser-Volumenstrom im Hinblick auf unterschiedliche Anzahl der Düsen sowie die Abmessungen der Platte wurden variiert. Anschließend wurde ein analytisches Modell für die Oberflächenabkühlung formuliert, das als Grundlage das Phänomen der '*film boiling*' Prozesse betrachtet. Die Effekte der Turbulenz unter Bedingungen des sog. Leidenfrost Phänomens wurden am Staugebiet berücksichtigt. Das Dampf-Flüssig Interface weist einen dynamischen Charakter auf, indem es mit entsprechend hoher Frequenz oszilliert, was als Folge einen zusätzlichen Impulstransport hat. Dabei wurden die turbulenten Längen- und Geschwindigkeitsmaßstäbe durch die Annahme homogener Turbulenz approximiert. Das neue, den Wärmefluss und die Wandüberhitzung berücksichtigende Modell resultiert in einer guten Übereinstimmung mit den in der veröffentlichten Literatur verfügbaren Ergebnissen.

Table of Contents

Nomenclature

A	constant of shape function
A	area, m^2
C_A	closure coefficient, (Ch. 3)
C_D	coefficient of drag, (Eq. 3.37)
C_m	vapor formation
C_1	constant of length scale
C_2	constant of wave number
C_p	specific heat capacity at constant pressure, *J/(kgK)*
d	diameter, *m*
D	steel plate diameter, *m*
D_b	bubble diameter, *m* (Ch. 3)
D_s	substrate diameter, *m* (Eq. 2.8)
F	force vector, *N*
f	volume fraction of liquid or vapour
g	gravity, m/s^2
H	enthalpy, *J*
$\langle H_{k,}\rangle^k$	intrinsic volume-averaged enthalpy of the k^{th} phase at the interface, *J* (Eq. 3.42)
Δh_{evap}	latent heat, *J/kg* (Ch.2)
H_s	enthalpy of solid material, *J* (Eq. 3.49)
h	heat transfer coefficient, $J/(m^2K)$
h_{fg}	latent heat of vaporization, *J/kg*
h_n	nozzle to plate spacing, *m*
I	identity tensor
i	complex number
Ja	Jacob number, $Ja = C_{pl}(T_w - T_{sat})/h_{fg}$
J_i	mass flux of i^{th} species relative to mass-averaged velocity, $kg/(m^2s)$
k	thermal conductivity, *W/(mK)*(ch. 2), wave number, m^{-1}
K_{chf}	transient critical heat flux factor, (Ch. 3)

K_{mhf}	transient minimum heat flux factor (Ch. 3)
l	wave length, *m*
L	latent heat of phase transition (Eq. 2.4)
$\dot{m}$	mass source per unit volume
$M_{e,}$	momentum exchange coefficient between phases *j* and *k* (Eq. 3.36)
$\hat{n}$	unit normal vector
p	pressure, N/m^2
P	mean pressure, N/m^2
Pe	Peclet number, $Pe=Re\times Pr$,
Pr	Prandtl number,$Pr=\mu Cp/k$
$\dot{q}$	heat flux, W/m^2 (Ch. 2)
q_k	heat flux vector, W/m^2 (Eq. 3.41)
q_k^t	turbulent heat flux vector, W/m^2 (Eq. 3.41)
Q	heat flux, W/m^2 (Ch. 3)
r	radial coordinate, radius, *m* (Ch.2)
R	radius of curvature, *m*
Re_b	Reynolds number of vapor bubble (Eq. 3.39)
R_g	Individual gas constant (Eq. 2.4)
$\dot{R}(t)$	Bubble growth rate, *m/s* (Eq. 2.4)
Re	Reynolds number, $Re=U_jd/\nu$
r_n	nozzle radius, $r_n=d_n/2$, *m*
t	time, *s*
T	temperature, *K*
T_0	saturation temperature at the static pressure, *K* (Eq. 2.4)
T_{sat}	saturation temperature of liquid (water), *K*
T_{tls}	thermodynamic limit of liquid superheat, *K* (*Ch. 2*)
$(\Delta T_w)_{fc}$	wall temperature at film collapse, *K*
ΔT_{sat}	wall superheat, $\Delta T_{sat}=T_w-T_{sat}$, *K*
ΔT_{sub}	liquid (water) sub-cooling, $\Delta T_{sub}=T_{sat}-T_l$, *K*
T_w	wall temperature, *K*

T_∞	ambient temperature, K
u	velocity of fluid in x or r direction, m/s
u_j	jet velocity, m/s
u_s	surface velocity, m/s
v	velocity of fluid normal to the surface, m/s
V	velocity, m/s
V	*volume,* m^3, (Ch. 3)
$\vec{V}$	velocity vector, m/s
$\Delta\vartheta$	volume element for volume average, m^3
w_p	wetting parameter (Eq. 3.24)
y	normal-to-wall coordinate
$\Delta\theta_{sat}$	wall superheat=$\theta_w - \theta_{sat}$, K (Ch. 2)
$\Delta\theta_{sub}$	liquid sub-cooling=$\theta_{sat} - \theta_l$, K (Ch. 2)

Greek Symbols

α	thermal diffusivity of fluid, m^2/s, volume fraction,(Ch. 3)
β	evaporation – condensation coefficient (Eq. 2.4)
γ	total acceleration of fluid, m^2/s
δ	thickness, liquid layer thickness (Ch. 2), m
ε	volume fraction, momentum diffusivity by turbulent, m^2/s
ε_d	dispersed phase volume, m^3 (Ch. 3)
ε^+	non-dimensional effective diffusivity [-](Ch. 2)
ζ	shape function,
θ	azimuthal coordinate, temperature, K
λ	thermal conductivity, W/mK
μ	dynamic viscosity, $kg/m.s$
ρ	density, kg/m^3
ρ_i	density of i^{th} species
σ	surface tension, N/m
Π	number of different phases, (Ch. 3)
τ	shear stress tensor, N/m^2

ϕ	arbitrary property function, (Ch. 3)
Φ	arbitrary property function, (Ch. 3)
$\bar{\Phi}$	time average of property function, (Ch. 3)
Ψ	arbitrary property function, (Ch. 3)
Ω	arbitrary property function, (Ch. 3)
∇	Laplace operator vector
$\Im$	Laplacian filter
ν	kinematic viscosity, m^2/s,
ω	wave frequency, s^{-1}

Subscripts

c	continuous phase, critical
cb	convective boiling
CHF	Critical Heat flux
crit	critical
d	disperse phase
i	i^{th} component
I	interface
j	jet
k	k^{th} phase in multiphase system
l	liquid
m	momentum
min	minimum
p	plate
sat	saturation state
v	vapour phase
v	vapour
w	wall
w	wall
t	turbulent, thermal

Superscripts

k	phase index
n	normal component
t	tangential component,
′	perturbed function
^	base magnitude of perturbed function

Others

$\langle \ \rangle$	volume averaged
$\langle \ \rangle^k$	phase average

List of Abbreviations

AMG	Algebraic Multi-Grid method
CBC	Convection Boundedness Criteria
CDS	Central Difference Scheme
CFD	Computational Fluid Dynamics
CHF	Critical Heat Flux
LDV	Laser Doppler Velocimetry
LUDS	Linear Upwind Difference Scheme
MHF	Minimum Heat Flux
RANS	Reynolds-Averaged Navier-Stokes
ROT	Run-Out-Table
SIMPLE	Semi-Implicit Method for Pressure Linked Equation
SPMD	Single Program Multiple Data
TKE	Turbulent Kinetic Energy
UDS	Upwind Differencing Scheme
URANS	Unsteady Reynolds-Averaged Navier-Stokes
VOF	Volume-of-Fluid, Volume-of-fraction

1. Introduction and Motivation

Surface quenching through liquid jets have ample applications in different industrial branches such as steel processing (see e.g., Figure 1 and 2), nuclear power plants and automobile industry [Gradeck et al., (2009), Biswas et al., (1997), Hatta et al., (1989), Cho et al., (2008), Pan and Webb (1995), Rivallin and Viannay (2001), Liu et al., (2002)].

Figure 1– Process of jet cooling of Run-out-Table (ROT) [Gradeck et al., (2009)]

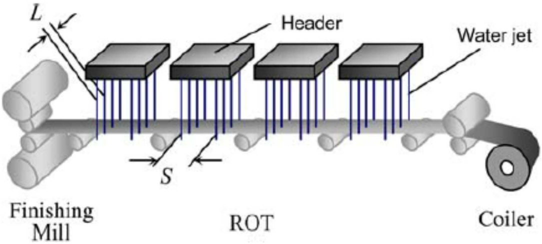

Figure 2 – Schematic diagram of the ROT cooling Process [Cho et al., (2008)]

Especially, the material properties of rolled-steel-slab depend upon the process and types of quenching. Generally, water jets are used for quenching the heated surface (800-1000 ^{o}C) which is accompanied with the different heat transfer mechanisms, such as nucleate boiling, transition boiling and film boiling. Various boiling phenomena exhibit various characteristics; see e.g. the Nukiyama Curve [Nukiyama (1934)].

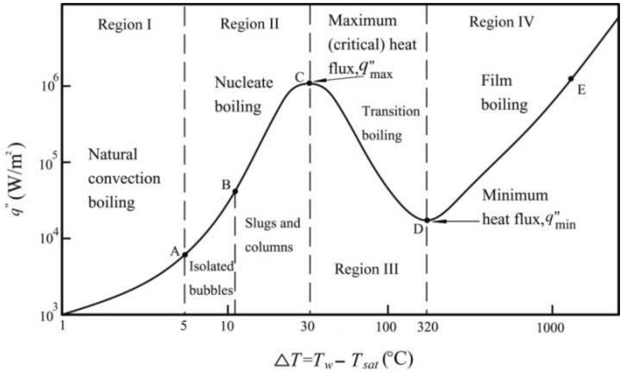

Figure 3 – Pool boiling curve [50]

Accordingly, Figure 3 shows the characteristics of the pool boiling phenomena, which is important in understanding the basics of boiling. The Region I depicts the natural convection up to the 5 K superheat of the surface up to point A in the curve. From point A to C the nucleate boiling regime takes place. Further, this part has been divided into two sections. From A to B, corresponding to the wall superheat ranging from 5 K to 11 K, isolated bubbles are generated. Due to the low wall superheat, only very few nucleation sites become activated to beget the bubbles; hence, the bubble number density is reduced. When the wall superheat is increased to 30 K, from B to C in the diagram, more nucleation sites become activated, and the density of the bubbles increases – the bubbles merge forming slugs and columns of bubbles. Consequently, it enhances the heat flux exhibiting a high rate, in comparison to natural convection and low wall superheat nucleate boiling.

The further increment of the wall superheat causes the destabilization of the slug and columns, which activates an explosion of the bubbles, and an enormous amount of vapor evolves from this process. Hence the residence time of the liquid wettability decreases. This phenomenon is so transient that it exhibits nucleate and film boiling phenomena intermittently. In this way, the heat transfer rate decreases. The Region III from C to D in the above diagram shows this phenomenon.

If the wall superheat further increases, a significant amount of vapor is generated preventing consequently the contact of the liquid to the surface; the corresponding point in the diagram is D at 320 K of superheat for the transition boiling. Therefore, the point

D (Figure 3) represents the minimum heat flux, and the vapor layer becomes stabilized. A thorough vapor layer is formed below the liquid layer at the vicinity of the surface. The point D is called the Leidenfrost point, known as incipient of the film boiling. The further increment of the wall superheat from D to E in the above diagram, in Region IV, relates to the film boiling. Due to the high degree of wall superheat, the radiation mechanism plays important role in transferring the heat, increasing consequently the wall heat flux.

The aforementioned boiling curve was obtained for the case of when the liquid pool is contained in a vessel and is heated through the gas burner. In the event of the surface quenching the Nukiyama curve can be reproduced from E-D-C-B-A. However, due to complex flow characteristic, the boiling curve is not same as in the case of surface quenching through the liquid jet impingement [Gradeck et al., (2009)] as shown in Figure 4.

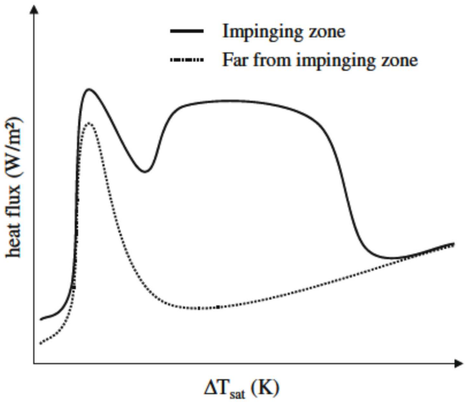

Figure 4 – Boiling curve for jet impingement [Gradeck et al., (2009)]

In the case of liquid jet impingement onto a heated surface, a moment of inertia of the liquid apart from energy equation is inevitable to compute the heat flux extracted from the surface. Whereas, in the case of pool boiling, a moment of inertia of liquid is not a crucial factor. Quenching through liquid jet, in comparison with the liquid pool, is capable of extraction of high heat-flux, as confirmed experimentally, [Miyasaka et al., (1980), Mozumder et al., (2006), Mitsutake and Monde (2003), Robidou et al., (2002)].

To understand the boiling of liquid during the quenching of the surface, one should be aware of the several flow regimes taking place at the surface. As the liquid jet impinges onto the horizontal surface, the flow regions are featured by stagnation, acceleration and wall-jet region (Figure 5). The area just underneath of liquid jet, where the flow velocity is close to that of a nearly stagnant flow, is called the stagnation region, spanning around 1.25 times of nozzle diameter [Watson (1964)] in the case of a laminar flow. While in the case of a turbulent flow, the jet stagnation region varies in size [Fuchang et al., (2006)].

As the flow passes through the stagnation region, the jet accelerates due to the static pressure difference between stagnation and an outer region, and the velocity of the flow can be higher than the velocity at the nozzle exit; this flow zone is termed as the acceleration region.

As the fluid progresses through acceleration region parallel to the surface, the flow velocity decreases gradually due to the viscosity effects and loss of momentum. The wall jet region is characterized by a lower velocity compared to the velocity related to the acceleration region. In the wall-jet region, due to the enhanced friction on the surface and consequent loss of momentum, the flow retards. Subsequently, the liquid layer becomes gradually thicker, because of mass conservation. This characteristic thickening of the liquid layer is termed as the hydraulic jump (Figure 5) [Watson (1964) and Stevens and Webb (1993)].

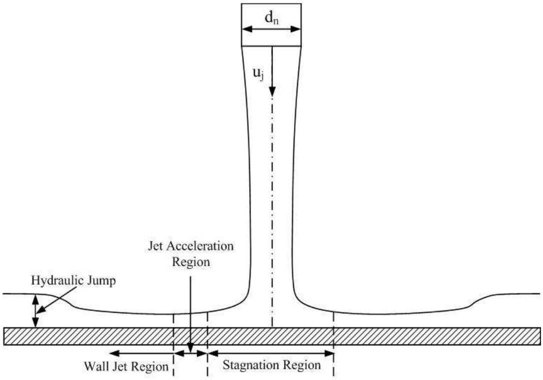

Figure 5 – Jet impact on the horizontal surface

On the other hand, the hydrodynamics of the multiple jets is quite complicated. Let us assume that the two jets interact with each other as shown in Figure 6; the jet up-wash exhibits as a common phenomenon. The jet up wash enhances the turbulent kinetic energy and hence, is responsible for the high rate of extraction of the heat flux from the surface. Due to the up wash of the jet, the water-pool height exhibits the wavy nature causing the difference in the relative hydraulic pressure at the jet stagnation region and the up-wash region.

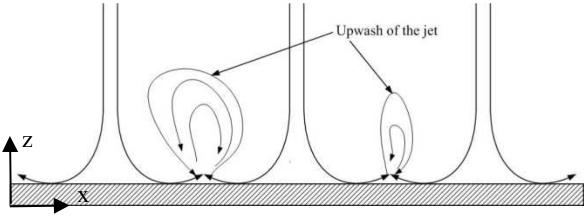

Figure 6 – Up-wash of the multiple jets

In the in-line arrangement of the liquid jets they interact intensively with each other as shown in Figure 6, illustrating the arrangement in the x-y plane, with the z-direction being normal to the x-y plane. The jets can be arranged in a staggered way forming a hexagonal pattern, Figure 7. Hexagonal distribution of jet facilitates extraction of heat flux homogeneously from the heated surface [Pan and Webb (1995)].

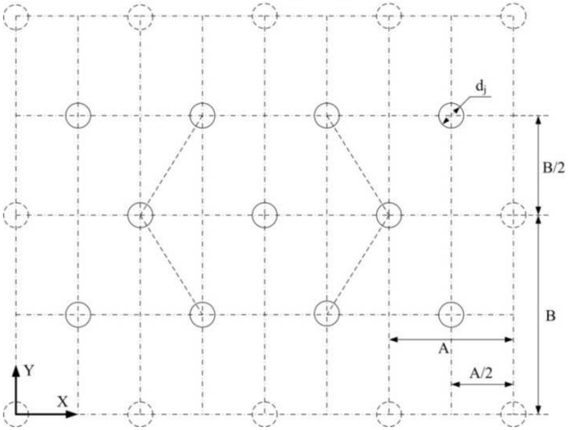

Figure 7 – Nozzle arrangement in the hexagonal pattern

In the case of quenching through multiple jets, the heat transfer mechanism becomes quite complicated, due to the several modes of boiling commencing simultaneously. Most of the published research delineates different form of correlations developed for the industrial applications, see e.g. Zürcher, et al. (2000), Wolf, et al. (1990), Omar, et al. (2009), Mitsutake and Monde (2003), Wang and Monde (2000), Monde (1985), Wang and Monde (1997) and Liu et al., (2004).

Some of the authors have focused their analysis only at the stagnation region investigating the maximum heat flux removal capacity, see e.g. Zumbrunnen, (1991), Liu et al., (2004), Liu (2003) and Qui and Liu (2005).

Furthermore, the film boiling has drawn much attention because of its application in the various processes in the industry. The governing physics is documented in due details by Nagendra (1971), Wang and Monde (1997), Liu et al., (2004). Nagendra [Nagendra (1971)] developed a model for saturated flow film boiling at NASA (National Aeronautics and Space Administration). Whereas, sub-cooled pool film boiling was modeled by Hamill and Baumeister, (1967) at Lewis Research Centre, NASA. They [Nagendra (1971), Hamill and Baumeister, (1967)] applied the entropy principle for determination of the shape of the interface between vapor and liquid rather than using the Taylor instability principle. Both models [Nagendra, (1971), Hamill and Baumeister, (1967)] were developed assuming two-dimensional steady state.

1.1. The objectives of the research

Surface quenching through liquid jets represents a very complex process because several heat-transfer mechanisms are implicitly coupled through material properties and fluid properties. The present research develops the understanding of the surface quenching phenomena through a single jet accounting for the liquid inertia that influences the characteristics of the quenching employing the computational models. Another aspect is to characterize the performance of the presently adopted 4-equation k-ε-ζ-f model of turbulence for this case.

The next objective is to envisage the phenomenon of a hydraulic jump in the case of moving surface and, furthermore, to investigate the capability of quenching model and to accordingly reveal another potential of the modeling aspect.

Envisaging the hydrodynamics of the multiple jet impingement process through computation modeling represents the next important task as well as the analysis of different aspects of the development of the water pool over the surface, interactions of the multiple jets and the intensity of the upwash. In addition, the validation of the theoretical model for the water pool height and average velocity of the water pool is considered. Finally, the work on development of the film boiling model including the effect of turbulence at the jet stagnation region is conducted.

1.2. Outline of the Thesis

The thesis consisted of seven chapters. The first chapter, which is the introductory chapter, delineates the motivation for the present work as well as the objectives of the research.

The second chapter discusses the state of the art in the flow boiling phenomena. The first section of this study is about hydrodynamics and convective heat transfer. Accordingly, the physics of boundary layer, thermal boundary layer at the stagnation region and wall jet region are studied. In addition, the effect of motion of the surface on the heat transfer from the literature is discussed. The second section deals with the deliberate quenching through the liquid jet. It describes the mechanism of the quenching while the surface is initially at approximately 600 °C. The third section describes the bubble dynamics in the process of nucleate boiling, since it influences the maximum heat flux as well as the mechanism of the film collapse at minimum heat flux. Hence, the fourth and fifth sections discuss these phenomena. The sixth section delineates the film boiling in the case of liquid jet impingement. The seventh section discusses the influence of turbulence in the jet impingement flow boiling. The eighth section describes various aspects of the growth, collapse and explosion of the bubble. The ninth section describes hydrodynamics and heat transfer aspects of the multiple jet impingement.

The third chapter describes the mathematical model applied in this research. The first section illustrates the Eulerian averaging technique. In the second section, the computational model describes the flow with phase change, where mass conservation is derived using the Eulerian averaging method. After that, the quenching model is discussed. The momentum and energy equations for the fluid are derived. Afterward, energy equation for the solid block is given. The third section describes the computational model for multi-fluid flow without phase change. Afterward, the volume of fluid interfacial momentum exchange model is described. The fourth section describes the four equation (k-ε-ζ-f) turbulence model along with the relevant wall treatment. The fifth section delineates the numerical solution methodology. Integral forms of equations are discretized using higher order differencing schemes. SIMPLE (Semi-Implicit Method for Pressure-Linked Equation) is discussed in short. Then the next sections describe the segregated approach (AMG method) to solve the resultant algebraic equations. Further sections describe the implementations of the boundary conditions. At last, the concepts of conjugate heat transfer implemented in the problem, as well as the parallel processing of the problem, are discussed.

The beginning of the fourth chapter describes hydrodynamics of the single jet impingement. Then, an experimental study is described aiming at providing relevant database for computational validation in order to make decision about the turbulence model. From the heat-transfer point of view, another experimental case is adopted; in order to analyse the predictability of the four-equation ($\mathrm{k}-\varepsilon-\zeta-\mathrm{f}$) turbulence model. The fourth, fifth and sixth sections describe the computational details of surface quenching through the single liquid jet. The last section of the fourth chapter discusses the important results obtained from the computational study.

The fifth chapter describes an analytical expression for the determination of the pool height and average velocity of water pool for the given mass flow rate and its computational validation. The third section outlines the computational domain of the multiple jets. The fourth section discusses the important results obtained. The effects of the mass-flow rate, surface width and the turbulence produced due to the impingement, as well as of the hydraulic jump on the jet interaction are studied. At the end of this chapter, the semi-empirical model developed by considering the data from the literature for the quenching of the multiple jets system is illustrated.

The chapter sixth is devoted to the analytical model development for the film boiling at the Liedenfrost temperature including the effect of instability. Here, a model for both planar and circular jets including the effects of turbulence is formulated. Finally, the seventh chapter delineates the conclusions and recommendations for the future work.

2. State of the Art

2.1. Hydrodynamics and convection heat transfer

The understanding of the flow behavior is a prerequisite to investigating transport phenomena for the heated surface. Therefore, discussing a review on the state of the art of the liquid jet hydrodynamics is of importance. Stevens and Webb (1993) had performed the study of the liquid jet impinging onto the horizontal surface. They had verified the analytical model developed by Watson (1964) using the laser-Doppler velocimetry (LDV) for the measurement of the velocity and turbulence across the boundary layer. They found that maximum velocity and highest turbulence level at the radial locations less than 2.5 times nozzle diameter; which contradicts the assumption made by Watson (1964).

Fujimoto et al., (1999) had studied the convective heat transfer between a circular jet and a solid surface numerically and considered several hydrothermal properties of the liquid such as viscosity, surface tension, and Nusselt number. They solved steady state condition of the laminar flow and energy equations along with the constant heat flux boundary condition at the surface. The literature mentioned above [Fujimoto et al., (1999)] is necessary to understand the physics of both momentum and thermal boundary layers at stagnation and wall jet regions.

Zumbrunnen et al. (1992) studied heat transfer for the case of the laminar jet impinging onto the moving surface. They solved an integral form of boundary layer equation for stagnation region and free surface jet region. In general, the surface velocity intensifies the turbulent kinetic energy (TKE) and heat transfer rate at the free surface jet region. This study reveals the facts that in the jet impingement case the two regions, namely the stagnation region and free surface jet region (i.e., wall-jet region), exhibit different mechanism concerning the heat flux. The reason is to be looked for in the differences in the velocity field at stagnation and free surface jet regions. The Zumbrunnen's theoretical model requires the validation against experimental results for the given range of parameters.

2.2. Quenching through jets

It is important to envisage physics of the quenching while the liquid jet impinges onto the surface at very high temperatures (surface temperature > 900 °C). Most of the literature describes the quenching process at low surface temperatures (less than 900 °C) [Gradeck et al., (2009), Omar et al., (2009), Xu and Gadala, (2006), Islam et al., (2008), Seiler-Marie et al., (2004)].

At the surface temperature lower than 900 °C, an experimental investigation [Islam et al., (2008)] shows that the liquid comes into contact with the heated surface and starts the heterogeneous/homogeneous nucleation. The tiny bubble formation starts just after the impingement. Islam et al., (2008) conducted such experiments considering water jet diameter of 2 mm, the sub-cooling range of water between 5-80 K and nozzle velocity 3-15 m/s; surface was made up of steel/brass, which was heated up to 500-600 °C. For the steel block at an initial temperature of 500 °C, 5 m/s of jet velocity and 80 °C of water temperature, the high-speed video imaging show circular shiny liquid sheet at the center of the steel block encompassing the time interval between 3 and 30 milliseconds. The quiet and calm flow and no boiling sound were evidence of no contact of liquid to the surface. At the start of impingement, there may be the liquid-solid contact for short period in which the bubbles form, coalesce and generate a tiny liquid sheet onto which the jet slides. Slightly later, around 200 milliseconds, there is the contact of the jet with the surface, influencing the onset of homogeneous/heterogeneous nucleation, and subsequently of the boiling sound. Hence, the tiny liquid sheet began to disappear. Some of the bubbles splashed at a certain angle from the surface. After 500 milliseconds, more contact with the surface was occurred and rigorous generation, coalesce, and splashing of the bubble took place.

While for a brass surface, just after the impingement, flow exhibits the explosive pattern, the mechanisms mentioned are not pertinent to the case of surface temperature equal to or higher than 900 °C for the steel. In the case of steel surface equal to or more than 900 °C, quenching through water jet leads to different boiling phenomena. The heat transfer process governed by several boiling mechanisms depends upon wall-superheat ($\Delta T_{surface}$ - ΔT_{sat}). These heat transfer mechanisms are convection, nucleate, transition, and film boiling. In the convection, heat transfer takes place through the motion of the fluid. The convection heat transfer is easy to calculate, described in Leinhard IV and Leinhard V (2011) through the equation as given below.

$$h = \frac{q}{(T_w - T_\infty)} = -\frac{k}{(T_w - T_\infty)} \frac{\partial T}{\partial y}\bigg|_{y=0} \tag{2.1}$$

Nevertheless, other boiling heat transfer mechanism such as nucleate, transition and film boiling are very complex in nature and already discussed in the first chapter, Figures 3 and 4. However, the prediction of heat-flux was facilitated through numerous correlations and theoretical models proposed by different authors [Omar et al., (2009), Xu and Gadala (2006), Islam et al., (2008), Andreani and Yadigaroglu (1992), Mitsutake and Monde (2003), Timm et al., (2003), Rivallin and Viannay (2001), Robidou et al., (2002)]. The wall-superheat and associated heat-flux determine the different heat transfer mechanism depending upon the flow condition. One of the models developed by the Zürcher et al., (2000) to differentiate between nucleate boiling and convective evaporation inside a horizontal tube to predict the heat flux at the onset of nucleate boiling is given as:

$$\dot{q}_{ONB,\ x} = \frac{2\sigma T_{sat}\, h_{cb,crit}}{r_{crit}\, \rho\, \mathrm{V}\, \Delta h_{evap}} \tag{2.2}$$

The heat transfer coefficient $h_{cb,\ crit}$ defined as:

$$\mathrm{h_{cb,crit}} = \mathrm{C}\ \mathrm{Re}_{\delta}^{\mathrm{m}} \mathrm{Pr}_{\mathrm{L}}^{0.4} \frac{\lambda_{\mathrm{L}}}{\delta_{\mathrm{crit}}} \tag{2.3}$$

Where, the values of the two constants, $\mathrm{C} = 0.01361$ and $\mathrm{m} = 0.6965$, are based on experimental results of pure convective heat transfer in annular flow for ammonia refrigerant (R-717).

Robidou et al. (2002) performed an experiment under steady state condition for controlled cooling of the heated surface through a water jet. They studied the influence of the jet velocity, sub-cooling of water and the surface temperature. For a jet velocity of 0.8 m/s, the surface temperature of about 450 °C, and sub-cooling of 16 K the film boiling takes place at stagnation region. The reason may lie on the mechanism that, because of the low jet velocity and a high temperature, the water is not capable of penetrating the vapor formed near the surface.

Gradeck et al., (2009) described the boiling curve for several locations at the curved surface through jet impingement. They explored the mechanism of the quenching through planar water jet of the heated rolling cylinder experimentally. The initial temperature of the cylinder was 500-600 °C, the sub-cooling range of water was 10-83 K, the jet velocity range was 0.8-1.2 m/s and the jet velocity to surface velocity ratio (u_s/u_j) was in range between 0.5 and 1.25. They found aberration from the standard boiling curve (Nukiyama Curve), i.e., the existence of the “shoulder of flux” in the stagnation region as shown in Figure 8. The width of the shoulder of heat-flux increased with the sub-cooling of liquid. At some other locations at the surface, e.g. as within the wall-jet region; the relevant boiling curve depicts approximately the standard one.

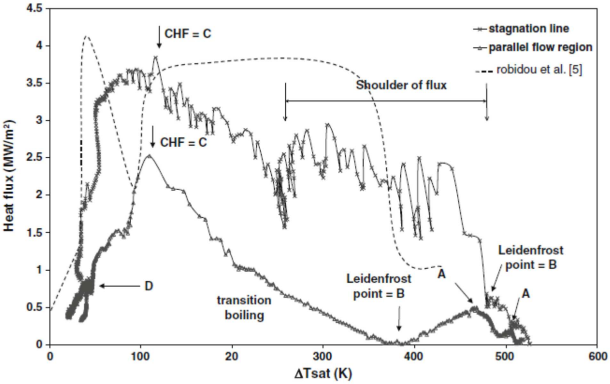

Figure 8 – Boiling curves ΔTsub = 15 K; u_j = 1.2 m/s; d = 50 mm [Gradeck, et al., (2009)]

As the liquid jet interacts uniformly with the heated plate at very high temperature, just after few milliseconds of the impact of the jet, the vapor generation rate is quite high due to the high wall superheat. Nevertheless, as the time elapses, the vapor generation rate decreases and, vapor film cannot sustain longer at the immediate vicinity of the surface. The collapse of the film is the consequence. Due to this mechanism, the film boiling shifts to nucleate boiling shown by curve B (Figure 9) at MHF (Minimum Heat Flux). In the case of heating, it passes from CHF (Critical Heat Flux) along the curve B to film boiling. However, depending on the thermal inertia of the heated surface the curve always moves along the lines according to A in Figure 9.

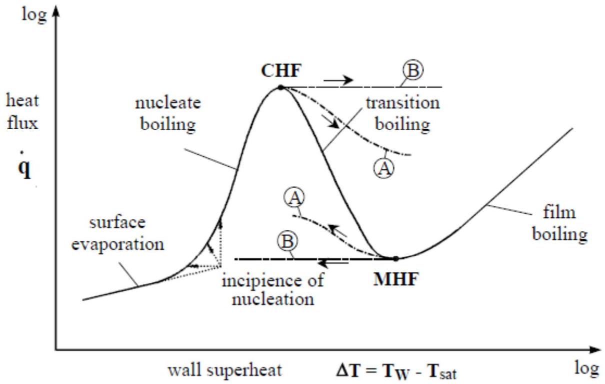

Figure 9 – Hysteresis along the Nukiyama curve [50]

The hysteresis behavior is found in the transition and steady state boiling by Witte and Lienhard, (1982). This hysteresis consists of a transitional nucleate boiling and a film boiling branch, both overlapping on the heat-flux. However, implying precise temperature control system [Auracher and Marquardt, (2004)] and with a clean heating surface, boiling curves, even for liquids with large contact angles (water), show no hysteresis regardless in which direction they were measured: stepwise from film to nucleate boiling or vice versa. Moreover, due to the surface contamination, boiling curves are not reproducible. Each test run, even under carefully established steady state conditions, results in a shift of the curve already at a minimal change of the deposit [Auracher and Marquardt, (2004), Ungar and Eichhorn, (1966)].

2.3. Bubble dynamics in nucleate boiling

Omar et al., (2009) developed the analytical/empirical model to predict the heat transfer rate for nucleate boiling in the stagnation region of a planar jet impinging onto a horizontal flat surface. The model assumes that bubble induced mixing would result in enhanced momentum and thermal diffusivity. Hence, flow and energy equations considered the additional diffusivity. The bubble dynamics, such as frequency of bubble generation and average bubble diameter were characterized using high-speed imaging and an intrusive optical probe.

A correlation for the effective diffusivity was developed using the flow parameter, thermophysical properties of liquid and surface thermal properties as given in the equation (2.3).

$$\varepsilon^{+} = \frac{\mathrm{Re}_{\mathrm{b}}^{x_1}\mathrm{Ja}_{\mathrm{sup}}^{x_4}\mathrm{Ja}_{\mathrm{sub}}^{x_5}}{\left(\mathrm{We}_{\mathrm{b}}^{x_2} + x_3\right)}$$

(2.3)

where, $x_1 = -0.7736$, $x_2 = 4.283$, $x_3 = 5.634$, $x_4 = 4.167$, $x_5 = -1.586$

The developed model is valid under the range of mass flux 388–1649 kg/m^2. s, degree of sub-cooling 10-28°C, surface temperature 75-120°C with accuracy of heat flux around +30% to -15%.

Due to the technological limitation, the experimental investigation of the bubbles growth mechanism for the jet impingement system is very complex. As bubble contains the 30% of the total heat flux [Stephan and Hammer, (1994)] in the case of the nucleate boiling. Therefore, one needs to study the bubble dynamics to develop the model. While, bubble residence time is in the order of microseconds [Avdeev and Zudin, (2005)]. Until now, there are no published literature on the experimental study of bubble dynamics for such a high-temperature jet impingement boiling/quenching system. However, Mukherjee and Kandlikar, (2005) studied the bubble growth numerically in the square microchannel of size 200 µm. Bubble resides at the center, and the superheated liquid fills the entire channel. They found that the bubble growth rate increases with the incoming superheated liquid while, it decreases with Reynolds number. They noticed the forward and backward movement of the bubble, and there was little effect of the gravity on the bubble growth. The other study on the bubble dynamics are by Mann et al., (2000) and Fuchs et al., (2006) and are important in mentioning a detailed study by the interested researchers.

Very few works based on numerical simulation, exist for the nucleate boiling considering the jet impingement flow boiling. Nucleate boiling contains mainly four processes such as the formation of nucleation site, bubble formation, merger, and explosion. Son et al., (2002), investigated the bubble merger process numerically. They found that the thin liquid film forms underneath a growing bubble attached to the wall and this part contribute 30% of the total heat flux carried by the bubble. Therefore, it is important to include for the numerical study.

The bubble growth behavior differs at different atmospheric pressure. The precise experiment on nucleate pool boiling by Kim et al., (2007) is evident. The bubble growth rate at sub-atmospheric pressure is larger than at atmospheric pressure irrespective of the fluid properties. Also, because of the relatively higher pressure, momentum is strong, based on the Rayleigh-Plesset equation owing to the high specific volume.

Avdeev and Zudin (2005) developed the inertial thermal model, which grows in the superheated liquid. They suggested the general inertial thermal model for the vapor bubble growth inside the superheated pool of liquid.

However, a simple way of determining the bubble growth rate is given by molecular-kinetic laws of evaporation of liquid from the superheated interface as given in equation (2.4):

$$\dot{R}(t) = \frac{0.4\beta}{1-0.4\beta}\frac{L(T_\infty - T_o)}{\left(R_g T_0^3\right)^{0.5}}$$

(2.4)

Another way of determining the bubble growth rate is from dynamic viscous mechanism as given in equation (2.5)

$$\dot{R}(t) = \frac{p_o - p_\infty}{4\mu}R(t)$$

(2.5)

The dynamical inertial mechanism determines the radius of the bubble, which is a function of time, by Rayleigh (1917) formula in equation (2.6).

$$R(t) = \left(\frac{2}{3}\frac{p_0 - p_\infty}{\rho_L}\right) t$$
(2.6)

Therefore, it is clear that the nucleate boiling is very much sensitive to the generation, growth, and merger process of the bubbles. Thus, for investigation of the nucleate boiling, one must have an emphasis on the dynamics of the bubble. Nevertheless, for the engineering application, one can take into account the cumulative effect of the bubble dynamics to calculate the overall heat flux.

2.4. Maximum heat flux

The surface quenching can be controlled by several parameters such as the jet velocity, system pressure, sub-cooling, etc. One of the significant work by Mitsutake and Monde (2003) obtained the ultra-high-critical heat flux through experiment. They [Mitsutake and Monde (2003)] used the highly sub-cooled liquid jet impinging onto the rectangular surface. The other parameter such as jet velocity was 5-60 m/s, the temperature of the liquid jet was 20°C, system pressure was 0.1-1.3 MPa, and sub-cooling was 80-170 K with increasing system pressure. They measured 211.9 MW/m^2 of maximum heat flux for 35 m/s jet velocity, liquid sub-cooling of 151 K and system pressure 0.7 MPa. Gambill and Lienhard (1989) proposed an analytical model of maximum heat flux predict 48% of the experimental value by Mitsutake and Monde (2003). The reason for under prediction by the analytical model is due to assumptions taken. Which are as follows: (i) steady state flow, (ii) the laminar flow.

Moreover, the maximum heat flux is at a stagnation point in the experiment of Mitsutake and Monde (2003). However, the location of maximum heat flux is not certain as the liquid is impinging onto the heated surface. Hence, Mozumder et al., (2007) studied the maximum heat flux propagation in the case of sub-cooled water jet impinges on the heated cylindrical block with initial temperature range 250-600 °C.

Mozumder [Mozumder et al., (2007)] found that when the wetting front starts moving towards the circumferential region, the maximum heat flux reaches visible leading edge of the wetting front. They found that the velocity of the wetting front propagation increases with the rise of jet velocity and the sub-cooling of the liquid decreases with the increment of the initial block temperature.

Another work of Mozumder (2006) prescribed the correlation of the maximum heat flux value be valid to the block temperature 250-400 °C, sub-cooling 5-80 K and jet velocity 3-15 m/s.

As the initial temperature of the block is low as compared to the case of steel-block, quenching in the hot rolling process cannot be applied for the prediction of maximum heat flux for such application. In most of the industrial application, the surface temperature is around 800-1100°C. When the initial temperature of the block is higher, the quenching process is transient in nature.

The correlation developed by them predicts ± 30% of the maximum heat flux for the brass and copper material, but for steel material, the error lies in the much larger region. The reason for such aberration may lie on different thermal material properties of the brass and copper as compared to steel.

Qui and Liu (2005) developed a correlation of critical heat- flux (CHF) for the jet velocity range 0.5-10 m/s, at the jet stagnation region employing a saturated liquid jet of water, ethanol, R-113, R-11. They took the same heater diameter as of the jet diameter. However, as discussed before the stagnation region is greater than the jet diameter. They proposed correlation in the following form (Equation 2.7).

$$\frac{q_{c,o}}{\rho_l u_j h_{fg}} = 0.130 \left(1 + \frac{\rho_v}{\rho_l}\right)^{1/3} \left(\frac{\sigma}{\rho_l u_j^2 d}\right)^{1/3} \left(\frac{\rho_v}{\rho_l}\right)^{1.4/3} \tag{2.7}$$

This correlation shows that there is no effect of thermal properties of the substrate material. The correlation factor found by the wide range of jet velocities from the experiment.

Liu and Qui (2008) developed the correlation of Critical-Heat-Flux (CHF) for the jet stagnation region for the super hydrophilic surface. They formed the super hydrophilic surface by coating the copper cleaned and mirrored surface with titanium oxide. When the surface irradiated with the UV-light, the water contact angle becomes zero after some time. The effect of the super hydrophilic surface seen as 30% enhanced heat transfer from the surface. Considering the substrate diameter is greater than the jet diameter and proposed the correlation in the following form (Equation 2.8).

$$\frac{q_{c,o}}{\rho_l u_j h_{fg}} = 0.0985 \left(\frac{\rho_v}{\rho_l}\right)^{0.275} \left(\frac{\sigma}{\rho_l u_j^2 d}\right)^{1/3} \left(\frac{1}{1+0.00113\,(D_s/d_j)^2}\right) \tag{2.8}$$

Transition boiling exhibits distinct characteristics as evidence from the experiment of the Seiler-Marie et al. (2004). When the maximum heat flux is achieved at certain wall-superheat, then a further increment of the wall-superheat the first minimum heat-flux comes, and further increment of wall-superheat resulted in an increment of the heat-flux for a broad range of the wall-superheat. Which is termed as the shoulder of heat-flux as shown in Figure 10. The beginning of the shoulder of heat flux comes at a first minimum and ends with minimum film boiling point. They developed the model for the shoulder of heat flux, first minimum boiling point, i.e., start of the shoulder of heat flux and second minimum boiling point (which is incipient of the film boiling). Their model assumes that existence of periodic bubble oscillation at the wall caused by the jet hydrodynamics.

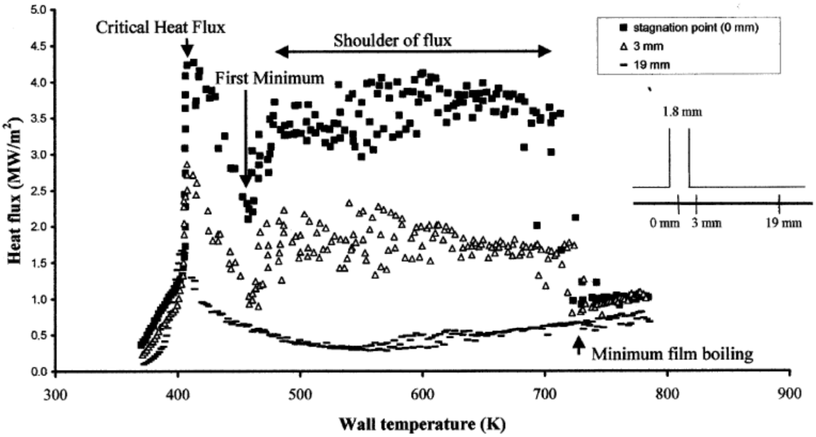

Figure 10 – Wall heat flux at different locations from the stagnation point of a planar water jet [Seiler-Marie et al. (2004) jet velocity 0.8 m/s and water sub-cooling 16 K]

2.5. Film collapse at minimum heat-flux

It is important to study the critical temperature of the wall at which the film collapses. Until now, no experiment has been done to investigate the vapor film collapse for the jet impingement cooling process. However, Meduri [Meduri et al. (2009)] investigated the film collapse temperature for the sub-cooled flow film boiling on a vertical flat plate. The part of the wall heat flux is responsible for the increment of the temperature of the liquid and some for the vapor generation (latent heat for phase change). When the liquid sub-cooling increases, the net vapor generation decreases and at fixed critical sub-cooling of the liquid the production of the vapor too small to consider. This means total wall heat flux goes into the liquid. A correlation for the film collapse temperature proposed for the wall temperature and liquid temperature.

$$(\Delta T_w)_{fc} = \frac{h_{fg}}{Cp_v}\left(0.006\left(\frac{\rho_l}{\rho_v}\right)^{0.83} Pr_l^{0.33}\,\frac{Ja_{sub}^{0.33}\left(1+0.0005\,Re_l^{0.75}\right)^{1.67}}{\left(1+7.7\exp(-512\,Ja_{sub})^{1.67}\right)}\right)^{1.67} \quad (2.9)$$

Freon-13 liquid and copper test specimen selected for the proposed correlation. Therefore, investigation of minimum film collapse temperature needed for a large range of different fluid properties and thermal properties of the surface.

Ohtake and Koizumi (2004) investigated the mechanism of the vapor-film collapse through the propagation of the film. They found that when the local cold spot temperature decreased, and propagation velocity of vapor-film collapse would decrease. As a result, Minimum Heat Flux (MHF) temperature would increase. The significant increments registered in MHF temperature for the case of local cold spot temperature lower than the thermodynamic limit of liquid superheat, T_{tls}.

2.6. Jet impingement film boiling

In the case of film-boiling and nucleate boiling, as the wall superheat increases, the wall heat flux also increases. However, in the event of transition boiling as the wall superheat increases the heat flux decreases. The reason for the decrement of the heat flux with increasing the wall superheat is as the wall superheat increases beyond the maximum heat flux (the corresponding wall superheat) the bubbles formation rate increase and bubble dynamics such as growth, merger, and explosion, can trigger intermittent contact of the liquid jet to the heated surface. In other words, because of the high rate of formation of vapor, the residence time of the contact of the liquid jet to the heated surface decreases.

Furthermore, the increment of the wall superheat, the bubbles merge together and forms the vapor layer on the heated surface. Once, this vapor layer is stable the heat transfer rate becomes minimum, because of the very low conductivity of the vapor. This minimum heat flux is called as Leidenfrost heat- flux and the corresponding wall superheat as Leidenfrost temperature.

The existence of the turbulent film boiling for the liquid jet impingement cooling is evident from the fact that high oscillation of the vapor-liquid interface. As the flow over heated surface exhibits the turbulent nature results in an increment of thermal diffusivity of the vapor and consequently, increases the wall heat flux. Sarma et al., (2001) performed the analysis of the turbulent film boiling over the cylinder. Due to the steep temperature gradient in the vapor layer, the thermo-physical properties of the vapor varied and taken into account. They included the effect of the radiation and found satisfactory agreement with the experiment.

Liu and Wang (2001) have done a theoretical and experimental study of the film boiling at jet stagnation region for high sub-cooling of the water. They proposed the semi-empirical correlations for the wall-heat-flux as follows.

$$q_w = \left[1.414\, Re_l^{1/2} Pr_l^{1/6} (\lambda_l \lambda_v \Delta\theta_{sub} \Delta\theta_{sat})^{1/2}\right] / d_j$$

(2.10)

The correlation has -5% to +25% variations from the experimental results. For higher jet velocity and the high sub-cooling correlation exhibits larger (more than 40%) deviations from the experimental wall heat flux. The reason may lie in the fact that the high jet velocity enhances the turbulent intensity near the surface and its effect on heat-flux is not accounted.

Liu et al., (2002) performed the experiment on the quenching of heated surface through the nozzle. In this case, the initial temperature of the plate was 700-900 °C and the water temperature was 13 °C and 30 °C. They plotted the boiling curve have not shown the film boiling phenomena for such a high sub-cooling of the liquid. Although, they agree upon the fact, that just after the impact of the jet, the liquid cannot contact the surface as the film formed underneath the jet. Another reason is the surface temperature for a very short interval of the time, just after the impact is hard to measure, due to the experimental limitations.

The Leidenfrost temperature depends on several parameters, like jet impingement velocity, wall-superheat, sub-cooling of liquid, the conductivity of the material, the thermal heat capacity of the material and some other material aspects (such as surface roughness, granular structure of the surface). How these parameters affect to the type of quenching of the surface are not well understood. To understand the complexity of the problem, mathematically, the Leidenfrost temperature is a function of thermal and material properties of the plate. It is possible to model, only when, one could do the characterization of the material properties by the Leidenfrost point considering the thermal and flow parameters as mentioned above. This would require an enormous amount of database only for film boiling at Leidenfrost temperature. Consequently, Direct-Numerical-Simulation for this problem would require plenty of computer hardware space and RAM to execute and store the calculation and output results. Therefore, the computational cost will be too much. Therefore, it is complex phenomena to model from the first principle. Here, the first principle implies that the Direct Numerical Simulation.

The current status of the research on the boiling at Leidenfrost temperature is only experimental works exist till date [Ishigai et al., (1978), Robidou et al., (2002), Bogdanic et al., (2009), Seiler-Marie et al., (2004), Liu (2003) and Woodfield et al., (2005)].

Ishigai et al., (1978) performed the experiment for the film boiling at stagnation region for the planar jet and then analytical study with two-phase boundary layer theory. Their result shows qualitatively good agreement, but 1.6-1.7 times higher heat flux than analytical results.

Bogdanic et al., (2009) analyzed the vapor–liquid structures at stagnation region by using the miniaturized optical probe for sub-cooled (20 K) planar (1 mm-9 mm) water jet with a velocity of 0.4 m/s. They measured the liquid surface contact frequency at the incipience of nucleate boiling is about 40 Hz and at the end of the transition boiling nearly 20,000 Hz. Therefore, it infers that for film boiling the frequency of the liquid-vapor interface is higher than 20,000 Hz.

Meduri et al., (2009) conducted an experiment on the sub-cooled flow film boiling on a vertical flat surface. The correlation calculated the heat flux around ± 20% for the given wall-superheat 200-400°C.

Some of the experimental studies [Meduri et al., (2009), Hsu and Westwater (1960), Coury and Duckler (1970), Suryanarayana and Merte (1972)] on film boiling over the vertical plate advocate that the vapor film is turbulent in nature. The reason may lie in this fact that oscillation frequency (> 20,000) [Bogdanic et al. (2009)] of vapor film interface due to gravitational force and inertia force of liquid jet on the vapor film. Note that, oscillation frequency may increase or decrease, depending upon nature of the application of inertia force on the vapor film. Sarma et al. (2001) investigated the turbulent film boiling on the cylinder. While the effect of inertia force on the vapor film is very less. On the contrary, both inertia and gravity forces of liquid jet acted on the vapor film, which causes the higher oscillation frequency. Chou and Witte (1995) developed the analytical model for the stable sub-cooled flow film boiling on the cylinder surface. They [Chou and Witte (1995)] developed the model of film boiling for the wake region of the flow. However, the model did not consider the turbulent flow. Therefore, this model is not suitable for the inertia dominated turbulent flow film boiling.

Almost explosive flow pattern visualized at the wall superheat greater than 300 K. Quite chaotic and turbulence flow observed by Woodfield at al. (2005) during the quenching of the heated surface. The Woodfield's [Woodfield at al. (2005)] observation supports the consideration of the turbulence in the jet impingement quenching process. Because, inertia, thermal buoyancy, and gravity forces play a vital role in the flow being turbulent. Before, going into the details of the modeling process, the discussion of the physics of the liquid jet impingement onto the high wall superheated plate at stagnation region at the Leidenfrost point is necessary. Due to the high wall-superheat, vapor generates at a high rate, which cannot escape in the normal direction to the plate due to the liquid jet, it has the only way to escape through parallel to the wall. In this way, vapor layer forms at the vicinity of the wall and liquid layer exist over vapor layer. Consequently, the film boiling establishes. Due to the formation of the vapor near the wall, the inertia force of the fluid increases and the gravity force also come into play. Consequently, Rayleigh-Taylor instability [Rayleigh (1917)] establishes despite the low jet velocity called the thermal buoyancy effect on the film. Due to the high frequency of oscillation of liquid-vapor interface exhibits dynamic behavior, which contributes to enhancing the momentum and thermal diffusivity. The instantaneous flow can be divided into two parts, which are mean (Reynolds average), and the fluctuating part. The fluctuating part can be modeled as turbulent diffusivity.

Previously, the assumption was that due to the low velocity at the stagnation region the flow is laminar. However, in the case of multiphase flow phenomena at the stagnation region there exists the vortex-flow phenomenon studied by Sakakibara et al., (1997). Therefore, to calculate the heat flux and the temperature at the Leidenfrost point, the introduction of the turbulent thermal diffusivity is necessary. Karwa et al., (2011) proposed the model without considering the turbulence near Leidenfrost temperature. They reported 46% less wall heat flux and 70% less wall-superheat**.** Therefore, there was the necessity to develop the model considering the effect of turbulence especially, for turbulent jet and a higher degree of sub-cooling (< 45 K).

2.7. Turbulence in jet impingement flow boiling

Shigechi et al., (1989) studied analytically the two-dimensional, steady state and laminar film boiling with a downward facing at the jet stagnation region considering the saturated liquid with radiation heat transfer and compared the heat flux and wall superheat with experiment. Although the qualitative results were good, the quantitative was two times less.

Fillipovic et al., (1993) studied the laminar film boiling over the moving isothermal plate. They obtained the similarity solution for the boundary layer on the surface. Because of the vapor layer at the surface, the viscous force and heat transfer rate reduced in comparison with the complete liquid layer (in the case of convection) and vapor-droplet mixture (in the event of nucleate and transition boiling) at the surface.

Furthermore, Filipovic et al., (1994) dedicated to studies of the effects of turbulent film boiling phenomena for the isothermal moving plate using the modified Cebeci-Smith (1967) eddy-viscosity model with the Cebeci-Bradshaw (1984) algorithm. A correlation proposed for the surface heat flux resulted in the maximum error of -30% for liquid subcooling (ΔT_{sub} = 70K), free stream velocity 5.3 m/s and plate temperature 873.15 K along with the ratio of the plate velocity-to-free-stream velocity. Therefore, there is room to increase the range of the parameters, accomplishes in chapter five, developed the film boiling model including the effect of the interface oscillation.

Wolf et al., (1990) showed the importance of the turbulence to enhance the heat flux removal rate from the surface. The range of the jet Reynolds number was from 15000-54000. Increasing the jet Reynolds number enhancements of the heat-flux attributed due to the enhanced turbulence at high jet velocity for the single-phase convection and nucleate boiling. The substantial work performed by the Castrogiovanni and Sfroza (1997) considered turbulence in their analysis by assuming the dynamics of bubble formation, merger, explosion, and implosion in the boiling phenomena, which in turn enhanced the momentum and thermal diffusivity. They used the genetic algorithm (GA) to quantify the bubble dynamics and applied it for the boiling inside a pipe flow.

Behnia et al., (1998) predicted the heat transfer in an axis-symmetric turbulent air jet impingement on a heated flat plate. Because of the anisotropic nature of the turbulence near the wall, normal velocity relaxation turbulence (v2f) model [Durbin (1995)] is applied. Whether, the standard and RNG (Re-Normalization Group) k-ε model [Launder and Spalding (1974), Yakhot et al., (1992)] with wall function over predicted the heat transfer coefficient, because of the over prediction of the turbulence kinetic energy at the jet stagnation region. Moreover, the k- ε model predicted the physically unrealistic behavior of the Nusselt number for large aspect ratio (H/D = Nozzle-to-plate-spacing/Nozzle-diameter).

Son and Dhir (2008) simulated numerically the film boiling on the horizontal cylinder. They used the level-set method for tracking the liquid-vapor interface. Finite difference method used to solve the mass, momentum and energy equation in vapor and liquid phases. Furthermore, investigations made for heat transfer in film boiling including the effect of the cylinder diameter and gravity on the interfacial motion.

Chou and Witte (1995) developed the analytical model for the film boiling on the horizontal cylinder covering the entire cylindrical region i.e., front and wake region and compared with experiment and other published results [Chou et al. (1995)].

Banerjee and Dhir (2001)[1] studied the sub-cooled film boiling on a horizontal disc. Linearized stability analysis was performed on the vapor layer underlying a pool of sub-cooled liquid. While the nonlinear evolution of the vapor interface was obtained through numerical study. The growth rate of the interface, the flow and temperature fields in the vapor and liquid phase, dissipation of heat flux from the wall into the sub-cooled liquid obtained from the analytical/numerical study. This study under predicted around 10-40 % as compared with the experiment [Banerjee and Dhir (2001)[2]]. For very low subcooling ($\Delta T_{sub} < 10K$) of liquid, the heat flux prediction is around -10 %.

Numerical simulation on the film boiling from the literature [Yuan et al., (2008), Son and Dhir (1998), Baumeister and Hamill (1967), Nagendra (1971), Esmaeeli and Tryggvason (2004), Malmazet and Berthoud (2009)] says that the vapor interface has been captured either by VOF (Volume of Fluid) or by Level-Set (LS) method depending upon the requirement of accuracy and focus of study areas.

The above-mentioned studies performed for the pool boiling, where the liquid inertia is absent. In the case of unsteady liquid jet impingement, one has to take into account the effect of inertia on different heat transfer mechanism, which is governed by the different boiling mechanism. For low subcooling of liquid ($\Delta T_{sub} < 10K$) and higher wall-superheat of the surface ($\Delta T_{sat} > 873.15K$), it can be assumed that just after the liquid jet impingement the film boiling mechanism plays the role for heat transfer. The above-mentioned range sub-cooling and wall-superheat can be varied ± 10% depending upon the liquid thermal and viscous properties, substrate thermal properties, and the flow properties. These should be determined experimentally for the different flow range for the different substrate material.

At a very high temperature of the surface (> 800°C), the inclusion of the radiation is necessary for the analysis of the film boiling. Hamill and Baumeister (1967) have included the effect of radiation for the case of sub-cooled pool film boiling. The analysis based on the concept of maximization of the entropy. In the case of the flow film boiling, inertia effect would be included in the concept of entropy maximization to determine the heat flux.

Through the above discussion, it has been felt that in the case of liquid jet impingement onto the heated surface the turbulence plays a vital role in the heat transfer mechanism.

It has been found that the accurate modeling and computation of production and dissipation rate of the turbulent kinetic energy at the vicinity of the surface is required which plays a significant effect on computation of heat-flux [Wolf et al. (1995)]. The turbulent dissipation is the rate at which turbulent kinetic energy converted into thermal internal energy, equal to the mean rate at which work done by the fluctuating part of the strain rate against the fluctuating viscous stresses.

2.8. Another quenching studies

Fuchang and Gadala (2006) used the iterative and sequential heat transfer analysis to determine the heat flux at the stagnation region of water jet impingement at the stationary heated surface. They noticed that heat transfer behavior is significantly affected by the water temperature rather than water flow-rate.

Hall et al., (2001) investigated a technique for controlling the boiling heat transfer by injecting the gas into the circular liquid jet. They did the experiment with the cylindrical copper specimen. The gas injected with void-fraction range 0-0.4 and the liquid velocity ranging from 2-4 m/s. They reported the enhanced convective heat transfer by a factor of 2.1 in the stagnation region as compared to single-phase convective heat transfer. Nevertheless, the maximum heat flux is unaffected with a various void fraction of gas. While the minimum film boiling temperature increases and minimum heat flux decreases.

Wang et al., (1989) did the analytical study on the heat transfer between an axis-symmetrical impinging jet and a solid flat surface with non-uniform surface temperature or heat flux. They found that increment of the surface temperature or heat flux with radial distance reduction in the stagnation point Nusselt number and vice-versa.

When the liquid jet impinges on the surface from the downward face, then observation of the flow behavior and investigation of the heat flux (Figure 11) is important. Thus, Woodfield et al., (2005) studied the different flow pattern for different wall-superheat as shown in Figure 11.

They used the microphone to hear the boiling sound. When the initial temperature was above 300 °C, the explosive sound heard. This phenomenon was observed because of the fact that, liquid sheet flow structure destroyed due to the abrupt formation of bubbles at high wall superheat. When the wall superheat went down to 300 °C, a liquid sheet structure observed and the change in the boiling sound accompanied. When the liquid sheet appeared this signified the higher heat transfer rate than the explosive structure of the boiling.

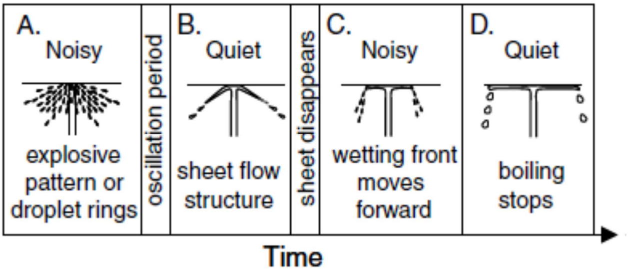

Figure 11 – Phenomenological history during quenching [Woodfield et al., (2005)]

In this quenching process, buoyancy influences the flow structures and heat transfer mechanism. The remarkable work done by Papell (1971) determined experimentally the effect of the buoyancy on the flow boiling of liquid hydrogen using the vertical test plate with up-flow and down-flow. The influence of buoyancy on a vertical flowing film boiling system found at low heat flux transition from the nucleate to film boiling prematurely; same heat flux supports nucleate boiling for up-flow.

The study of buoyancy on the flat surface quenching through jet impingement from the downward would be one of the parameters.

Very few works on numerical simulation of the quenching through the liquid jet are reported in the literature, because of the complex mechanism, only empirical correlations developed to quantify the heat transfer rate. However, some of the researchers have contributed towards the enhancement of the understanding of the phenomena. Hatta and Osakabe [Osakabe (1989)] considers the laminar water curtains are impinging onto the steel plate for the numerical modeling. The laminar jet impinged onto the plate, and heat transfer led to the film boiling phenomena for quenching. It implies that the inertia force of the water jet in not enough to penetrate the vapor film formed near the heated surface. In industrial case, the water jet is always turbulent in nature as the jet Reynolds number is in the range of 30,000-50,000. Therefore, enough inertia of liquid can penetrate the vapor film, and film boiling cannot exist, and even at high wall-superheat nucleate boiling can be established. Furthermore, nucleate boiling exhibited the more heat-flux than film boiling.

Hatta et al., (1989) did the numerical study on the quenching process of the heated steel plates by the water curtains. The numerical model gave quite satisfactory results with the measured value. However, they were unable to quantify the different boiling phenomena during the process in detail. Because of quenching phenomenon is very much transient in nature. Therefore, it is necessary to reveal the phenomena to understand the cooling process.

Timm et al., (2003) proposed the mechanistic model for the jet impingement boiling phenomena. They assumed that due to the high wall superheat (> 800°C) large population of the vapor bubble generated near the surface and viscous sub layer could not exist. Furthermore, they took advantage of the Prandtl mixing length model to analyze the phenomena.

Due to the growth, collapse, and the explosion of the bubbles created additional diffusivity in the flow. They emphasized on the fact that, one need more information about the bubble dynamics to improve the prediction of heat-flux. However, on the contrary, in the case of temperature controlled boiling the transition boiling phenomena, where heat flux decreases with increasing wall superheat, the mechanistic model by Timm et al., (2003) is unable to predict the heat flux. However, the concept of this model successfully implemented for the nucleate boiling by Omar et al., (2009).

2.9. Multiple jet impingement onto the flat surface

Quenching of heated surface through multiple liquid jets have [Liu and Samarasekera (2004), Sengupta et al., (2005)] many industrial applications to achieve the desirable product quality. Mainly in the steel industry, new technologies emerge [Hermann (2001), Sekiguchi et al. (2004), Kromhout et al. (2006)] results in lower production costs, improves product quality, to fulfill the increased demands of the developing countries for infrastructure development. For example, production of the high-strength steel is achieved with less alloying elements. Several technologies [Akio et al. (2002), Sun et al. (2002), Lucas et al. (2004)] employs to increase the quenching rate in the Run-Out-Table (ROT) milling process. Very high rate of quenching can produce high strength of the steel, because, the formation of Martensitic steel [Akio and Kazuo (2005)] depending on the plate thickness. Therefore, in order to envisage the phenomena in details; it has been realized that there are several parameters like mass-flow rate, plate width, nozzle to plate spacing, nozzle configuration. onto which the heat transfer coefficient depends on [Sun et al. (2002), Smith and Weinzierl (2007)].

It is evident from the experiment [Chong et al., (2008)] that in the case of multiple liquid jet impingement onto the isothermal surface, liquid pool develops on it. Chong et al., (2008) experimentally and numerically studied the hydrodynamics of multiple water jet impingement on Run-Out-Table (ROT) quenching process. They found that the water pool-height on the surface increases with increasing the water flow rate and width of the surface, while, static pressure at the jet stagnation region decreases.

The pool-height, flow-rate, and static pressure implicitly affect the mechanism of the heat-transfer. In the case of the single jet impinging onto the heated surface

(<600°C), then just after impingement (within ten milliseconds), transient boiling phenomena visualized with some explosion pattern of the bubble dynamics [Woodfield et al. (2005)]. The question arises that, what happens when multiple jets impinge onto the heated surface. What heat-transfer mechanism takes place at the temperature of the surface more than 600°C? Until now there is no such experiment exist in the literature as being the complex phenomena to predict the mechanism, because, its dependencies on so many parameters are non-linear in nature. Initially, the bubble formation is high, as the time elapses, its formation rate decreases and the liquid pool started to develop on the surface. Due to the high temperature of the surface, bubble began to form within the liquid pool. The bubble dynamics is a function of the density of nucleation site on the surface plays a crucial role in extracting heat flux from the heated surface. The density of nucleation site is a function of surface roughness and types of the granular surface. In the case of, high surface roughness and mixed type of surface structure in the processed metal block the nucleation site density is greater than the smooth and polished surface. This large number of bubbles convey a large amount of heat-flux. Therefore, the dynamics of the bubbles are necessary to study.

Hatta and Osakabe (1989) proposed a model for the temperature change of quenching of moving steel through the laminar water curtain. They also investigated the effect of the surface velocity on the cooling intensity. They said that there was certain surface velocity at which the cooling intensity was minimum. The critical velocity found for determining whether the film boiling occurs or not. This model did not take into account the turbulent diffusivity and did not envisage the boiling phenomena in detail.

Tsay et al., (1996) carried out an experimental investigation of the pool boiling heat transfer. They took the water at saturation temperature and found enhancement of the heat transfer for the rough surface and decrement when the stainless steel screen covers the heated surface, and the screen size was comparable to the bubble departure diameter. When they decreased the level of water from 60 to 5 mm, decreased the heat transfer rate. This study will help to the development of the heat transfer model for many jets impinge on the heated surface.

Rivallin and Viannay (2001) reported the general principle for the controlled cooling in the metallurgical process. They developed the theoretical model for the forced convection through sub-cooled water in the film boiling regime and correlated with experiment. They found the film boiling plays a role to quench the surface.

3. Mathematical Modeling

In this research work, the *Eulerian* technique is used to describe the flow. The basic concept of this approach is to observe the flow properties from a fixed location about a reference frame. The reference frame can be stationary or more generally moves at its own velocity. The *Eulerian* approach gives the values of the fluid variable at a given point (x, y, z) at a given time t. For example, the velocity can be expressed as $V = V(x, y, z, t)$, where x, y, and z are independent of t.

Since the *Eulerian* approach is consistent with conventional experimental observation techniques, therefore adopted for mathematical formulations in the present work [Fagari and Zhang (2010)].

In order to mathematical formulations of the multiphase flow, there are three Euler-Euler approaches of multiphase models listed in the order of increasing accuracy:

- Homogeneous (Equilibrium) Model
- Multi-fluid Model
- Volume-of-Fluid (VOF) Free-Surface Model

The homogeneous model is the least accurate multiphase model based on the Euler-Euler approach. A volume fraction equation is computed for each phase. However, only a single momentum equation is solved for the phases in momentum equilibrium.

In the multi-fluid model, all conservation equations are solved for each phase. From the numerical perspective, the Volume-of-fluid (VOF) model is very similar to the homogeneous model. A single momentum equation is computed for all phases that interact using the VOF model. However, the calculation of volume fraction equations using VOF model is considerably more accurate allowing the sharp resolution of the interfaces. One of the common defects of the VOF calculation can occur when the interface is not resolved sharply despite the use of the high-order discretization techniques for the volume fraction equation – in that case, the VOF model degenerates into the homogeneous model. This is quite common in many practical calculations. It happens due to very high-resolution requirements of the VOF model that can often be hard to fulfill.

In this research work, multi-fluid model and VOF (Volume of Fluid) methods are used for the formulations of the governing equations based on the requirement.

Now, in the next section, the *Eulerian* averaging technique is described.

3.1. *Eulerian* averaging

In this research work, the objective is to obtain the *Eulerian* averaging of the governing equations that are solved to predict the macroscopic properties of the multiphase system. Here, it is important to list the salient features of *Eulerian* averaging formulations: which is given below.

- It is consistent with the control volume analysis.
- It is based on the time-space description of physical phenomena.
- Changes in the various dependent variable can be expressed as functions of independent variables.
- The integral operations smooth out the local spatial or instant variations of the properties within the domain of integration.

The Eulerian time average for a function $\Phi = \Phi(x, y, z, t)$, is obtained by averaging the flow properties over a certain period of time, Δt, at a fixed point in the given frame of reference.

$$\overline{\Phi} = \frac{1}{\Delta t}\int_{\Delta t} \Phi(x, y, z, t)dt \tag{3.1}$$

In the above equation (3.1) Δt is larger than the largest time scale of the local properties. During this period, different phases can flow through the fixed point. Eulerian time averaging is predominantly suitable for a turbulent multiphase flow.

Eulerian volumetric averaging is done over a volume element, ΔV, around a point (*x, y, z*) in the flow. For a multiphase system, that includes Π different phases, the total volume equals the summation of the individual phase volumes, i.e.

$$\Delta \mathrm{V} = \sum_{\mathrm{k}=1}^{\Pi} \Delta \mathrm{V}_{\mathrm{k}} \tag{3.2}$$

The volume fraction of the k^{th} phase α_k, is defined as the ratio of the elemental volume of the k^{th} phase to the total elemental volume for all phases, i.e.,

$$\alpha_k = \frac{\Delta V_k}{\Delta V} \tag{3.3}$$

The volume fraction of all phases must sum to unity:

$$\sum_{k=1}^{\Pi} \alpha_k = 1 \tag{3.4}$$

Eulerian volume averaging can be written as

$$\langle \Phi \rangle = \frac{1}{\Delta V} \sum_{k=1}^{\Pi} \int_{\Delta V_k} \Phi_k(x, y, z, t) dV \tag{3.5}$$

Intrinsic phase average

$$\langle \Phi_k \rangle^k = \frac{1}{\Delta V_k} \int_{\Delta V_k} \Phi_k dV \tag{3.6}$$

Extrinsic phase average

$$\langle \Phi_k \rangle = \frac{1}{\Delta \mathrm{V}} \int_{\Delta V_k} \Phi_k dV \tag{3.7}$$

Here, the intrinsic phase average is the inherent part of a phase and is independent of another phase in the volume element. In contrast, extrinsic phase average is a property that depends on the phase's relationship with other phases in the volume element.

While the intrinsic phase average is taken only over the volume of the k^{th} phase in equation (3.6), the extrinsic phase average for a particular phase is taken over an entire elemental volume in equation (3.7). These two phase-averages are related by:

$$\langle \Phi_k \rangle = \alpha_k \langle \Phi_k \rangle^k \tag{3.8}$$

The intrinsic and extrinsic phase averages defined in equations (3.6) and (3.7) are related to the volume average defined in equation (3.5) by:

$$\langle \Phi \rangle = \sum_{k=1}^{\Pi} \langle \Phi_k \rangle = \sum_{k=1}^{\Pi} \alpha_k \langle \Phi_k \rangle^k \tag{3.9}$$

The deviation from a respective intrinsic phase-average value can be written as:

$$\widehat{\Phi}_k = \Phi_k - \langle \Phi_k \rangle^k \tag{3.10}$$

When the product of two variables ~~are~~ is phase-average, the following relations are used for derivation:

$$\langle \Phi_k \Psi_k \rangle^k = \langle \Phi_k \rangle^k \langle \Psi_k \rangle^k + \langle \widehat{\Phi}_k \widehat{\Psi}_k \rangle^k \tag{3.11}$$

$$\langle \Phi_k \Psi_k \rangle = \alpha_k \langle \Phi_k \rangle^k \langle \Psi_k \rangle^k + \langle \widehat{\Phi}_k \widehat{\Psi}_k \rangle \tag{3.12}$$

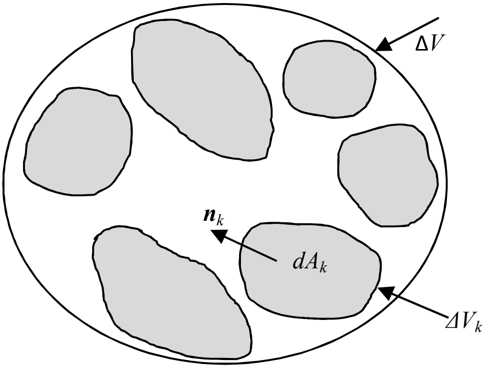

Figure 12 – Control volume for volume averaging

For a control volume ΔV shown in Figure 12 the volume averaging of the partial derivative with respect to time is obtained by the following general transport theorem:

$$\langle\frac{\partial\Omega_k}{\partial t}\rangle = \frac{\partial\langle\Omega_k\rangle}{\partial t} - \frac{1}{\Delta V}\int_{A_k}\Omega_k\boldsymbol{V}_I \cdot \boldsymbol{n}_k dA_k \tag{3.13}$$

Where A_k is the interfacial area surrounding the k^{th} phase within control volume ΔV, ΔV_k is the volume occupied by the k^{th} phase in the control volume and ΔV, $\boldsymbol{V}_I$is the interfacial velocity, and $\mathbf{n}_k$ is the unit normal vector at the interface directed outward from phase k (Figure 12).

The volume average of the gradient is

$$\langle\nabla\Omega_k\rangle = \nabla\langle\Omega_k\rangle + \frac{1}{\Delta V}\int_{A_k}\Omega_k\mathbf{n_k}dA_k \tag{3.14}$$

moreover, the volume average of a divergence is

$$\langle\nabla\cdot\Omega_k\rangle = \nabla\cdot\langle\Omega_k\rangle + \frac{1}{\Delta V}\int_{A_k}\Omega_k\cdot\mathbf{n_k}dA_k \tag{3.15}$$

3.2. Computational model for multi-fluid flow with phase change

The computational model describing the two-phase flow in the fluid region relies on solving the mass, momentum and energy equations simultaneously. At this moment, the two-fluid model is being applied for multiphase flow calculation. In the framework of this method, the motion of both phases, considered as two interpenetrating continuum media, is described by a particular set of transport equations relying upon the corresponding conservation laws. In the solid region, only the energy equation described the heat conduction process.

3.2.1. Mass Conservation

The volume-averaged form of the continuity equation for the k^{th} phase reads

$$\frac{\partial(\alpha_k\langle\rho_k\rangle^k)}{\partial t} + \nabla\cdot\left(\alpha_k\langle\rho_k\rangle^k\langle\vec{V}_k\rangle^k\right) = \sum_{j=1(j\neq k)}^{\Pi}\dot{m}_{jk} \tag{3.16}$$

The volume fraction satisfying the condition of the compatibility: $\sum_{k=1}^{\Pi}\alpha_k = 1$.
The modeling of the source term originating from the phase change taking place due to heat transfer between the fluid and the heated surface (quenched surface) is the subject of the following section.

3.2.2. Quenching Model

The afore-mentioned mass transfer rate between the liquid and the vapor generated by the presence of the quenched solid part, in which the temperature field simultaneously investigated, defined as follows:

$$\dot{m}_{jk} = \frac{C_A C_m h A_i \Delta T}{h_{fg}} = -\dot{m}_{kj} \tag{3.17}$$

Where, h is the heat transfer coefficient existing in the relevant boiling mode; $\Delta T=T_w-T_{sat}$ is the excess wall temperature, T_w being the wall temperature and T_{sat} the liquid saturation temperature. The area considered in the boiling model is given as $A_i = 6\varepsilon_d/D_b$, with D_b ($=0.1$ *mm* is the typical value) being the bubble diameter and ε_d dispersed phase volume fraction. C_m represents the vapor formation coefficient in the film boiling mode (taking the value of 100) and the vapor collapse coefficient in the transition to nucleate boiling stage (with the corresponding value of 20). The closure coefficient C_A is given by the following relationship

$$c_A = 1 - \sqrt{\frac{\alpha_d + \alpha_{min}}{\alpha_{pack} - \alpha_{min}}}$$

The heat transfer coefficient corresponding to the film boiling mode is computed by using Bromley's (1955) equation.

$$h = 0.62\left[\frac{k_v^3\rho_v(\rho_l-\rho_v)g\left(h_{fg}+0.4C_{pv}\Delta T\right)}{D_b\mu_v\Delta T}\right]^{0.25} \tag{3.18}$$

To evaluate the heat transfer coefficient in the transition boiling regime and to identify the limits of the phase change rates, the Critical Heat Flux (CHF) and Minimum Heat Flux (MHF) limits are evaluated based on the properties of the interacting phases. An estimation of the critical heat flux value pertaining to the current system is established by using Zuber's (1958) relation.

$$Q_{CHF} = 0.131\rho_v h_{fg}\left[\frac{\sigma g(\rho_l-\rho_v)}{\rho_v^2}\right]^{0.25} \tag{3.19}$$

With σ representing the surface tension of the liquid. The effect of sub-cooling is taken into account using the relation of Hua and Xu (2000) as following.

$$\frac{Q_{CHF,subcool}}{Q_{CHF,sat}} = 1 + 0.345\frac{Ja}{Pe^{0.25}} \tag{3.20}$$

A constant 'transient critical heat flux factor,' K_{chf}, is provided to identify the effect of transient burn out approximation [Auracher and Buchholz (2005)] on the CHF during the quenching process. The modified Critical Heat Flux value is computed as following.

$$Q_{CHF,subcool} = K_{chf}Q_{CHF,sat}\left(1 + 0.345\frac{Ja}{Pe^{0.25}}\right) \tag{3.21}$$

Where *Ja* and *Pe* are the *Jacob* and *Peclet* numbers respectively. The value of K_{chf} is taken between *0.5 – 4.0*. The Minimum Heat Flux (MHF) approximation in the quenching system is estimated as:

$$Q_{MHF} = 0.09\rho_v h_{fg}\left[\frac{g(\rho_l-\rho_v)}{\rho_l+\rho_v}\right]^{0.5}\left[\frac{\sigma}{g(\rho_l-\rho_v)}\right]^{0.25} \tag{3.22}$$

Similar to the burn out approximation factor, a constant 'transient minimum heat flux factor,' K_{mhf}, is introduced to describe the variations in the computed minimum heat flux owing to the local fluctuations, boundary layer modulation, and solid surface characteristics. Accordingly, the modified Minimum Heat Flux reads.

$$Q_{MHF} = K_{mhf} Q_{MHF} \tag{3.23}$$

The range of the variation of the K_{mhf} values is 2-15. The heat flux experienced during the transition boiling (TB) mode in the near-wall region is.

$$Q_{TB} = Q_{CHF} \left[w_p \frac{T_{chf}}{(T_w - T_{chf})} \right] \tag{3.24}$$

Where T_{chf} is the temperature value taken at the Critical Heat Flux limit. Q_{CHF} is defined using equation (3.19). The parameter w_p, defined as the wetting parameter, provides the instantaneous flux disposition when the wall temperature drops below the Leidenfrost temperature limit. In the following equation, the heat transfer coefficient in the nucleate boiling (NB) regime is obtained by presuming the similar relationship as for the transition boiling mode ($Q_{NB} \approx Q_{TB}$)

$$h_{NB} = \frac{Q_{NB}}{T_w - T_{sat}} \tag{3.25}$$

The limits of phase change process during the film and nucleate boiling modes are given by the following.

$$\Gamma_{lim}^{i} = \frac{Q_i A_{wet}}{h_{fg}} \tag{3.26}$$

With i denoting the critical heat flux ($i \equiv CHF$) in the nucleate boiling mode and minimum heat flux ($i \equiv MHF$) in the film boiling mode. The corresponding CHF and MHF limits, given by equation (3.21) and (3.22) respectively, are to be inserted here. A_{wet} represents the wetted area given by

$$A_{wet} = (1 - \varepsilon_{pack}) A_s \tag{3.27}$$

A_s in equation (3.27) denotes the physical interface area exposed to the boiling process. α_{pack} is the phase packing limit defined by

$$\alpha_{pack} = \alpha_{dry} + F\alpha_{wet} \tag{3.28}$$

Factor F takes the value of 1 if the interface temperature is less than the Leidenfrost temperature (nucleate boiling mode) or 0 otherwise (film boiling mode). α_{dry} and α_{wet} are the dry and wet phases packing limits.

3.2.3. Momentum Equation

The intrinsic volume-averaged momentum equation for the k^{th} phase is given by

$$\frac{\partial\left(\alpha_k\langle\rho_k\rangle^k\langle\vec{V}_k\rangle^k\right)}{\partial t}+\nabla\cdot\left(\alpha_k\langle\rho_k\rangle^k\langle\vec{V}_k\vec{V}_k\rangle^k\right)=$$

$$-\langle p_k\rangle^k I+\nabla\cdot(\alpha_k\langle\tau_k+T_k^t\rangle)-\frac{1}{\Delta\vartheta}\int_{A_k}\rho_k\vec{V}_k\left(\vec{V}_k-\vec{V}_I\right)\cdot n_k dA_k+\frac{1}{\Delta\vartheta}\int_{A_k}\tau_k\cdot n_k dA_k$$

(3.29)

Where, $\langle\tau_k\rangle^k$ is the phase-averaged stress tensor of the k^{th} phase,

$$\langle\tau_k\rangle^k=\mu_k\left[\nabla\langle\vec{V}_k\rangle+\left(\nabla\langle\vec{V}_k\rangle^k\right)^T\right]-\frac{2}{3}\mu_k\left(\nabla\cdot\langle\vec{V}_k\rangle^k\right)I \tag{3.30}$$

$$\langle T_k^t\rangle^k=-\rho_k\langle\overline{v_i'v_j'}\rangle_k=\mu_k^t\left[\left(\nabla\langle\vec{V}_k\rangle+\left(\nabla\langle\vec{V}_k\rangle^k\right)^T\right)-\frac{2}{3}(\nabla\cdot\langle V_k\rangle^k)I\right]-\frac{2}{3}\,\rho_k\langle K_k\rangle^k I$$

(3.31)

The turbulent viscosity

$$\mu_k^t=\rho_k C_\mu\zeta\frac{\boldsymbol{K}_{\mathrm{k}}^2}{\varepsilon_k} \tag{3.32}$$

The third and fourth terms on the right-hand side of equation (3.29) represent the momentum exchanges and interactive forces between the phases:

$$-\frac{1}{\Delta\vartheta}\int_{A_k}\rho_k\,\vec{V}_k\left(\vec{V}_k-\vec{V}_I\right)\cdot n_k\,dA_k=\sum_{j=1(j\neq k)}\left(\langle\dot{m}_{jk}\rangle\langle V_{k,I}\rangle\right) \tag{3.33}$$

$$\frac{1}{\Delta\vartheta}\int_{A_k}\tau_k\cdot n_k dA_k=\sum_{j=1(j\neq k)}^{\Pi}\langle\vec{F}_{jk}\rangle \tag{3.34}$$

Here, $\langle\vec{V}_{k,i}\rangle^k$ is the intrinsic volume-averaged velocity of the k^{th} phase at the interface. The velocity difference between two adjacent phases results solely from their density difference. $\vec{F}_{jk}$ is an interactive force between the j^{th} and k^{th} phases depending upon the friction, pressure and cohesion between different phases. Newton's third law requires that the contact interaction forces (action and reaction force pair) satisfy the conditions

$$\langle\vec{F}_{jk}\rangle=-\langle\vec{F}_{kj}\rangle \tag{3.35}$$

The interactive force can be determined by:

$$\langle \vec{F}_{jk} \rangle = M_{e,jk}\left(\langle \vec{V}_j \rangle^j - \langle \vec{V}_k \rangle^k\right) \tag{3.36}$$

$M_{e,jk}$ representing the momentum exchange coefficient between phases j and k. If liquid is the primary phase and vapor is the secondary phase, the vapor disperses in liquid as vapor bubbles. The momentum exchange coefficient can be than estimated by following equations:

$$M_{e,\ jk} = \frac{3}{4} C_D \frac{\alpha_j \langle \rho_k \rangle}{D_b} \left| \langle \vec{V}_j \rangle^j - \langle \vec{V}_k \rangle^k \right| \tag{3.37}$$

Where k denotes the primary phase and j the secondary phase. D_b is the diameter of the vapor bubbles or liquid droplets of the secondary phase j. C_D is the drag coefficient based on the relative Reynolds number, which is obtained from the following empirical correlation:

$$C_D = \begin{cases} \frac{24}{Re_b}\left(1 + 0.15 Re_b^{0.687}\right) & if \quad Re_b \leq 1000 \\ 0.44 & if \quad Re_b > 1000 \end{cases} \tag{3.38}$$

$$Re_b = \frac{\langle \rho_k \rangle \left| \langle \vec{V}_j \rangle^j - \langle \vec{V}_k \rangle^k \right| D_b}{\mu_j} \tag{3.39}$$

Introduction to the equations (3.33) - (3.34) into equation (3.29) results in the final form of the volume-averaged, multi-fluid momentum equation, applied in the present work:

$$\frac{\partial\left(\alpha_k \langle \rho_k \rangle^k \langle \vec{V}_k \rangle^k\right)}{\partial t} + \nabla \cdot \left(\alpha_k \langle \rho_k \rangle^k \langle \vec{V}_k \vec{V}_k \rangle^k\right) =$$
$$-\langle p_k \rangle^k I + \nabla \cdot \left(\alpha_k \langle \tau_k + T_k^t \rangle\right) + \sum_{j=1(j\neq k)} \langle \dot{m}_{jk} \rangle \langle \vec{V}_{k,I} \rangle^k + \sum_{j=1(j\neq 1)}^{\Pi} \langle \vec{F}_{jk} \rangle \tag{3.40}$$

3.2.4. Energy Equation

The intrinsic volume-averaged energy equation for the k^{th} phase is given as follows

$$\frac{\partial\left(\alpha_k \langle \rho_k \rangle^k \langle H_k \rangle^k\right)}{\partial t} + \nabla\left(\alpha_k \langle \rho_k \rangle^k \langle \vec{V}_k H_k \rangle^k\right) = -\nabla \langle q_k + q_k^t \rangle + \alpha_k \frac{D \langle p_k \rangle^k}{Dt} + \nabla \langle \vec{V}_k \rangle : \langle \tau_k \rangle -$$
$$\frac{1}{\Delta\vartheta} \int_{A_k} \rho_k H_k \left(\vec{V}_k - \vec{V}_I\right) \cdot n_k dA_k - \frac{1}{\Delta\vartheta} \int_{A_k} q_k \cdot n_k dA_k \tag{3.41}$$

The next to last term on the right-hand side of equation (3.41) represents the enthalpy exchange between the k^{th} phase and other participating phases featured by the ongoing mass transfer:

$$-\frac{1}{\Delta\vartheta}\int_{A_k}\rho_k H_k\left(\vec{V}_k-\vec{V}_I\right)\cdot n_k dA_k=\sum_{j=1(j\neq k)}^{\Pi}\dot{m}_{jk}\langle H_{k,I}\rangle^k \tag{3.42}$$

Where,$\langle H_{k,I}\rangle^k$ is the intrinsic volume-averaged enthalpy of the k^{th} phase at the interface. The last term on the right hand side of equation (3.41) describes the heat transfer between the k^{th} phase and all other participating phases:

$$-\frac{1}{\Delta\vartheta}\int_{A_k}q_k\cdot n_k dA_k=\sum_{j=1(j\neq k)}^{\Pi}\langle q_{jk}\rangle^k \tag{3.43}$$

The important heat exchange process is based on the Ranz- Marshall (1952) correlation for the Nusselt number, *Nu*:

$$Nu=2.0+0.6Re_b^{1/2}Pr^{1/3} \tag{3.44}$$

Where Re_b is the local bubble Reynolds number and *Pr* is the Prandtl number. This model should also be used when the Ranz-Marshall correlation is employed for the calculation of mass exchange due to boiling process.

The heat transfer rate becomes:

$$\langle q_{jk}\rangle=C\frac{\kappa_c}{D_b}Nu\cdot A_i\cdot(T_d-T_c)=-\langle q_{kj}\rangle \tag{3.45}$$

Presently, $C_b = 1$ and $C_c = 0$ were adopted (boiling and condensation coefficients respectively). κ_c represents the conductivity of the continuous phase. T_d and T_c are the temperatures of the dispersed and continuous phases respectively. The final form of the energy equation solved presently is as follows:

$$\frac{\partial\left(\alpha_k\langle\rho_k\rangle^k\langle H_k\rangle^k\right)}{\partial t}+\nabla\left(\alpha_k\langle\rho_k\rangle^k\langle\vec{V}_k H_k\rangle^k\right)=-\nabla\cdot\langle q_k+q_k^t\rangle+\alpha_k\frac{D\langle p_k\rangle^k}{Dt}+\nabla\langle\vec{V}_k\rangle:\langle\tau_k\rangle+\sum_{j=1(j\neq k)}^{\Pi}\left[\langle q_{jk}\rangle+\dot{m}_{jk}\langle H_{k,I}\rangle^k\right] \tag{3.46}$$

Heat flux q_k is defined as:

$$q_k=\frac{\kappa_{c,\ k}}{C_{p,k}}\nabla\cdot\langle H_k\rangle^k \tag{3.47}$$

Where $\kappa_{c,\ k}$ is the thermal conductivity and C_{pk} is the heat capacity of k^{th} phase.

Turbulent heat flux q_k^t equals:

$$q_k^t = -\rho_k \langle \overline{v_\imath' H_\jmath'} \rangle_k = \frac{\mu_k^t}{\sigma_T} \nabla \cdot \langle H_k \rangle^k \quad (3.48)$$

3.2.5. Heat Conduction Equation for the Solid Region

The heat transfer (conduction) computation in the solid region is based on the solution of an appropriate enthalpy equation.

$$\langle \frac{\partial(\rho_s H_s)}{\partial t} \rangle = -\langle \nabla \cdot q_s \rangle \quad (3.49)$$

The heat flux formulation is given as $q_s = \frac{\kappa_s}{C_{ps}} \nabla H_s$

3.3. Computational model for multi-fluid flow without phase change

The hydrodynamics and convection heat transfer of jet impingement onto the flat horizontal surface used the following model for computational study.

Mass balance:

$$\frac{\partial(\alpha_k \langle \rho_k \rangle^k)}{\partial t} + \nabla \cdot \left(\alpha_k \langle \rho_k \rangle^k \langle \vec{V}_k \rangle^k \right) = 0 \quad (3.50)$$

Momentum Balance:

$$\frac{\partial(\alpha_k \langle \rho_k \rangle^k \langle \vec{V}_k \rangle^k)}{\partial t} + \nabla \cdot \left(\alpha_k \langle \rho_k \rangle^k \langle \vec{V}_k \vec{V}_k \rangle^k \right) = -\langle p_k \rangle^k I + \nabla \cdot (\alpha_k \langle \tau_k + T_k^t \rangle^k) \quad (3.51)$$

The volume fraction satisfying the condition of the compatibility: $\sum_{k=1}^{\Pi} \alpha_k = 1$

Where, $\langle \tau_k \rangle^k$ is the phase-averaged stress tensor of the k^{th} phase.

VOF (Volume-of-Fluid) method is used only in the case of multiple jets or the jet without phase change. The VOF method proposed by Hirt and Nichols (1981) is used to capture the free surface of the water jet.

The volume fraction of the tracked phase can be written in the conservative form as:

$$\frac{\partial \alpha}{\partial t} + \nabla \cdot \alpha \vec{V} = 0 \quad (3.52)$$

Where ε is the volume fraction of the tracked phase and $\vec{V}$ is the velocity field. A computational cell can be associated with the value α =1, if fully occupied by the tracked phase, otherwise α = 0. In the partially filled cells the volume fraction takes the values *0<* α *<1*. A single set of governing equations is solved for the "effective" fluid representing a mixture of the participating phases. The local density and viscosity of this mixture occupying the whole computational domain are defined with help of the following volumetric-fraction-weighted relationships, with the subscripts j and k denoting the different phases.

$$\rho_m = \alpha\rho_j + (1-\alpha)\rho_k \tag{3.53}$$

$$\mu_m = \alpha\mu_j + (1-\alpha)\mu_k \tag{3.54}$$

3.3.1. Volume-of-fluid interfacial momentum exchange model

In the flows with the interface, surface tension on the interface plays a significant role. Continuum-surface-force model is employed and treated as body force:

$$\mathrm{f}_\sigma = \int_{\mathrm{V}} \sigma\,\kappa\nabla\alpha\,d\mathrm{V} = \sigma\kappa_P(\nabla\alpha)_P\mathrm{V}_P \tag{3.55}$$

Where, σ is surface tension, κ_P is the curvature of the interface calculated from the following expression:

$$\kappa_P = -(\nabla\cdot\hat{n}) = -\left[\nabla\cdot\left(\frac{\nabla\alpha}{|\nabla\alpha|}\right)\right]_P = -\frac{1}{\mathrm{V}_p}\sum_{j=0}^{n_f}\mathrm{S}_j\cdot\left(\frac{(\nabla\alpha)_f}{|\nabla\alpha|_f}\right) \tag{3.56}$$

Where, $\hat{n}$ is unit normal to the surface. An accurate evaluation of the curvature using (3.56) demands the smoothing of the volume fraction field (which is discontinuous on a discretized mesh without smoothing). This task can be achieved by applying the Laplacian filter several times, defined as:

$$\Im(\alpha)_\mathrm{P} = \sum_{\mathrm{j}=1}^{\mathrm{n_f}}\alpha_\mathrm{f}\left|\mathbf{s}_\mathrm{j}\right| / \sum_{j=1}^{\mathrm{n}}\left|\mathbf{s}_\mathrm{j}\right|$$

(3.57)

When fluid interfaces are in contact with wall boundaries, the effects of wall adhesion must be accounted. The simplest approach within the framework of the CSF model is to adjust the normal vector to the interface according to the contact angle θ_w (the angle between the wall and the tangent to the interface at the wall, measured inside the tracked phase).

At points $\vec{\mathrm{X}}_\mathrm{w}$ on the wall, the unit normal vector can be expressed as:

$$\hat{\mathrm{n}} = \hat{\mathrm{n}}_{\mathrm{wall}}\cos\theta_\mathrm{w} + \hat{\mathrm{n}}_\mathrm{t}\sin\theta_\mathrm{w} \tag{3.58}$$

$\hat{\mathrm{n}}_{\mathrm{wall}}$ is the unit wall normal directed into the wall and is computed from the geometry, whereas, $\hat{\mathrm{n}}_{\mathrm{t}}$ lies on the wall and is normal to the contact line between the interface and the wall at $\vec{\mathrm{X}}_{\mathrm{w}}$.

The value of $\hat{\mathrm{n}}_{\mathrm{t}}$ is computed from the known volume fraction field by applying the symmetry condition at the wall boundary. Once, $\hat{\mathrm{n}}$ is evaluated using (C), it is substituted in the curvature expression (3.56) as a boundary condition for the cells near the wall. This change in curvature, in turn, modifies the surface tension (3.55) near the wall (dynamic treatment).

In reality, the physics associated with wall adhesion is very complex - the contact angle θ_w is not only a fluid property but also a function of the geometry and smoothness of the wall surface. Besides, when the contact line is moving, it depends on the local fluid conditions as well, and additional modeling is necessary.

3.4. Turbulence and its modeling

It is evidence from the experiment [Islam et al. (2008), Mitsutake and Monde (2003), Nishio et al. (1998)] that heat transfer mechanism at the surface which is being quenched by liquid jet is governed by turbulent diffusion caused by dynamics (bubble growth, merger, and collapse) of vapour bubbles. A pioneer work by Paul Durbin [Durbin, 1993)] demonstrated the fact that, the standard k-ε model over predicts the heat-flux and developed the new $\overline{v^2} - f$ model which shows some improvements.

In order to improve numerical stability of the original $\overline{v^2} - f$ model by solving a transport equation for the velocity scale $\zeta = \frac{\overline{v^2}}{k}$ instead of velocity scale $\overline{v^2}$. The variable ζ represents a scalar whose near-wall behaviour resembles that of the normal-to-wall Reynolds stress component.

Incorporating the Durbin's [Durbin, (1995)] elliptic relaxation concept, a new eddy-viscosity turbulence model comprising four equation denoted as $k - \varepsilon - \zeta - f$ developed by Hanjalic et al. (2004).

The eddy-viscosity is obtained in the following from:

$$\nu_t = C_\mu \zeta \frac{k^2}{\varepsilon} \tag{3.59}$$

moreover, the rest of variables from the following set of model equation, thus

$$\frac{\partial(\alpha_k \rho_k \mathrm{k}_k)}{\partial t} + \frac{\partial}{\partial x_j}(\alpha_k \rho_k \mathrm{v}_k \mathrm{k}_k) =$$

$$\frac{\partial}{\partial x_j}\left[\alpha_k \left(\mu_k + \frac{\mu_k^t}{\sigma_k}\right)\frac{\partial \mathrm{k}_k}{\partial x_j}\right] + \alpha_k \rho_k (\mathrm{P}_k - \varepsilon_k) + \sum_{i=1,j\neq k}^{\Pi} \mathrm{K}_{jk} + \mathrm{k}_k \sum_{i=1,j\neq k}^{\Pi} \dot{m}_{jk}$$

(3.60)

$$\frac{\partial(\alpha_k\rho_k\varepsilon_k)}{\partial t}+\frac{\partial}{\partial x_j}(\alpha_k\rho_k\mathrm{v}_k\varepsilon_k)=\frac{(C_{\varepsilon1}^{*}P_k\alpha_k\varepsilon_k-C_{\varepsilon2}\alpha_k\varepsilon_k^2)}{\mathrm{k}_k}+\frac{\partial}{\partial x_j}\left[\alpha_k\left(\mu_k+\frac{\mu_k^t}{\sigma_\varepsilon}\right)\frac{\partial\varepsilon_k}{\partial x_j}\right]+$$

$$\sum_{i=1,j\neq k}^{\Pi}\mathrm{D}_{jk}+\varepsilon_k\sum_{i=1,j\neq k}^{\Pi}\dot{m}_{jk}$$

(3.61)

$$\frac{\partial(\alpha_k\rho_k\zeta_k)}{\partial t}+\frac{\partial}{\partial x_j}(\alpha_k\rho_k\mathrm{v}_k\zeta_k)=\rho f-\rho\frac{\zeta}{k}P_k+\frac{\partial}{\partial x_j}\left[\alpha_k\left(\mu_k+\frac{\mu_k^t}{\sigma_\zeta}\right)\frac{\partial\zeta_k}{\partial x_j}\right] \tag{3.62}$$

Where the following form of the *f* equation is adopted as

$$f-L^2\frac{\partial^2 f}{\partial x_j\partial x_j}=\left(C_1+C_2\frac{P_k}{\zeta}\right)\frac{\left(\frac{2}{3}-\zeta\right)}{T} \tag{3.63}$$

The turbulent time scale *T* and length scale *L* are given by

$$T=max\left(min\left(\frac{k}{\varepsilon},\frac{\alpha k}{\overline{\upsilon^2}C_\mu\sqrt{6S^2}}\right),C_T\left(\frac{\nu}{\varepsilon}\right)^{1/2}\right) \tag{3.64}$$

$$L=C_L max\left(min\left(\frac{k^{3/2}}{\varepsilon},\frac{k^{3/2}}{\overline{\upsilon^2}C_\mu\sqrt{6S^2}}\right),C_\eta\left(\frac{\nu^3}{\varepsilon}\right)^{1/2}\right) \tag{3.65}$$

Additional modifications to the ε-equation is that the constant $C_{\varepsilon1}$ is dampened close to the wall thus

$$C_{\varepsilon1}^{*}=C_{\varepsilon1}\left(1+0.045\sqrt{1/\zeta}\right) \tag{3.66}$$

This is computationally more robust than the original model $\overline{v^2}-f$.

3.4.1. Hybrid Wall-treatment

This wall treatment should ensure a gradual change between viscous sub-layer formulations and the wall functions. Popovac and Hanjalic (2005) extended Kader's (1981) proposal for the description of temperature profile in the wall boundary layer also on all turbulence properties, thus

$$U^+=y^+e^{-\Gamma}+\frac{1}{\kappa}\ln(Ey^+)e^{-1/\Gamma} \tag{3.67}$$

$$\mu_w=\mu\frac{y_P^+}{U_P^+} \tag{3.68}$$

$$\Gamma=\frac{0.01(\mathrm{Pr}\,y^+)^4}{1+5Pr^3y^+} \tag{3.69}$$

This wall treatment provides the standard wall function for the large values of y^+ as well as the integration of equations up to the wall for the very small values of y^+. Similarly, the relationships for a dissipation rate and turbulence viscosity at the point next to the wall are derived. The production of turbulence kinetic energy near the wall is modified as well to ensure that results are the same for the small y^+ as provided by low-Re models and the results are the same as with the standard wall function for the high y^+. All models given above are implemented in conjunction with this wall treatment also.

3.5. Numerical Solution Methodology

3.5.1. Introduction

This section discusses numerical aspects of the method employed to solve the governing equations described in sections 3.2 and 3.3. First of all, the integral form of the modeling equations, which is the preliminary for the finite volume discretization, is presented. The fundamental features of the discretization method such as Linear Upwind Differencing Schemes (LUDS), time integration and basis of algebraic equations are delineated. The SIMPLE (Semi-Implicit Method for Pressure-Linked Equation) -like segregated method used to connect the momentum, continuity and energy equations (i.e. coupling between the velocities, pressure, and density) is essential to the whole procedure and is deliberated. Next, the overall solution procedure is presented, and the implementation of various boundary conditions is described.

3.5.2. Integral form of equations

The differential form of the generic conservation equation is given as:

$$\frac{\partial\left(\varepsilon_k\langle\rho_k\rangle^k\langle\phi_k\rangle^k\right)}{\partial t}+\nabla\cdot\left(\varepsilon_k\langle\rho_k\rangle^k\langle\vec{V}_k\phi_k\rangle^k\right)=\nabla\cdot\left(\varepsilon_k\Gamma_{\phi,k}\nabla\langle\phi_k\rangle^k\right)+\nabla\cdot\left(\varepsilon_k\boldsymbol{q}_{\boldsymbol{\phi S,k}}\right)+$$
$$\langle\phi_{k,I}\rangle^k\sum_{j=1(j\neq k)}^{\Pi}\langle\dot{m}_{jk}\rangle+\sum_{j=1(j\neq 1)}^{\Pi}\langle S_{\phi,kl}\rangle \tag{3.70}$$

The above equation integrated over the cell volume to provide the generic conservation equation in the integral form:

$$\frac{\partial}{\partial t}\int_V \varepsilon_\mathrm{k}\langle\rho_\mathrm{k}\rangle^k\langle\phi_\mathrm{k}\rangle^k dV_\mathrm{k}+\int_S \varepsilon_\mathrm{k}\langle\rho_\mathrm{k}\rangle^k\langle\vec{V}_k\phi_k\rangle^k\cdot\mathrm{ds}=\int_S \varepsilon_\mathrm{k}\Gamma_{\phi,k}\nabla\langle\phi_k\rangle^k\cdot\mathrm{ds}+$$
$$\int_S \varepsilon_\mathrm{k}\,\mathbf{q}_{\phi\mathrm{S,k}}\cdot\mathrm{ds}+\int_V\left(\langle\phi_{\mathrm{k},I}\rangle^k\sum_{j=1(j\neq\mathrm{k})}^{\Pi}\langle\dot{m}_{jk}\rangle+\sum_{j=1(j\neq 1)}^{\Pi}\langle S_{\phi,kl}\rangle\right)\mathrm{dV}$$
(3.71)

k= 1,….,N

3.5.3. Differencing Schemes

The governing equations are presently discretized by a scheme fulfilling the boundedness criterion. In the case of non-bounded results the 1st order Upwind Differencing Scheme (UDS) is employed, because this scheme is unconditionally bounded.
The convection boundedness criterion (CBC) of Gaskell and Lau (1988) is incorporated. Because of its flexibility in the construction of the higher-order (upwind) bounded scheme. The high-order upwind scheme is usually developed on structured grids along the local coordinate, which passes through the upstream (U), central (C) and downstream (D) computational nodes. In the case of the unstructured grids, the upstream node is not identified. However, an imaginary upstream cell U can be defined in such a way that the vector identity $\overrightarrow{CU} = -\overrightarrow{CD}$ is satisfied and that an imaginary face between C and U is placed at the same distance from C as the considered face j.

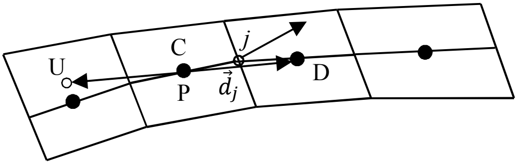

Figure 13 – Definition of Upstream (U), Central (C) and Downstream (D) Nodes

The three equations for ϕ at U, C and D is obtained by the Taylor-series expansion around j. A general upstream-weighted approximation for ϕ_j can be obtained as:

$$\phi_j = \phi_C + \left[\frac{1}{2} f_j^*\left(1 + f_j^*\right) - \alpha_j\right](\phi_D - \phi_C) + \left[\frac{1}{2} f_j^*\left(1 - f_j^*\right) + \alpha_j\right](\phi_C - \phi_U)$$
(3.72)

The parameter α_j defines a family of the second and third-order accurate schemes:

$$\alpha_j = 0.5 f_j^*\left(1 + f_j^*\right) \tag{3.73}$$

This is second-order accurate Linear Upwind Differencing Scheme (LUDS) of Warming and Beam (1976).

$$\nabla\phi_j = \nabla\widetilde{\phi}_j + \frac{\vec{A}_j}{\vec{A}_j \cdot \vec{d}_j}\left[\left(\phi_{pj} - \phi_p\right) - \nabla\widetilde{\phi}_j \cdot \vec{d}_j\right] \tag{3.74}$$

The cell face values are calculated by using linear interpolation (CDS), equation.

3.5.4. Time Integration

For unsteady fluid flow problems, the semi-discretized equation resembles a first order ordinary differential equation:

$$\frac{d\Psi}{dt} + \Phi(\phi, t) = 0, \;\; \Psi = (\rho V \phi)_P \tag{3.75}$$

In which all fluxes and sources are replaced by the quantity Φ:

$$\Phi = \sum_{j=1}^{n_f} C_j - \sum_{j=1}^{n_f} D_j - \left(S_\phi^V + \sum_{j=1}^{n_f} \left(S_\phi^A\right)_j\right) = C - D - S \tag{3.76}$$

In order to advance the solution method in time step by step (time 'marching' procedure) the above equation need to be integrated over each time interval Δt. Explicit methods used to evaluate the fluxes and sources contained in $\Phi(\phi, t)$. Explicit schemes involve a stability requirement that Courant number (defined for the 1D case as $U\,\Delta t/\Delta x$) should be less than unity. If this condition is violated, the solution becomes unstable.

3.5.5. Algebraic Equations

The outcome of the discretization procedure is a set of algebraic equations, which can be written in the form:

$$a_p \phi_p = \sum_{j=1}^{n_i} a_j \phi_{pj} + S_\phi \tag{3.77}$$

where n_i is the number of internal faces which make a volume around the computational node P. The central coefficient a_p, the coefficients a_j associated with the values of the dependent variable φ at neighboring nodes P_j and the source term S_ϕ are assembled as:

$$a_j = a_j^C + a_j^D = \max\left(-\dot{m}_j, 0\right) + \bar{\Gamma}_{\phi j} \frac{A_j^2}{\vec{A}_j \cdot \vec{d}_j} \tag{3.78}$$

$$a_P = \sum_{j=1}^{n_b} a_b + a_t + S_\phi \tag{3.79}$$

$$a_t = \frac{4(\rho V)_P^{n-1} - (\rho V)_P^{n-2}}{2\Delta t} \tag{3.80}$$

$$S_\phi = \sum_{j=1}^{n_i}\left[\gamma_\phi|\dot{m}_j|\phi_j\left(\phi_P - \phi_{P_j}\right) + \bar{\Gamma}_{\phi j}\overline{\nabla\phi_j}\cdot\left(\vec{A}_j - \frac{A_j^2}{\vec{A}_j\cdot\vec{d}_j}\vec{d}_j\right)\right] + \sum_{b=1}^{n_b}\left[a_b\phi_b + \Gamma_{\phi b}\nabla\phi_P\cdot\left(\vec{A}_b - \frac{A_b^2}{\vec{A}_b\cdot\vec{d}_b}\vec{d}_b\right)\right] + S'_\phi + \sum_{j=1}^{n_f}\left(S_\phi^A\right)_j + S_{\phi t}$$

(3.81)

$$S_{\phi t} = \frac{4(\rho V\phi)_P^{n-1} - (\rho V\phi)_P^{n-2}}{2\Delta t} \tag{3.82}$$

Note that the boundary coefficients a_b are defined in the same way as a_j, see equation (3.78). There are $n_b = n_f - n_i$ boundary faces for the given cell P. The second order explicit scheme is used to discretize for the unsteady term.

3.5.6. SIMPLE Based Pressure-Velocity Coupling

The principal difficulty in solving the momentum equations for incompressible flows lies in the determination of the pressure. In the iterative SIMPLE-like [Semi-Implicit Method for Pressure-Linked Equations, Patankar and Spalding (1972)] algorithms, the discrete form of the continuity equation is converted into an equation for the pressure correction. The pressure corrections are then used to update the pressure and velocity fields so that the velocity components obtained from the solution of momentum equations satisfy the continuity equation.

For computation of incompressible and compressible flows, the Unsteady SIMPLE method can be extended by introducing density corrections and coupling them via an equation of state with the pressure corrections, see Karki and Patankar (1989) and Demirdzic at al., (1993).

3.5.7. Solution Procedure

For a computational domain with M control volumes, a system of $M \times N$ algebraic equations like equation (3.77) need to be solved for N dependent variables ϕ. The equations are non-linear and also coupled with more than one dependent variable features in each equation. Since the nonlinearity in the equations the iterative solution techniques are used.

There are two approaches: the coupled (simultaneous) and segregated (sequential). In the segregated approach, each equation for the considered variable is decoupled by treating other variables as known. This leads to a subset of M linear algebraic equations for each dependent variable. Having much smaller storage requirements, the segregated approach is adopted in the computations.

3.5.8. Segregated Approach

In this approach, the coefficients a_j and the source term S_ϕ are calculated by using variable values from the previous iteration or time step. The resulting sub-system of linearized algebraic equations can be arranged in a matrix form as:

$$A_\phi \phi = S_\phi \tag{3.83}$$

Where, A_ϕ is the $M \times M$ coefficient matrix and S_ϕ are vectors of the unknown variable ϕ and the source term, respectively. It is important to note that the matrix A_ϕ is sparse (there are $n_i + 1$ non-zero elements in each row, n_i is the number of the nearest neighbours, i.e. internal faces), asymmetric, except for the pressure correction equation for incompressible flows, and diagonally dominant (A number of iterative methods which retain the sparsity of the above matrix can be used.

Algebraic multigrid methods (AMG) are among the most efficient solvers of large sparse linear systems. The idea behind multigrid methods is that long wavelength errors on the fine level appear as short wavelength errors on coarser levels and therefore, can be effectively damped out by a relaxation scheme [Borzi (2000)].

3.5.9. Under-relaxation

After solving the linearized system (3.83), a change of variable values from the previous (outer) iteration (ϕ^{k-1}) to the next iteration (ϕ^{k}) is limited in order to ensure the convergence of the solution procedure. The limitation, i.e. under-relaxation is done implicitly, as proposed by Patankar (1980)

$$\phi^k = \phi^{k-1} + \alpha_\phi (\phi^{new} - \phi^{k-1}) \tag{3.84}$$

where ϕ^{new} is the solution of (3.83) and φ α is the under-relaxation factor with values between 0 and 1. The implicit implementation of the above relaxation formula leads to the modified algebraic equation (3.78). It retains the same form but, the central coefficient (a diagonal element of matrix A_ϕ) and the source term are redefined as:

$$a_P^* = \frac{a_P}{\alpha_\phi}, S_\phi^* = S_\phi + \frac{1-\alpha_\phi}{\alpha_\phi} a_P \phi_P^{k-1} \tag{3.85}$$

so that the modified equation:

$$a_P^* \phi_P = \sum_{j=1}^{n_i} a_j \phi_{Pj} + S_\phi^* \tag{3.86}$$

is solved by the linear equation solver. Optimum under-relaxation factors are problem dependent. The under-relaxation is applied to all equations except to the pressure correction equation.

3.5.10. Implementation of boundary conditions

The boundaries of a solution domain are either natural (walls and free surfaces) or artificial in the sense that they are truncated parts of the physical domain through which fluid may enter or leave. The latter comprise the *inlet*, *outlet* and *symmetry* planes. For these types of boundaries, the pressure is extrapolated from the inside of the solution domain. However, the static pressure can often be prescribed on either the inlet or outlet boundaries. In such situations, it is useful to introduce the *pressure boundary* type

Inlet Boundaries

The values of the velocity components and other dependent variables (with exception of the pressure) are prescribed at inlet boundaries. These values may be known from experiments.

Outlet Boundaries

Outlet boundary conditions are used at the domain boundaries through which the fluid leaves. A zero gradient condition along the line connecting the interior node P and the boundary node b is commonly used to calculate the outlet values.

Symmetry Boundaries

When the flow is bounded by a plane of symmetry, the velocity component normal to this plane is set equal to zero, yielding zero convective flux. In addition, the normal derivatives of all the remaining variables are set to zero which implies zero diffusion fluxes. When a symmetry boundary condition is used in the absence of a natural plane of symmetry, care should be taken in placing this boundary at a location where the above conditions apply.

Wall Boundaries

The walls are assumed smooth and impermeable. For real flows, the velocity of the fluid, which is in contact with the wall, is equal to the wall velocity. This is known as a no-slip condition. This condition is usually enforced by specifying the wall velocity components. Only diffusion fluxes at the wall need to be evaluated since the convective fluxes are zero.

The hybrid wall treatment is done in order to resolve the viscous sub-layer the details are given in ~~the~~ section 3.4.

Total Enthalpy – Temperature

When the Standard heat transfer wall function is used, the enthalpy (energy) near-wall treatment is done by defining the near-wall thermal conductivity κ_w

$$\kappa_w = \begin{cases} \kappa & if\ y_P^* > y_T^* \\ \frac{y_P^*}{U_P^*+Y}\frac{\mu C_p}{\sigma_T} & if\ y_P^* \geq y_T^* \end{cases} \tag{3.87}$$

Where equation (3.88) gives the viscous sub-layer resistance factor Y, and the thermal sub-layer thickness y_T^* is obtained from the intersection of the linear and logarithmic law for the temperature. Thus, y_T^* is obtained from equation (3.89).

$$Y = 9.24\left[\left(\frac{Pr}{\sigma_T}\right) - 1\right]\left[1 + 0.28\exp\left(-0.007\frac{Pr}{\sigma_T}\right)\right] \tag{3.88}$$

$$\frac{Pr}{\sigma_T}y_T^* = \frac{1}{\kappa}\ln(E_T y_T^*)\ \ , E_T\ \approx 9.8 \tag{3.89}$$

The thermal wall boundary conditions are: given temperature, external convection and/or radiation and thin walls

3.6. Conjugate Heat Transfer

It is possible to perform conjugate heat transfer calculations. Some parts of the calculation domain are assumed to be solids. Inside these regions (specified via selections) the enthalpy equation is the only equation to be solved.

The solid is specified with its own physical properties: density, thermal conductivity, and thermal heat capacity. Inside the solid region, all source terms and matrix coefficients from all equations but the enthalpy are reset to zero. For the enthalpy, only the diffusion coefficients and the rate of change terms are calculated.

The interface between the fluid and the solid is a set of internal faces which is considered as a wall from the fluid side. All wall treatment is therefore applied there. The wall temperature is computed from a heat flux balance between fluid and solid sides.

3.7. Parallelization with MPI

This section describes the basic principles and techniques used for parallel execution of the computations. It uses the concept of the single program multiple data (SPMD) paradigm. This means that a single copy of the executable program can operate on multiple data. In this process, each processor has its own physical memory (or a part of the total memory space) attached to it and processors cannot access local memory of other processors. Data can be exchanged among processors by explicit message passing. In our case, a program is the CFD solver and multiple data sub-domains. Messages are exchanged with the MPI library. An advantage of SPMD paradigm is that programs developed with it can be executed on both distributed and shared computers.

4. Single Jet Impingement

4.1. Hydrodynamics of the single jet

This chapter describes the investigation of the hydrodynamics of single jet impingement process and the quenching of heated surface through the single jet. When the single liquid jet impinges onto the horizontal surface several flow regions are to be observed. The flow region just beneath the jet is called stagnation region. Then, the jet acceleration region comes, after that wall jet region. Due to the viscous effect, the velocity retards in the downstream of the flow. As the velocity becomes smallest the liquid becomes thicker (respecting the mass conservation law) representing the phenomenon termed as hydraulic jump. It may strongly influence the cooling efficiency in the surface quenching through the liquid jet. Therefore, it is important to investigate the hydraulic jump.

Several studies found on the free surface impinging jet. The fundamental work by Watson (1964) is necessary to elucidate here. He used the boundary layer theory and proposed the analytical expression for the velocity fields of the different flow regions such as stagnation region, accelerated region (boundary layer region), deceleration flow region, and hydraulic jump.

Azuma and Hoshino (1984) did the experimental validation of the above analytical study. They used the laser-Doppler measurement to verify the expression for laminar boundary layer, similarity region, and liquid film thickness.

Stevens and Webb (1993) also verified the Watson's analytical model. They used the Laser-Doppler velocimetry (LDV) for measurement of the velocity profile. They compared the velocity profile, free surface velocity, and film thickness. They found that the maximum velocity in the layer was not at $r/d < 2.5$ of the free surface. However, an analytical model of Watson assumes the maximum velocity at $r/d \leq 2.5$. Therefore, the film flows attracted the many researchers for last few decades to envisage the phenomena in detail [Nakoryakov et al., (1978), Yu et al., (1994), Bohr et al., (1993), Pan et al., (1992), Zumbrunnen (1991) and Zumbrunnen et al., (1992)].

4.2. Model of hydrodynamics study

For the case study, experimental investigations of a hydraulic jump from Gradeck et al., (2006) are selected to simulate with AVL Fire code (AVL FIRE Manual, 2009).

The flow and geometric parameters are taken as follows. The jet velocities are 1.72 m/s and 1.46 m/s, plate velocities are 1.53 m/s and 2.04 m/s and nozzle to plate spacing is 50 mm.

Table 1 – Matrix of simulation for case study

	V_j (m/s)	V_P (m/s)	d_j (mm)	h_{simu} (mm)
Case 1	1.72	1.53	12.96	50
Case 2	1.46	2.04	12.96	50

Where, V_j = Jet velocity, V_P = Plate velocity, d_j = Jet diameter, h_{simu} = Plate to jet distance.

In Figure 14, the z-r-θ coordinate directions are given and the (0, 0, 0) of the coordinate system lies at the center of the plate. The x and y coordinates are determined as $r.cos(\theta)$ and $r.\ sin(\theta)$. The grid is generated according to the near wall resolution of the $z^+ \approx 1$, $r^+ \approx 30$ and l^+ ($l = r\times\theta$) ≈ 30 (Figure 14-15). Here, $z^+ = \frac{z\,u_\tau}{\nu}$, $r^+ = \frac{r\,u_\tau}{\nu}$ and $l^+ = \frac{l\,u_\tau}{\nu}$.

The decision for taking such near wall resolution is based on the fact that, the viscous sublayer exists at y+ value less than 5. Here, in this computation (Figure 14) y^+ is actually z^+ due to the coordinate system. After that, r^+ and l^+ is taken sufficiently higher than z^+ in order to reduce the number of cells.

The approximate value of u_τ is taken as 2% of the jet velocity [Versteeg and Malalasekera (1995)] for the calculations of z^+, r^+ and l^+ at the time of grid generation. However, after computation u_τ is calculated as $\sqrt{\tau_w/\rho}$.

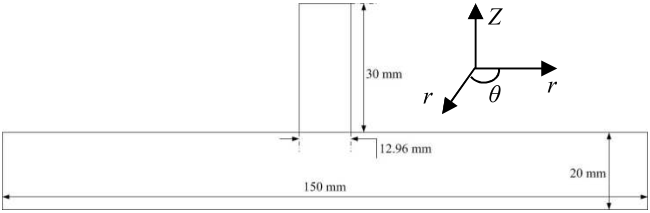

Figure 14 – Computational domain of the test case

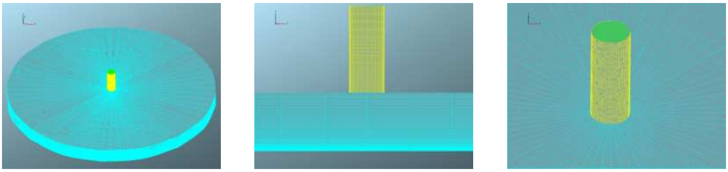

Figure 15 – The grid for the computational domain

In this computation, the *k-ε-ζ-f* turbulence model is used with hybrid wall treatment, which allows resolving the grid until viscous sublayer. This is also one of the reasons to take the z^+ value less than 5. The Figure 16 and 18 shows the free surface plot for the given test case. The horizontal axis is the location on the plate and the vertical axis is the iso-surface of the free surface of the water. The hydraulic jump is extracted from the Figure 16 and 18. The position of z_{max} is extracted in terms of the x, y coordinate (Figure 17 and 19) and compared against the experiment [Gradeck et al., (2006)]. The better agreement of simulation than previously published results [Gradeck et al., (2006)], shows that adequacy of the four-equation turbulent model (*k-ε-ζ-f*) used for the present research.

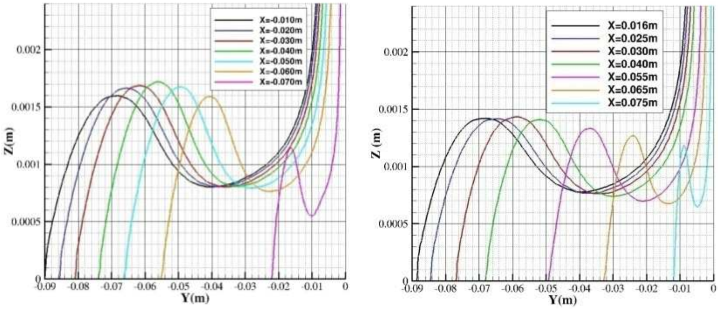

Figure 16 – The iso-surface of the water (V_j =1.72 m/s and V_p =1.53 m/s)

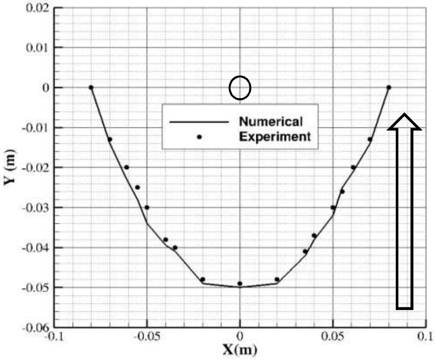

Figure 17 – Simulated positions of hydraulic jump compared with experiment [Gradeck et al., (2006)] (V_j =1.72 m/s and V_p =1.53 m/s, the arrow shows the direction of plate movement)

Numerical results show that the hydraulic jump positions move towards the jet impingement region only when the velocity of the plate is in opposite direction of the wall-jet velocity, otherwise, move away from the jet impingement region. Locus of the hydraulic jump at the surface has less radius of curvature for the high surface velocity. The hydraulic jump exists at the edge of the hydraulic radius exhibits a significant effect on the jet interactions.

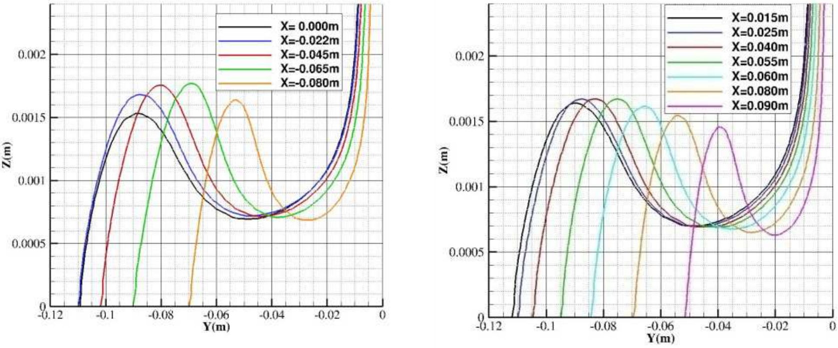

Figure 18 – The iso-surface of the water (V_j =1.46 m/s and V_p =2.04 m/s)

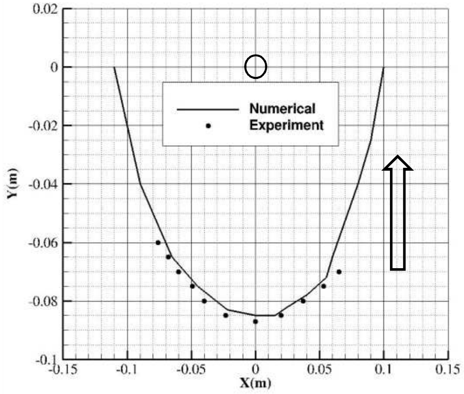

Figure 19 – Simulated positions of hydraulic jump compared with experiment [Gradeck et al., (2006)] (V_j =1.46 m/s and V_p =2.04 m/s, the arrow shows the direction of plate movement)

4.3. Decision of turbulence model for quenching simulation

It is paramount importance to check the turbulence model to use them in quenching phenomena. It is evidence from the research [Basara and Jakirlic (2003)] that the $k - \varepsilon$ model with standard wall function is not appropriate for the stagnation region flow and flow with separation. This model over predicts the turbulent kinetic energy at the stagnation region and hence over predicted the heat transfer rate.

Therefore, $k - \varepsilon - \zeta - f$ is used for the case of convection heat transfer and is validated the model from the literature [Stevens and Webb (1991)].

In order to validate the turbulence model mentioned above, the case is taken from the literature [Stevens and Webb (1991)]. The computational domain (Figure 20) for this case is as follows: Nozzle radius (r_n) = 2 mm, plate radius (R) = 24 mm, nozzle exit to plane spacing (h) = 15 mm, jet Reynolds number $Re_j = \rho U_j d/\mu$= 10600 and heat flux at the wall (Q) (=149000 W/m²)

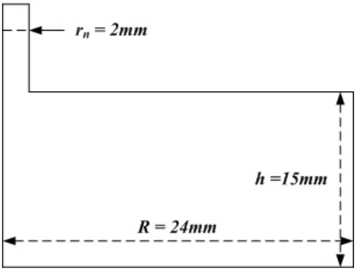

Figure 20 – Computational domain of test case for the heat transfer validation

The normalized pressure draws at the stagnation region flow of the liquid jet impingement in Figure 21. The line shows the calculation with new turbulence model, whereas the red circle shows the reference paper [Tong (2003)] calculation. It indicates that the span of stagnation region in the circular jet is around 1.25 times the diameter of the jet. Nevertheless, in the case of the multiphase flow at the stagnation region; it is general intuition from the flow phenomena that the span of the stagnation region would vary. In the case of the boiling at a high temperature of the surface, the transient nature of the boiling would influence the span of the stagnation region.

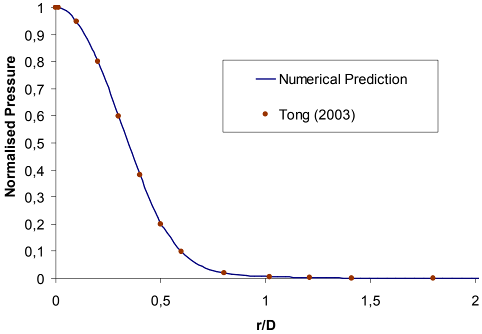

Figure 21 – Normalized pressure plot at stagnation region of the flow

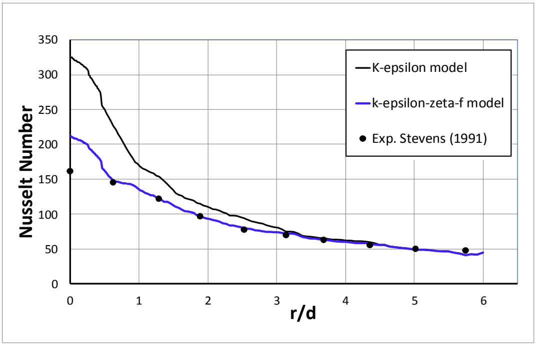

Figure 22 – Nusselt number plot for different turbulence model

In Figure 22, the Nusselt number plot given in the radial location of the flow the $k-\varepsilon$ turbulence model over predicted the heat flux at the stagnation region, the reason may lie on this fact that the turbulence kinetic energy prediction is higher at the stagnation region. The $k-\varepsilon-\zeta-f$ model shows improvement in the predictability. Other researchers also documented the better predictability of four-equation model. These results are for the single-phase liquid circular jet impingement on to the plate. In accordance with the experimental case, this simulation assumes constant surface heat flux.

It is observed from the current simulation that four-equation turbulence model ($k-\varepsilon-\zeta-f$) predicts the local heat flux at the stagnation region better as compared to the k-ε model.

Hence, it is decided that, $k-\varepsilon-\zeta-f$ turbulence model will be used for computation of quenching through single jet and hydrodynamics of the multiple jets impingement onto flat surface.

4.4. Description of flow configuration

The flow configuration considered accordingly to the subject of the experimental investigations at the Chair of Technical Thermodynamics, Technische Universität Darmstadt, Germany, and the present work represents an appropriate complementary study. The schematic flow geometry (computational domain) with the corresponding coordinate system (the azimuthal direction denoted by θ) shown in Figure 23. A circular water jet discharging from a nozzle whose diameter is 0.003 m impinges perpendicularly

onto a heated steel (SS304: Stainless Steel – Grade 304) surface. Nozzle to wall distance is 0.0975 m in the experiment. In order to avoid a very time-consuming free jet computation (free-surface flow), only part of this distance (h=0.045m) was covered computationally assuming the uniform jet velocity profile, Figure 22. Cylindrical surface diameter is D = 0.050 m and thickness (t) = 0.020 m. Here, considered a conjugate heat transfer model and accounted both fluid and solid (red-marked zone in Figure 23) regions. The fluid region considered as a multiphase system consisting of water, vapor, and ambient air. The ambient air considered as a low-temperature vapor. Three-dimensional calculations of water jet impingement on heated plate at jet velocity range
V_j =2.5-10 m/s, wall superheat range ΔT_{sat}=800 K-700 K and water sub-cooling range ΔT_{sub}=75 K have been performed.

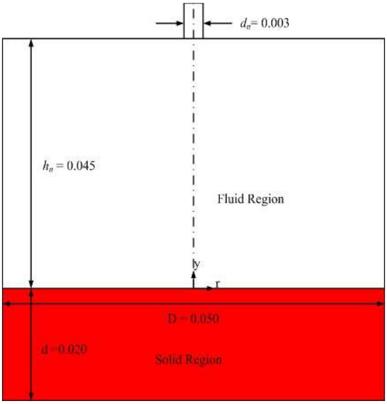

Figure 23 – Schematic of the computational domain in vertical r-y plane

4.5. Solution procedure and computational details

All computations were performed with the code AVL-FIRE (AVL List GmbH Company, Graz, Austria) employing the finite volume discretization method, which rests on the integral form of the general conservation law applied to the polyhedral control volumes [AVL FIRE Manual, (2009)]. The three-dimensional solution domain comprising both fluid and solid regions (Figure 24) has the shape of the cylinder, whose only one half with the symmetry boundary condition imposed at its plane was considered. In the fluid region, the number of grid cells are approximately 0.36 million ($N_r \times N_y \times N_\theta = 100 \times 150 \times 24$) and in solid region 0.24 million ($N_r \times N_y \times N_\theta = 100 \times 100 \times 24$). The near-wall computational mesh was carefully designed, the grid cells in the immediate vicinity of the wall are at the distance 10 µm; this is the result of the carefully conducted grid-independence study. Three different grid resolutions investigated and found that the water layer at the surface does not capture well for a grid comprising 69000 cells. Both finer grids consisting of 0.36 million cells and 0.86 million cells exhibited equal water layer thickness at the surface. Therefore, the grid comprising 0.36 million cells adopted for all cases of computations (The details are given in Annexure). The hexahedral grid cells are used everywhere thanks to appropriate block mapping of the solution domain. In such a way, the grid skewness alleviated largely. The fulfillment of the CFL number requirement (to be < 1 in the entire solution domain in the fluid region) led to the minimum time step of 10 µs.

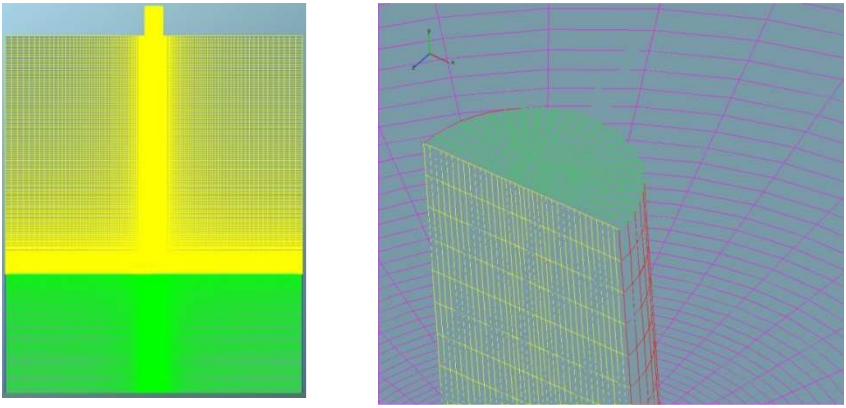

Figure 24 – Grid for the fluid and solid region

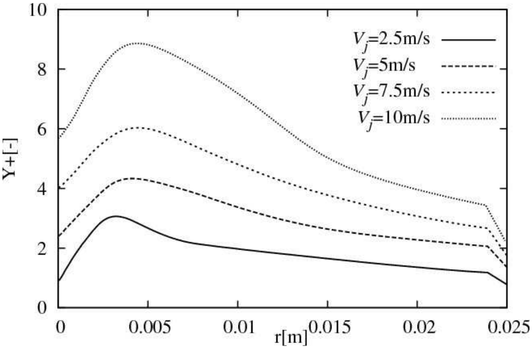

Figure 25 – y+ values of the wall-closest computational nodes for different jet velocities

The transport equations are discretized using the linear upwind scheme. Pressure and velocity are coupled through the well-known SIMPLE algorithm.

For the calculation of the y+ value before the computation for generating the grid, u_{wall} is taken as 2-5% of the free jet velocity as suggested by ERCOFTAC (2000) guidelines. The y^{+} value obtained at the first grid from the wall for the different jet velocities (Figure 25) revealed some flow features. For the jet velocities of 2.5-5 m/s the grid resolves the viscous sub-layer (hydro-dynamically), and for the higher jet velocities (7.5 m/s and 10 m/s the first grid cell at the vicinity of the surface are positioned somewhere in the transition-layer. Due to multiphase flow at the stagnation region, the flow velocity is higher for the jet velocities 7.5 and 10 m/s,

Separate computational domains constructed for the solid part (green part in Figure 23) and the liquid domain are numerically coupled at the interface of the solid-liquid boundary using the AVL-Code-Coupling-Interface (ACCI) feature. The advanced ACCI procedure allows the information about the phase change rates in the liquid domain to appear as cooling rates on the solid boundaries. Furthermore, one notes also the same grid resolutions in the radial and azimuthal direction: $N_r \times N_\theta$ (fluid) = 100×24 vs. $N_r \times N_\theta$ (solid) = 100×24. The advantage of the AVL-Code-Connectivity feature is used here to enable a smooth variable exchange.

4.6. Boundary Conditions

The following boundary conditions have been employed (see Figure 24 to follow the coordinate directions better):

- Wall boundary conditions, $r=0\text{-}R,\ y=0$ for all θ

  No-slip boundary $\mathbf{V}_{k,j}=0$; $T(r,\ t)$ prescribed

- Far-field boundaries, $r=d/2\text{-}R,\ y=h$

Atmospheric pressure prescribed

$$\frac{\partial \rho_{k,i}}{\partial y} = \frac{\partial \vec{V}_{k,i}}{\partial y} = \frac{\partial \varepsilon_{k,i}}{\partial y} = 0$$

Far-field boundaries, $r=R,\ 0<y<h$

Atmospheric pressure prescribed

$$\frac{\partial \rho_{k,i}}{\partial r} = \frac{\partial \vec{V}_{k,i}}{\partial r} = \frac{\partial \varepsilon_{k,i}}{\partial r} = 0$$

Inlet boundary (jet), $r=0\text{-}d/2,\ y=h$

$\vec{V}_{k,i} = -\vec{V}_{axial}$ (prescribed)

Symmetry boundary, *r=0, 0<y <h*

$$\frac{\partial P_{k,i}}{\partial r} = \frac{\partial \rho_{k,i}}{\partial r} = \frac{\partial \vec{V}_{k,i}}{\partial r} = \frac{\partial \varepsilon_{k,i}}{\partial r} = \frac{\partial T_{k,i}}{\partial r} = \frac{\partial f}{\partial r} = 0$$

The computations have been performed taking initially the uniform temperature of the steel block being of cylindrical shape. The upper flat surface is the impinging surface. The side-curved wall and the bottom surface of the solid part kept as adiabatic.

4.7. Results and Discussions

The understanding of the quenching through the liquid jet is enhanced through the computational study. Since the initial temperature of the solid block is high, the vapour generation is quite high. Hence, the vapour formation at the immediate vicinity of the wall is computed and analysed through the corresponding boundary layer development with respect to time and radial positions on the solid surface. After this, the influence of the turbulent kinetic energy on the boundary layer and heat transfer rate is analysed. The boiling curves are analysed at different jet velocities. The heat flux and surface temperatures are compared with experimental investigations for different velocities with respect to time. Furthermore, the boiling front propagations are analysed computationally and compared with experimental investigations.

4.7.1. Study of boundary layer at the quenching surface

Numerical investigations of the quenching of heated flat surface revealed many essential physics of flow. It is imperative to know the flow behavior at the surface before going into details of the surface quenching.

The hydrodynamic study of quenching surface is vital from two aspects. First, it provides valuable information to develop the quenching model and another it provides supplementary data to perform the experimental investigations.

The boundary layer profiles at radial location R = 1.5 mm (radial location from the center of the circular surface) of the flow are obtained (Figure 26) at three different times (2.0s, 2.5s, and 3.0s). These times are computed from as the jet impinged on the surface and started boiling.

After the jet impinged on the heated surface, the liquid starts boiling, and at 2s of the boiling (solid line in Figure 25), a linear velocity gradient at the vicinity of the wall is obtained, which implies the presence of vapor at the immediate vicinity of the heated surface.

The linear variation of the flow velocity (positive velocity gradient) exhibits the presence of viscous sub-layer, whose depth is approximately 400 µm (0.0004 m) given as Y (m) (distance in the perpendicular direction of the quenching surface) in Figure 26.
After 2.5s (dot-dot (....)) of the boiling, the velocity gradient near the surface is higher as compared to at 2.0s. Higher gradient shows that the vapor layer is very thin (Approx. 80-100 µm). Such a high-velocity gradient enables the vapor to escape from quenching surface. At 3.0s (dash-dot-dash (-.-)) the velocity gradient is same as of 2.5s. However, the vapor layer thickness is a little bit increased from 80-100 µm to approx. 120-140 µm.
Linear behavior of the vapor layer in the immediate vicinity of the quenching surface is documented for all jet exit velocity at 900 ^{o}C of surface temperature.
Above the vapor layer which shows viscous sub-layer, a transition and turbulent layer exists. This layer is formed by the mixture of liquid and vapor exhibits high turbulent kinetic energy of the flow due to the bubble vortex formation [Yaminsky, (2006)]. As the bubble vortex formation intensifies the circulation of the flow, consequently, increases the frequency of the hydrodynamic instabilities. As a result, the rate of heat transfer should be increased significantly [Ruspini et al., (2014)].

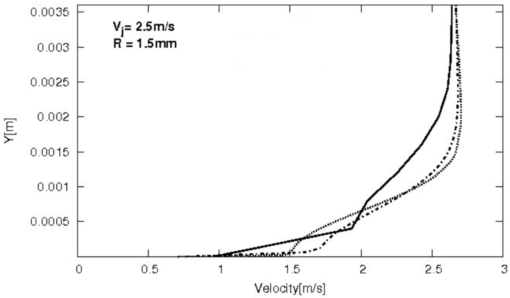

Figure 26 – Velocity profile at R= 1.5 mm at different time solid line (−) 2.0s , dot-dot (....) 2.5s, dash-dot-dash(-.-) 3.0s

However, the presence of vapor just beneath the mixed phase acts as a barrier in the way of increase in the heat transfer rate.

Figure 26 depicts the progression of the flow at the surface; it is clear that first the vapor layer flows to downstream and then mixed with the liquid and forms the mixed phase. The vapor phase shows the low-velocity gradient at 2.0s and higher velocity gradient at 2.5s and 3.0s. The velocity gradient at the layer of mixed phase exhibits the transition layer.

In Figure 26, the velocity profile is obtained at R = 3 mm (radial location from the centre of the circular surface) for three different times such as 3.0 s, 3.5 s, and 4.0 s. This particular radial location (R = 3 mm) is important from the perspective of coming under the jet acceleration region. The linear variation of the velocity profile at the immediate vicinity of the surface signifies the presence of the vapor layer comes under viscous sub-layer. The depth of the viscous sub-layer is around 500 µm. The positive velocity gradient shows the velocity is increasing in sub-layer. After the vapor layer, a mixed layer comes, which have a significant amount of liquid with vapor, which affected the velocity gradient and negative gradient comes into the picture. After this layer, a full liquid layer comes and shows nearly zero velocity gradient.

For instance, considering the velocity profile at 3.5 s and 4.0 s (Figure 27), one can infer that, as the vapor escapes from the surface, vapor layer becomes very thin and exhibits higher velocity gradient as compared to at 3.0s of the boiling. The mixed layer has more significant amount of liquid as compared to the mixed phase at 3.0s and shows negative velocity gradient; then liquid layer shows nearly zero velocity gradient. In the mixed phase layer, the negative velocity gradient indicates that the vapor escapes from the surface through all possible directions. However, very few amount of vapor escapes through normal direction from the surface. This is why the mixed phase has more amount of liquid and shows the strong negative velocity gradient. On the other hand, liquid tries to penetrate the mixed phase layer and vapor layer to have contact with the quenching surface.

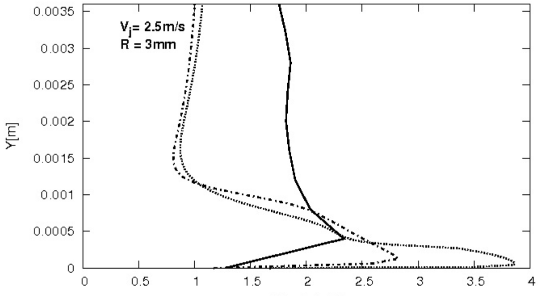

Figure 27 – Velocity profile at R= 3 mm at different time solid line (−) 3.0s , dot-dot (....) 3.5s, dash-dot-dash(-.-) 4.0s

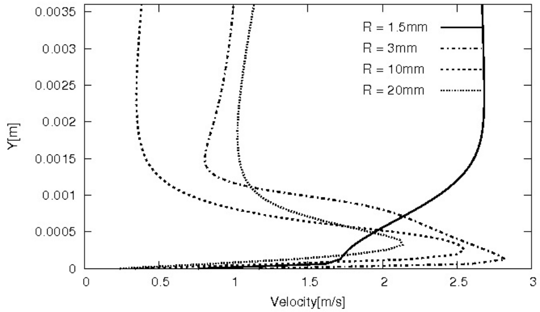

Figure 28 – Velocity profile after 12s for jet velocity 5 m/s (Re_{jet} = 14,800)

Furthermore, the boundary layers are investigated for jet velocity 5 m/s (Re_{jet} = 14,800) at time 12s (Figure 28) from the start of boiling at the heated surface.

At R = 1.5 mm, the velocity gradient is positive until the vapor layer (approx. 100 µm) (0.0001 m) in Figure 28. After this layer, mixed phase (mixture of vapor and liquid) layer comes, and velocity gradient is still positive but exhibits the lower gradient as compared to complete vapor phase. In the vapor phase, higher velocity gradient shows the higher turbulent shear- stress, as the turbulent normal stress is very less as ***v'*** is very less.

At R = 3, 10 and 20 mm, the velocity gradient is positive until 400 µm (0.0004 m given as Y(m)). After the vapor layer, the mixed phase (Vapour and liquid) comes, it exhibits the negative velocity gradient. Negative velocity gradient exhibits the dissipative nature of the turbulence in the mixed phase flow, because of the low inertia of the liquid, which is mixed with vapor in the mixed phase. This behavior of the velocity gradient exists until approx. 150 µm. After this layer, the velocity gradient is nearly zero indicates the presence of liquid layer until 3.5 mm.

Hence, one can classify the three layers, at the quenched surface, the first layer is complete vapor at the vicinity of the surface, and then mixed phase made up of vapor and liquid and at last completely liquid layer. All the layers show different nature of the velocity gradient as explained above. Since the present computational results exhibit the presence of viscous sub-layer of the boundary layer for the range of surface temperature 600-900 ^{o}C and the given range of jet velocity (2.5-10 m/s). However, it is necessary to discuss a theoretical model [Timm et al., (2003)] is assumed non-existent of the viscous sub-layer in the boundary layer. However, on the contrary, the computational results exhibit the viscous sub-layer.

In addition, there are three different types of the layer (vapour, mixed and liquid layer), such as positive velocity gradient exhibited by vapour layer, then the negative velocity gradient exhibited by mixed layer and finally zero velocity gradient exhibited by liquid layer, whereas in Timm's analysis only positive and zero gradient of velocity exist.

Therefore, Timm's model over predicted the heat-flux from experiment [Omar et al., (2009)].

The variation of vapor velocity at the vicinity of surface and behavior of mixed (Vapor-liquid phase) flow, which is above the vapor layer, with respect to time and positions at the surface can be modeled through Kolmogorov-Sinai-entropy theory [Frigg, (2004)].

4.7.2. Study of turbulent kinetic energy (TKE) at the quenching surface

The turbulent kinetic energy computed little bit away from the jet stagnation region and the behavior of TKE investigated inside the boiling front (Figure 29). Boiling front is defined as the outer periphery of the radial flow over flat surface through the liquid jet, which has significant bubble formation during the quenching.

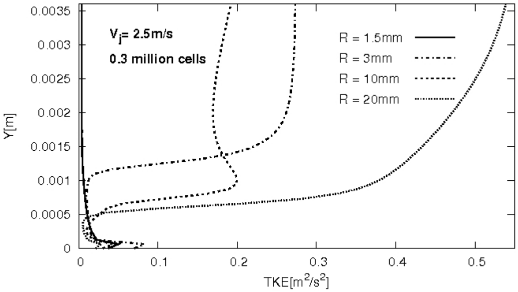

Figure 29 – Turbulent kinetic energy near the surface at VOF =0.1 (inside the boiling front)

As shown in Figure 29, at all radial positions, TKE increases (∂k/∂y is positive) until normal distance approx. 100 µm from the quenching surface. After that TKE decreases (∂k/∂y is negative) until normal distance approx. 120 µm.

After, 120 µm of perpendicular distance, at radial distance R = 1.5 mm, TKE is constant (∂k/∂y is nearly zero) until normal distance approx. 3500 µm, which is the entire thickness of different layers (vapor, mixed and liquid layers).

At radial distance R = 3 mm, TKE is constant (∂k/∂y is nearly zero) until the normal distance from 120 µm to 1000 µm, then it increases (∂k/∂y is positive) until normal distance approx. 2000 µm. Then finally, it is constant (∂k/∂y is nearly zero) until normal distance approx. 3500 µm.

At radial distance R = 10 mm and 20 mm, TKE is constant ($\partial k/\partial y$ is nearly zero) from 120 µm to 500 µm. Then, finally, it increases ($\partial k/\partial y$ is positive) non-linearly. Nevertheless, the non-linearity demonstrates dynamic nature of multiphase flow system.

For the jet velocity 5 m/s (Figure 30), $\partial k/\partial y$ is positive and attributes high gradient as compared to jet velocity 2.5 m/s (Figure 30) until the normal distance 100 µm from the quenching surface. Then, $\partial k/\partial y$ exhibits negative until 100 to 120 µm. Finally, $\partial k/\partial y$ varies non-linearly. Moreover, the non-linear variation does not follow the same behavior as for jet velocity 2.5 m/s (Figure 29). The non-linear variation of TKE shows that the phenomenon increases the entropy of the system. Therefore, the turbulent behavior near wall introduced another parameter to define the entropy of the system. Non-linear nature is because of the complex interaction among the multiphase system. The details of the TKE at different locations of the surface shown in the annexure, useful for those who want to define the entropy of the system to quantify the chaos.

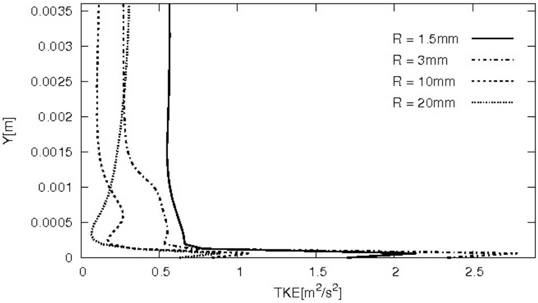

Figure 30 – Turbulent kinetic energy near the surface at VOF =0.1 (inside the boiling front) for jet velocity 5 m/s (Re_{jet} = 14,800)

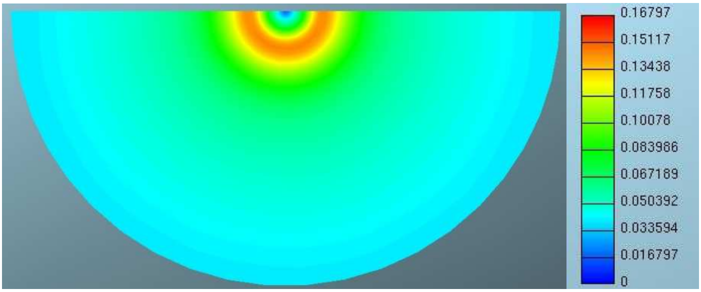

Figure 31 – Contours of Turbulent Kinetic energy at the surface for 2.5 m/s jet velocity at 5s at the middle of nucleate boiling

The above Figure 31 depicts the contours of turbulent kinetic energy (TKE) at the surface. The minimum TKE is at the stagnation region, and it increases up to the jet acceleration region ($r \approx$ 3-4.11 mm) as contour shows (Figure 31).
Another Figure 32 depicts the velocity vector at the stagnation region and the acceleration region.

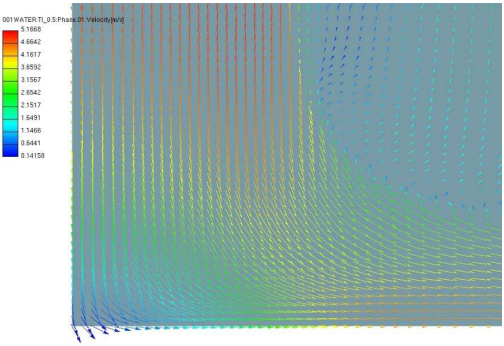

Figure 32 – Velocity vector at the stagnation and acceleration region for jet velocity 5m/s at 10s at the middle of nucleate boiling

The velocity at the stagnation region is not zero. Because due to the thermal inertia of the heated surface. However, it attains minimum velocity, and the velocity increases until the jet acceleration region. These two regions are primary interest to enhance the understanding of the flow boiling at high temperature.

The boundary layer profile at different radial position (Annexure) depicts that viscous sub-layer and the buffer layer are highly unstable, induced by the non-equilibrium and chaotic boiling. The average velocity at the first grid cell (10 µm) at the radial position (R = 1.5 mm), which is also the location of jet acceleration region is around 0.7 m/s. Which shows that single phase boiling does not commence at this region but governed by multiphase boiling. Consequently, shows the higher shear stress in this region compared with stagnation region of the flow. At the radial position 3 mm, the wall shear stress is highest, and at 10 mm of the radial location which is again, low wall shear stress.

The dynamic nature of the boundary layer shows that we should remodel the wall function including the instability. Here, in this research hybrid wall-function used successfully, which takes care of viscous sub-layer. Furthermore, the reason for taking hybrid wall function will be explained later. Furthermore, as the flow moves away from the jet stagnation region. The little bit less chaos commenced at the level of the boundary layer.

4.7.3. Study of quenching at the surface

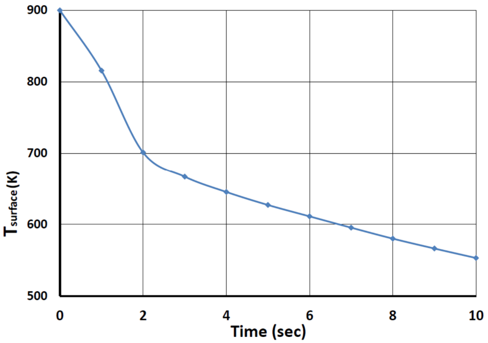

Figure 33 – Cooling at Stagnation region for jet velocity 2.5m/s

Now, the quenching curve at the stagnation region (Figure 33) exhibits fast cooling at the initial time until 2 sec and slow cooling after this stage. It shows that initially the liquid subcooling ($\Delta T_{sub} = T_{sat} - T_l$) is more and is capable of removing more heat flux per unit time. As the time passes, the liquid gets more heat-flux and forms thin vapor layer at the vicinity of the surface, but the escape of vapor from the stagnation region is much hard. Therefore, the slow cooling occurs. The cooling curves for other locations of the surface are given in Appendix.

Now, the boiling characteristics are investigated. The boiling curve for jet velocity 2.5 m/s has been plotted in Figure 34 (*a*-*b*) at different locations of the surface. It exhibits the mode of heat transfer mechanism at the heated surface. The nucleate and transition boiling are responsible for the heat transfer. The nucleate boiling occurs in the wide range of the wall temperature, while transition boiling occurs in the narrow range of the wall temperature. The transition boiling occurs in a wider range of wall temperature for the flow at wall jet region, which is far from the acceleration region.

The maximum heat flux is tabulated for 2.5 m/s jet velocity in Table 2. At *R*=0 mm (corresponds to stagnation region of flow) has maximum heat flux 9.81 MW/m^2 at wall-superheat of 1077 K. As one moves away from stagnation region of the jet flow, at *R*=1.00 mm the maximum heat flux value 7.41 MW/m^2 achieved at approximately 944 K. This is the minimum value of wall superheat value. From *R* = 3 mm to *R* = 20 mm the wall superheat increases as the maximum heat flux decreases. This is (3< R< 20 mm) the region of wall jet flow. The overall maximum heat flux of the surface has been achieved at R = 0 mm.

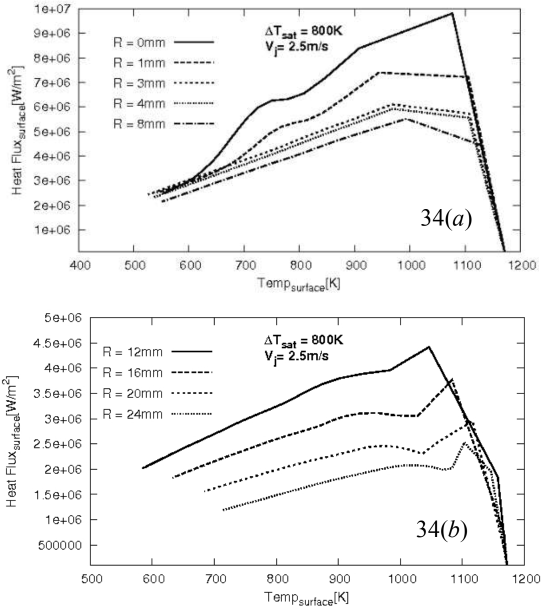

Figure 34 (a-b) – Boiling curve for V_j = 2.5 m/s at different location of the surface

Table 2 – Maximum Heat Flux at different location of the surface for $V_j = 2.5$ m/s

Location on flat surface (mm)	*Maximum Heat Flux Value (MW/m^2)*	*Wall-Superheat (K)*
0	9.81	1077
1	7.41	944
3	6.10	967
4	5.92	969
8	5.52	994
12	4.42	1046
16	3.76	1083
20	2.95	1116

The boiling curve for jet velocity 5 m/s has been plotted in Figure 35. The boiling curves obtained at the wall jet region. As one can see, the transition and nucleate boiling is predominant and the range of temperature to commence the transition boiling is wide.
The maximum heat flux at different locations on the wall superheat has been tabulated in Table 3. At $R = 0$ mm, the maximum heat flux of 8.32 M/W^2 at 951 K of wall superheat. Until R =3.00 mm the maximum heat flux value goes down. The wall superheat at R = 1.00 mm increases to 1121 K and again at R =3.00 mm, wall superheat is at 975 K. This oscillation of the wall superheat shows the complex behavior of the flow.

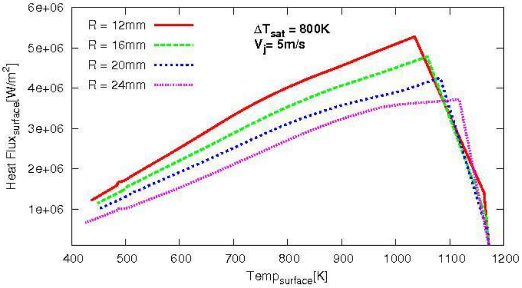

Figure 35 – Boiling curve for $V_j = 5$ m/s at different location of the surface

Table 3 – Maximum Heat Flux at different location of the surface for $V_j = 5$ m/s

Location on flat surface (mm)	*Maximum Heat Flux Value* (*MW/m²*)	*Wall-Superheat (K)*
0	8.32	951
1	7.23	1121
3	6.91	975
4	7.13	968
8	6.07	1002
12	5.27	1035
16	4.78	1058
20	4.25	1082
24	3.72	1117

At R = 4 mm, the maximum heat flux get the value 7.13 MW/m^2 at 968 K wall superheat. Now, from R = 4 mm to 24 mm, the maximum wall heat flux goes down, and wall superheat increases.

The boiling curve for jet velocity 7.5 m/s has been plotted in Figure 36. On the other hand, for jet velocity 7.5 m/s, again the range of temperature to occur the transition boiling at the wall jet region becomes narrow as compared to the jet velocity 2.5 m/s and 5 m/s. It indicates the influence of the jet velocity on the transition boiling.

The maximum heat flux has been tabulated in Table 4. At R = 0.00 mm the maximum heat flux 8.77 MW/m^2 has been attained at 1086 K of wall superheat. At R = 1.00 mm the decrement of the maximum heat flux 7.49 MW/m^2 and wall superheat 1099 K has been registered. At R = 2.00 mm to 4.10 mm wall heat flux increases. From R = 4.10 mm to 20.00 mm the wall heat flux decreases.

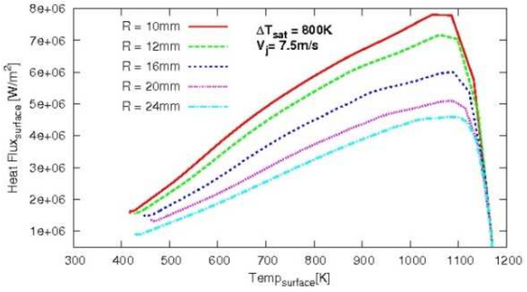

Figure 36 – Boiling curve for V_j = 7.5 m/s at different location of the surface

Table 4 – Maximum Heat Flux at different location of the surface for V_j = 7.5m/s

Location on flat surface (mm)	*Maximum Heat Flux Value (MW/m^2)*	*Wall-Superheat (K)*
0.00	8.77	1086
1.00	7.49	1099
2.00	7.98	1061
3.02	9.09	1038
4.10	9.46	1068
10.00	7.81	1046
12.00	7.17	1060
16.00	6.01	1089
20.00	5.10	1087

The boiling curve for jet velocity 10 m/s has been plotted in Figure 37. From this result, is conferring that, increasing the jet velocity, the range of temperature to commence the transition boiling is decreasing.

The maximum heat flux has been tabulated in Table 5. At R = 0 mm the maximum heat flux 8.54 MW/m^2 has been attained at 1078 K of wall superheat. From r = 0 mm to 4.10 mm the increment of the maximum heat flux 11.74 MW/m^2. Furthermore, from r = 4.11 mm to 20.00 mm wall heat flux decreases.

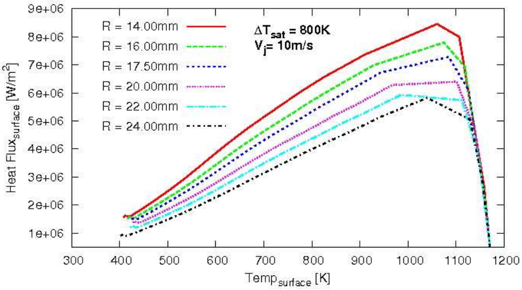

Figure 37 – Boiling curve for V_j = 10 m/s at different location of the surface

Table 5 – Maximum Heat Flux at different location of the surface for V_j = 10 m/s

Location on flat surface (mm)	*Maximum Heat Flux Value (MW/m^2)*	*Wall-Superheat (K)*
0.00	8.54	1078
1.04	8.96	1074
2.03	10.81	1045
3.02	11.74	1021
4.11	11.73	1006
10.34	9.58	1035
12.33	8.99	1048
16.00	7.78	1074
20.00	6.39	1101

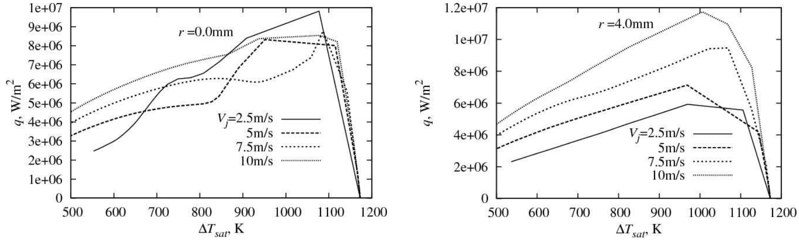

Figure 38 (a-b) – Boiling curves for different jet velocities (Left: plotted at stagnation region (r =0 mm) Right: plotted at acceleration region (r = 4 mm))

The effect of the flow velocity can be seen in the boiling curve in Figure 38 (*a*-*b*). As the velocity of the jet increases, the heated surface liberates more amount of heat flux.

The influence of the jet velocity on the boiling curve shows the heat transfer mechanism at the heated surface. Transition boiling and nucleate boiling play a pivotal role for the heat-flux extraction mechanism. In this simulation, sub-cooling of the liquid is 75 K and the jet Reynolds number varies from (7400 to 30000 approx.). The published experimental results [Islam et al (2008)] shows that for liquid sub-cooling more than 55 K and high velocity of the jet, the formation of the stable vapor layer at the immediate vicinity of the heated surface are not possible. Rather than the explosive pattern has been seen just after the impact of the liquid jet until few millisecond of the flow. Due to the transient boiling characteristic, the heat flux for jet velocity 2.5 m/s at r = 0 mm is 9.81 MW/m^2 for the wall superheat 1077 K. While for higher velocity of the jet at 5, 7.5 and 10 m/s the heat flux are 8.32, 8.77 and 8.54 MW/m^2 and wall superheat are 951 K, 1086 K and 1078 K respectively. This can be explained by the residence time of the liquid at stagnation region and corresponding boiling behavior. For the low velocity of the jet, for the certain control volume of the liquid which passes through the stagnation region of the flow will stay longer and takes heat flux from the surface and formation of a large number of vapor bubbles and heat transfer mechanism at boiling may lead to higher heat flux. On the other hand, for higher velocity, the residence time for the same control volume of the liquid will decrease and corresponding heat transfer mechanism may lead to different thermal diffusivity. It is still hard to say which is more dominant the residence time of the liquid control volume or the formation of a bubble at certain wall superheat. Furthermore, this hypothesis can be validated through the high precision experiment.

As the flow move away from the location r = 0 mm, for the jet velocity 2.5 m/s, the maximum heat flux goes down and the corresponding wall superheat increases as shown in Table 2. This can be explained by again with a residence time of the certain liquid control volume. Due to the higher residence time of moving control volume, the liquid temperature will attain the saturation temperature in less time. Therefore, the liquid is not capable of extracting higher heat flux than heat flux at r = 0 mm. At this velocity of the jet, the boiling heat transfer is more pronounced by the sub-cooling of the liquid.

For the jet velocity 5 m/s, the decrement of the heat flux has been registered from r = 0 mm to 3.00 mm, at r= 4 mm the heat flux again get little bit higher value approximately 7.13 MW/m^2. From r = 4.00 mm to 24.00 mm, the heat flux decreases. At this velocity of the jet, the effect of the flow velocity on the heat flux has been seen. It can be said that the stagnation region span around r = 0 to 3.00 mm and the jet acceleration region from 3.00 mm to 4.00 mm. At the jet acceleration region, the thermal diffusivity gets higher value, capable of extracting the higher heat flux value than the heat flux at r = 1.00 mm and 3.00 mm. However, still the heat flux at R = 0 mm is higher than the value at $r = 4.00$ mm. It can be said that residence time of the liquid control volume at the stagnation region is higher than at the acceleration region. Therefore, the boiling at stagnation region may lead to higher heat flux. The effect of different flow regime on boiling heat transfer has been seen here for 5 m/s velocity of the jet. It has been expected that for higher jet velocity the effect of flow regime will be more pronounced than the boiling heat transfer.

For the jet velocity 7.5 m/s, the maximum heat flux value decreases from $r = 0$ mm to 3.02 mm. At $r = 4.10$ mm the heat flux has the highest value of 9.46 MW/m^2, is higher than the value of heat flux at $r = 0$ mm, which is 8.77 MW/m^2. Now, the effect of the residence time of the control volume of the liquid is less dominant than the effect of acceleration region on the heat transfer. For the jet velocity 10 m/s, the maximum heat flux value at $r = 0$ mm is 8.54 MW/m^2 and it increases until $r = 3.02$ mm to the value of 11.74 MW/m^2. From $r = 4.11$ mm to 20.00 mm the heat flux decreases. This is due to the effect of high velocity, which induced more chaotic and turbulent behavior of the bubble dynamics at the surface. Consequently, until jet acceleration region of the flow, the higher heat flux has been achieved.

Another possible explanation can be for higher heat flux at jet velocity 2.5 m/s at the stagnation point, due to the shifting of the Leidenfrost temperature towards higher wall superheat for higher jet velocity. But, again the explanation of this behaviour can be envisage through the experiment. It is clear that, for the jet velocity at 5 m/s or higher. The effect of different flow regime on the boiling heat transfer has been seen.

At the wall-jet acceleration region (at $r=4$ mm, $y=0$) the boiling curve has been obtained for different jet velocities. The maximum heat flux has been observed at higher jet velocity values at the position $r=4$ mm. It is explained by the fact that at a higher jet velocity more thermal diffusivity will take place at the jet-acceleration region.

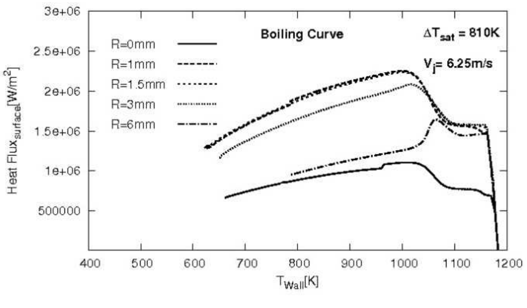

Figure 39 – Boiling curve for jet velocity 6.25 m/s and initial surface temperature 910 °C and ΔT_{sub} =10 K

In the boiling curve, the shoulder of heat flux is not found for the sub-cooling 75 K. The Figure 39 and 40, shows that shoulder of heat flux for sub-cooling 45 K and 10 K. This result also shows that sub-cooling effect on the surface quenching is more. Since, in Figure 40, the jet velocity is 6.25 m/s and sub-cooling is 10 K, have nearly the same maximum heat flux as for jet velocity 2.5 m/s and sub-cooling 45 K. But, the heat-transfer mechanism is different. The same influence is found with the experiment in literature [Gradeck, et al., (2009)].

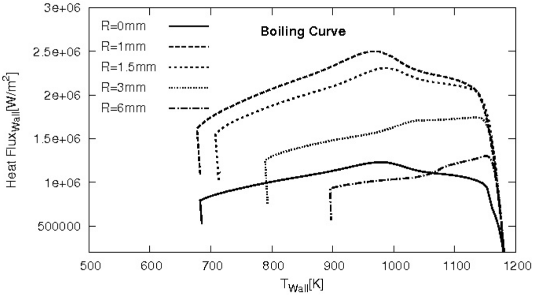

Figure 40 – Boiling curve for jet velocity 2.5 m/s and initial surface temperature 910 ° C and $\Delta T_{sub} = 45$ K

Lowering the wall-superheat one can obtain the ‘shoulder of heat-flux’, even for lower jet Reynolds number (see details in Appendix).

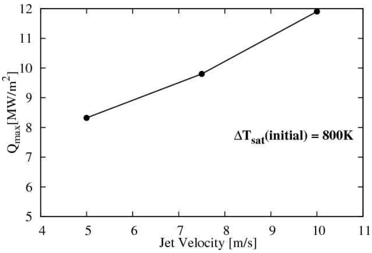

Figure 41 – Plot of maximum heat with respect to jet velocity

The overall maximum heat flux has been plotted against the jet velocity in Figure 41. It has been found that the overall maximum heat flux is a linear function of the jet velocity. However, the behaviour is not same at the velocity of jet 2.5 m/s. Which has been explained with a different mechanism. Therefore, one need to define the critical velocity of the jet where the effect of inertia is more pronounced, with respect to different initial surface temperature, sub-cooling and material thermal properties in detail for jet impingement configuration.

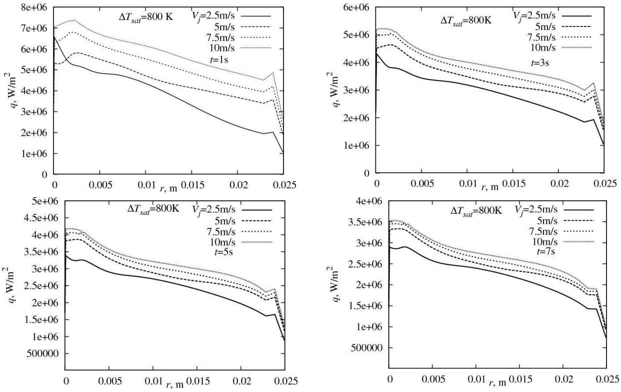

Figure 42 – Heat-flux development in terms of different jet velocities at t =1s (upper left), 3s (upper right), 5s (lower left), 7s (lower right)

Figure 42 displays the wall heat flux evolution (corresponding to the time instance *1*s to *7s*) along the radial direction in terms of the jet velocity. The heat transfer intensification is obvious. As the jet velocity is increased, the maximum heat flux occurs at higher wall super heat for both the stagnation and wall-jet acceleration regions.

The maximum wall heat flux is at the region $r \approx 3.00$ mm to 4.00 mm, the location corresponding to the jet acceleration region. The effect of the wall-jet acceleration region is more pronounce at the higher velocity and larger time instance. These results point out the fact that, for higher wall superheat at the initial time, the boiling phenomena is more pronounce at jet stagnation region where the bubble production rate is quite high. Herewith, a more intensive momentum and thermal diffusivity exchange hinder the wall-jet acceleration at the surface after the stagnation region accordingly, this phenomenon enhances the cooling rate at stagnation region for lower jet velocities. On the other hand, at times, e.g. 7.00 sec, the less number of bubbles are produced leading to a less vapor generated at the stagnation region. It causes a more intensive wall-jet acceleration and consequently an intensified momentum transport and thermal diffusivity leading finally to a substantial cooling rate enhancement.

The temporal evolution of the radial surface temperature distribution of the different jet velocities (2.5 m/s-10 m/s) is compared with the experimental findings in Figure 43 (*a-d*). The effect of the different flow regime on the temperature is clearly seen for all jet velocities. The qualitative behavior of the temperature at the stagnation region and the jet acceleration region is captured well with the experiment. For the higher jet velocities at 5m/s and more, the more quantitative agreement of the surface temperature can be seen.

The lowest temperature values (at r ≈ 4.00 mm) have been obtained at the larger jet velocity, the situation corresponding to the highest cooling efficiency. The temperature distribution in at 1.00 sec depicts the fact that at jet velocity 2.5 m/s the lowest temperature is at stagnation region, not at the wall-jet acceleration region. The possible mechanism is already explained in the boiling curve. For longer times the effect of wall-jet acceleration region (i.e., higher cooling efficiency) is more pronounced resulting in the lowest surface temperature.

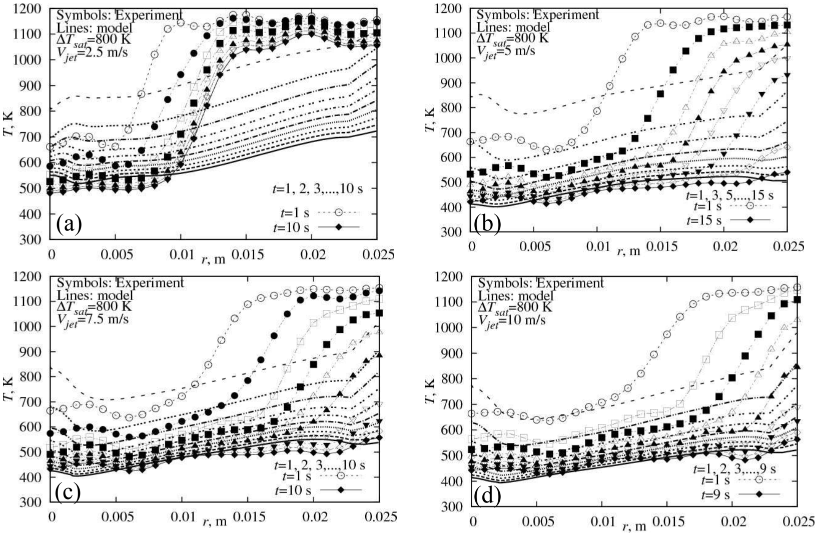

Figure 43 – Temporal temperature distribution on the surface at different locations for jet velocity: V_{jet} = 2.5 m/s (a), 5 m/s (b), 7.5 m/s (c), 10 m/s (d)

For the jet velocity 10 m/s, it can be seen that the temperatures have better agreement with the experiment for the initial time also. The surface temperature until r ≈12 mm shows good agreement with the experiment. Now, it can be said that the present quenching model computed the temperature of the surface gave better agreement with the experimental results for the higher jet velocity (Reynolds number > 30000). As in the industrial flow circuit for the quenching through the jet have a higher velocity (20000 < Reynolds number < 30000). Therefore, the present model can predict the surface temperature within the acceptable limit of the accuracy.

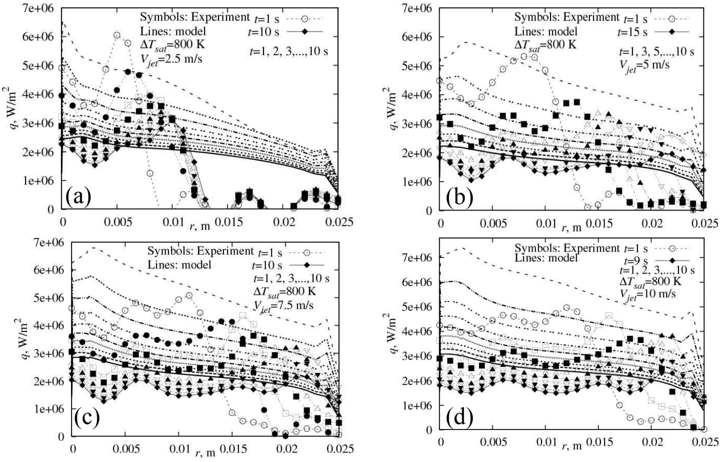

Figure 44 – Temporal heat-flux distribution on the surface at different locations for jet velocity: V_{jet} = 2.5 m/s (a), 5 m/s (b), 7.5 m/s(c), 10 m/s (d)

The computational heat-flux development along the flow on the surface plotted for the different velocities with the experiment in Figure 44 (*a-d*). The computational behavior is in accordance with the different flow regime. The jet acceleration region exhibited higher heat flux than the heat flux at other locations. The qualitative behavior at the higher jet velocity is not exhibited good agreement. However, it can be explained by the fact that the transient nature of the experiment. However, the surface average heat flux showed more agreement with the experiment. As observed in the experiment that the steep gradient of the temperature found at the transition regime from the wetted to the non-wetted region of boiling. This behavior is not included in the present quenching model. This may be a possible reason for the heat-flux behavior.

In order to include the effect of the wetted and non-wetted region in the present model, one needs to study the wetted and non-wetted region in depth.

Within the wetted region, the heat transfer rate is more intensive as compared to at the non-wetted region of the quenching surface. The experimental study reveals the wall-jet being lifted-up due to high-intensity evaporation. However, the computations simulated partially the transition from wetted to the non-wetted region under the present applied conditions.

Therefore, there are two ways to study this effect. The one relates primarily to the near-wall grid resolution another, to study the wetting-front propagation and compare with the experimental observation.

Therefore, an attempt has been made through the refinement of the grid (with $y^{+}\approx 0.05$ of the wall-adjacent node) for the capturing the steep temperature gradient in the wetted and non-wetted region of the boiling and comparison with an experiment in given in Fig. 45. However, this computation took the size of time-step 1.00 μs and computed for the jet velocity 2.5 m/s until 4.00 sec of the quenching time.

Although, the steep temperature gradient captured, but the oscillating temperature behavior at stagnation region evidenced the inadequacy of the hybrid wall function for such phenomena [Ramstorfer et al., (2005)]. Nevertheless, chaotic nature of the surface quenching also influenced such oscillations. However, it is important from the physics, which is revealed because of the refinement of the grid.

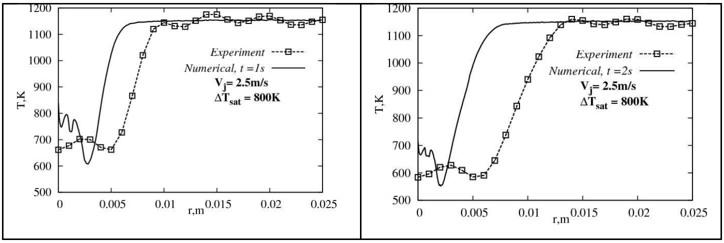

Figure 45 – Experimental and computational temperature evolution at refined grid (left: 1s, right: 2s)

The model has good temperature prediction through the averaging the heat flux for the quenching phenomena.

Nevertheless, the present model may be quite useful for the case of quenching through multiple jets as evident in most industrial applications. Where the temperature is the main parameter to control the material properties.

Now, the present model examined the other boiling characteristics, such as boiling-front-propagation. As the jet impinges on the plate, a transparent without boiling stagnation region has been seen, this is termed as a wetting region. Because this region is in direct contact with the liquid. As the liquid moves away from the stagnation region, the tiny bubble formation and other dynamics of the bubble have been visualized. This region termed as boiling region and the outer edge of this region is termed as boiling front.

Through experimental activity, the velocity of the boiling front has been investigated. Numerically, the boiling front is a little bit hard to describe, as simulating all bubble formed at the surface is computationally costly. Therefore, the volume fraction of liquid has been taken as a parameter representing the boiling front. Figure 46 is the contours of the volume fraction of liquid. Red part represented the wetting region of the flow and the other color represented the non-wetting region.

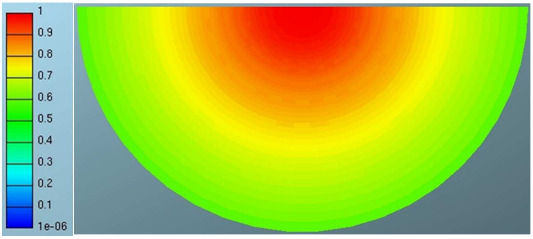

Figure 46 – Contours of volume fraction of water at the heated surface

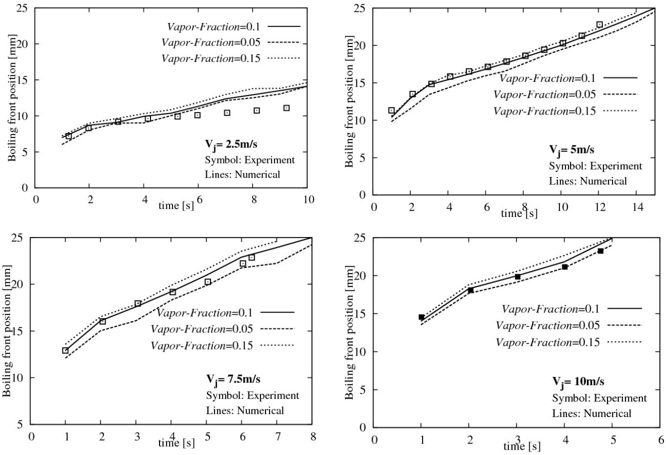

Figure 47 – Plot of boiling front threshold limit for jet velocities: V_{jet} = 2.5 m/s (upper left), 5 m/s (upper right), 7.5 m/s (lower left), 10 m/s (lower right)

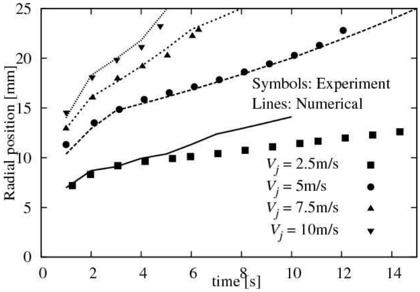

Figure 48 – Experimental and computational boiling front propagation for different jet velocities

Thus, it is important to decide the boiling-front in terms of the volume-fraction of vapor. The computationally obtained boiling-front threshold corresponds to the vapor volume fraction of 10% in the wall-next grid cell. One observes a good agreement with the experimental outcome. Further criteria for the boiling, i.e. wetting-front determination corresponding to 5% and 15% have been also checked as in Figure 47. The following plot suggests that the vapor volume-fraction corresponding to 0.1 may be the best choice for the wetting front position.

Now, the boiling-front propagation velocity has been plotted for different jet velocities. As Figure 48 displays the temporal evolution of the position of the wetting-front, i.e. boiling front propagating towards the edge of the heated plate.

Therefore, it has been seen that the present quenching model has strong ability to represent the flow-boiling feature.

The idea for improving the quenching model lie in improving the wall function with inclusion of the bubble dynamics and boiling-front propagation characteristics. The artificial roughness at the wall can be used as an analogy of the bubble dynamics. The inclusion of volume fraction as boiling-front propagation can be mimic by the progression of surface roughness with respect to boiling-front propagation velocity. These features can be included as input to the quenching model.

5. Multiple Jet Impingement

5.1. Introduction

In particular, steel processing industries employ multiple liquid jets to quench the heated surface in order to achieve the desirable product quality. In past two-three decades, the demand for the steel has been increased exponentially in the developing countries. Therefore, several new technologies have been emerged and resulted in the economic production of the desirable product quality. Present chapter envisages the methods to improve the cooling efficiency with more enhancement of the quality of final product and to meet the increasing demands in the future.

Increasing the cooling rate of the metal processing can produce the higher strength of steel with less alloying elements. Several technologies have been employed in order to increase the cooling rate in the ROT (Run-Out-Table) cooling process [Cho et al., (2008), Rivallin and Viannay (2001), Liu et al., (2002)]. One of the basic approaches are to increase the mass flow rate of the liquid jet, another approach is to decrease the distance between jet headers to the surface, the configuration of the header system like hexagon, pentagon, square and rectangular, and dimensions of the nozzle like square, rectangle, and circular shape of jet exit. One the other hand, the uniformity of the cooling is a prime factor in order to have better control on the microstructures and granular structures of the metal surface.

Therefore, one needs to study the nozzle configuration along with several flow parameters for the better design of the cooling header system.

The chapter is dedicated to the derivation of the theoretical model for the determination of the liquid pool height at the surface as well as the hydrodynamics of the multiple jets are studied numerically. The effect of the mass-flow rate, plate width and the turbulence produced due to the impingement are studied.

5.2. Theoretical model for the multiple jets impingement

Figure 49 shows the conventional flow domain. The x-y plane at the bottom (z = 0) is the heated surface. Normal to the x-y plane in the positive z-direction is the nozzle header, which consists of several nozzles (in the figure it shows few for reference). The figure also depicts the flow direction. The y-z plane at x= 0 is treated as the symmetry plane. Normal to the y-z plane in the positive x-direction is an outflow. The free stream flow velocity on the surface is u m/s in the x-direction and flow velocity in the y-direction is not taken into account. The flow rate q_{in} ($m^3/m^2.s$) comes from the top onto the horizontal surface. The liquid pool height (h) can be written by the following equation:

$$\frac{d}{dx}(hu) = q_{in}(x) \tag{5.1}$$

Integrating of the above equation for the entire length of the surface yields following equation:

$$hu = \int_0^x q_{in}(\xi)d\xi = Q \tag{5.2}$$

Here, the liquid pool velocity (u) and pool height (h) both are unknown, which can be determined in proceeding sections.

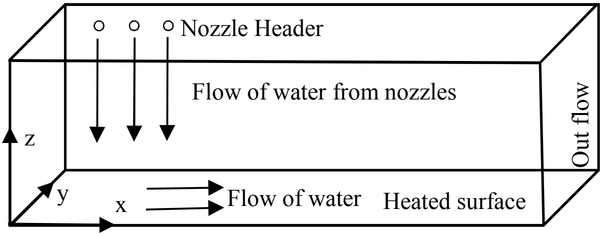

Figure 49 – Flow domain on the heated surface

5.2.1. Static Pressure and Pool Height

The pressure at the bottom h=0 varies with z and is denoted as $p_b(z)$. Similarly, the pressure at the top surface of the liquid pool is p_t. In terms of the hydrostatic head it can be given by the following relation:

$$p_b = p_t + \rho g h \tag{5.3}$$

The top surface of the liquid pool is at the atmospheric pressure, therefore, defined by the condition $p_t = 0$. Therefore, height and bottom pressure are related by:

$$h = \frac{p_b}{\rho g} \tag{5.4}$$

Bernoulli's equation is written for the streamline of the flow as follows:

$$p + \frac{1}{2}\rho u^2 = C \tag{5.5}$$

The plate center *x* = 0 is denoted by the index 0. It is a symmetry location and thus *u*(*x* = 0) = 0. Considering a streamline near the bottom *h* = 0. Inserting equation (5.4) leads to

$$h + \frac{1}{2g}u^2 = h_0 \tag{5.6}$$

Bernoulli's equation thus connects the heights at various points. The height at the center h_0 is unknown can be obtained from the height at the edge using the edge discharge condition.

5.2.2. Edge discharge condition

At $x = x_E$ the discharge (per unit length in plate withdrawal direction) is $h_E\, u_E = Q(x_E)$. This is usually expressed in terms of a Poleni factor (Naudascher, 1987) in the following way:

$$Q(x_E) = C_D g^{1/2} h_E^{3/2} \tag{5.7}$$

When C_D is given, the height at the discharge point can be computed from

$$h_E = C_D^{-2/3} Q^{2/3}(x_E) g^{-1/3} \tag{5.8}$$

and the velocity of the flow is given by this equation:

$$u_E = C_D^{2/3} Q^{1/3}(x_E) g^{1/3} \tag{5.9}$$

To retrieve the height h_0 at the center, equations (5.2) and (5.6) are combined and giving

$$Q^2 = 2gh^2(h_0 - h) \tag{5.10}$$

At every point on the surface:

$$h_0 = h + \frac{Q^2}{2gh^2} \tag{5.11}$$

Evaluating the right-hand side at $x = x_E$ and using equation (5.7) leads to from equation (5.6):

$$h_0 = h_E + \frac{Q_E^2}{2gh_E^2} \tag{5.12}$$

$$h_0 = C_D^{-\frac{2}{3}} Q(x_E)^{2/3} g^{-1/3} + \frac{Q_E^2}{2gC_D^{-\frac{4}{3}} Q(x_E)^{4/3} g^{-2/3}} \tag{5.13}$$

$$h_0 = \left(C_D^{-\frac{2}{3}} + \frac{C_D^{\frac{4}{3}}}{2} \right) Q(x_E)^{2/3} g^{-1/3} \tag{5.14}$$

$$h_0 = C_D' Q(x_E)^{\frac{2}{3}} g^{-\frac{1}{3}} \tag{5.15}$$

The value of the C_D depends upon the shape of the edge to discharge the liquid [Kraatz and Mahajan (1975)], in the equation (5.15) the value of C_D' can be determine by the following equation:

$$C_D' = \left(C_D^{-\frac{2}{3}} + \frac{C_D^{\frac{4}{3}}}{2} \right) \tag{5.16}$$

The characteristic of the C_D' has been plotted in Figure 50 with respect to the C_D tuned according to the experiment [Cho et al., (2008)].

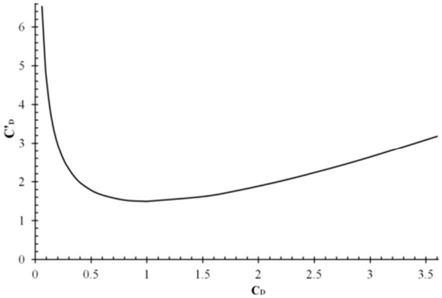

Figure 50 – Characteristic of the discharge coefficient

It is customary to define the flow velocity, liquid pool height, and mass-flow rate in terms of the non-dimensional form. Now, the flow velocity of the liquid on the plate and pool height can be non-dimensionalized in the following way:

$$U = \frac{u}{\sqrt{2gh_0}} \tag{5.17}$$

$$H = \frac{h}{h_0} \tag{5.18}$$

For non-dimensionalizing the lateral distance, *X= x/L*, where, *L* is the total length of the plate and mass flow rate in the lateral direction can be non-dimensionalized in the following way:

$$Q = \frac{Q(x)}{\sqrt{2gh_0^3}} \tag{5.19}$$

Apart from sections, where $q_{in} = 0$, this grows monotonically with x. Now, with the above parameters the equation (5.6) can be written in the following form

$$\frac{h}{h_0} + \frac{u^2}{2gh_0} = 1 \tag{5.20}$$

$$H + V^2 = 1 \tag{5.21}$$

$$V = \sqrt{1 - H} \tag{5.22}$$

and equation (7.2) becomes:

$$\frac{h}{h_0}\frac{u}{\sqrt{2gh_0}} = \frac{Q}{\sqrt{2gh_0^3}} \tag{5.23}$$

$$HV = Q \tag{5.24}$$

$$H\sqrt{1 - H} = Q \tag{5.25}$$

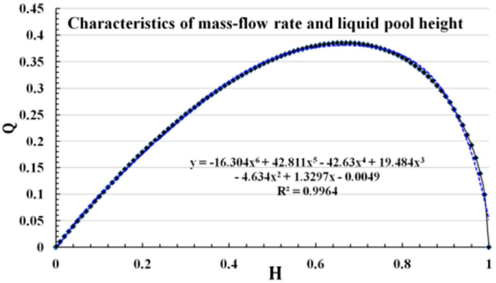

Figure 51 – Characteristics of liquid pool height with respect to the mass-flow rate

The flow characteristics with respect to the liquid pool height have been seen the Figure 51. It shows that the maximum value of the non-dimensional mass flow rate is 0.3849 for the non-dimensional height around 0.66. This implies that the water pool height has certain limitation and at a certain height, the flow rate becomes maximum.

In this equation, the effect of the cross-flow has been neglected, because of the infinite length of the cross-flow. To use this flow behavior the optimum flow rate and the height can be determined for the engineering applications.

The theoretical model for the determination of pool height and the average velocity of the pool has been compared with the computational model.

5.3. Problem description and procedure for solution

The computational domains for the multiple jets are shown in Figure 52 (*a*-*c*). The nozzle arrays arrangement exhibit the hexagonal pattern. The proceeding section discusses the reason for taking such configuration.

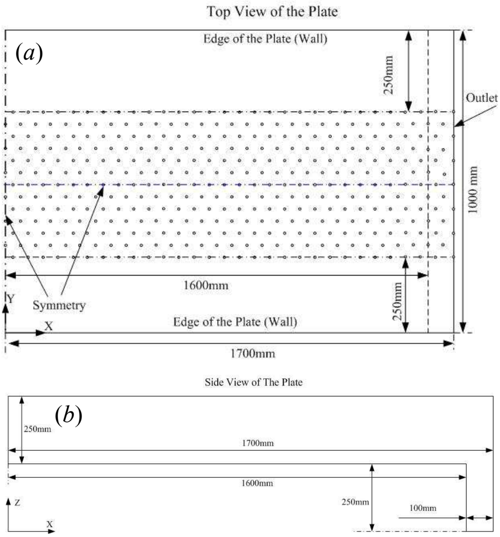

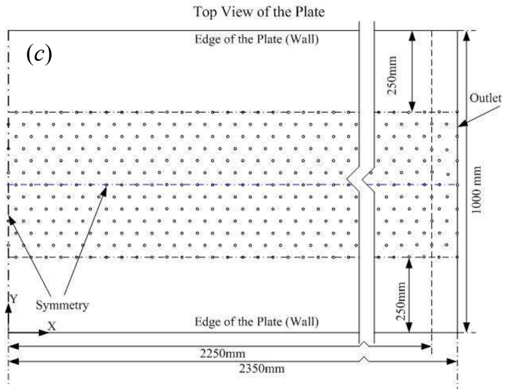

Figure 52 (a-c) – Computational geometry of the multiple jets flow

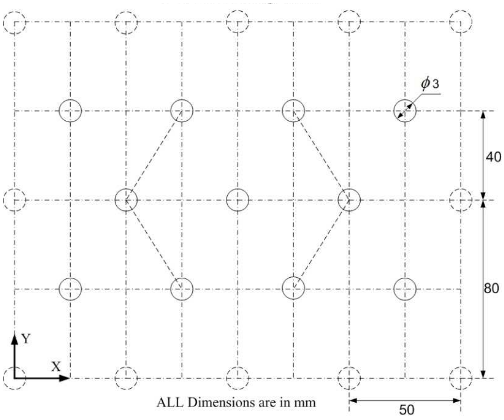

Figure 53 – Nozzle array configuration

Table 6 – Geometrical dimension and flow parameter

Case	Plate width (*m*)	Spray width (*m*)	Volumetric flow rate of water (m^3/h)	Nozzle velocity (*m/s*)
1	3.2	4.7	900	5.11

2	3.2	4.7	1500	8.53
3	4.5	4.7	900	5.11

The blue line (Figure 52 (a-c)) divides the computational domain into two parts and computes the lower quarter of the domain. Symmetry boundary condition applied along the plane of the central blue line. The nozzle spacing and diameter considered accordingly as shown in the following Figure 53.

The volume of Fluid (VOF) model is used to capture the water-air interface and the k-ε-ζ-*f* turbulence model has been used for these computations along with hybrid wall function.

All computations are performed with the CFD code AVL-FIRE (AVL List GmbH Company, Graz, Austria) employing the finite volume discretization method (Linear Upwind scheme), which rests on the integral form of the general conservation law applied to the polyhedral control volumes. Velocity-pressure is coupled through the SIMPLE-Algorithm (Patanker, 1980).

The fulfillment of the CFL number requirement (to be less than one in the entire solution domain) led to the minimum time step of 1e-04 sec and calculations have been performed until a steady state of the flow has been ensured. Thirty-two processors are used for this calculation and the number of the grid are 10 million takes 8-9 weeks per case.

The data regarding computations such as computational domain, the company Dillinger Hütte GTS provides jet arrays arrangement and mass flow rate of water.

5.4. Results and discussion

The hydrodynamics of the multiple jets are necessary to investigate in order to know the heat transfer characteristics during the quenching process. As the liquid jets impinge onto the large horizontal isothermal surface, the liquid accumulates before it comes out from the outlet. Consequently, the liquid layer started to build up to a certain height. The thickness of the liquid layer depends upon the mass flow rate and the width of the plate. Before, development of liquid pool, the jets interact with each other. There are different ways of jets interactions studied in order to develop the more understanding of the heat transfer mechanism. Development of the liquid pool emerges the hydrostatic pressure on the surface.

5.4.1. Jets arrays configuration

Jets arrays are one of the important parts of the several industrial flow circuits. These are used for heat and mass transfer for flat and curved surfaces, blocks, and aerodynamic stabilization of the strips. It has been seen that the staggered distribution of the nozzles exhibits maximum heat transfer rate as compared to any in-line distribution of the nozzles. Such a honeycomb-like nozzle array distributions as shown below (Figure 54) used for this study.

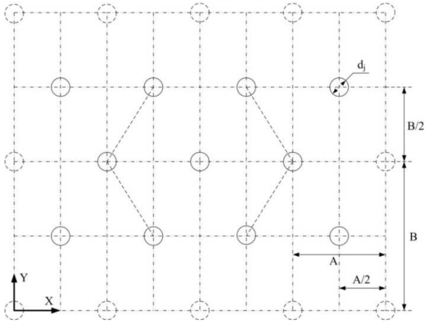

Figure 54 – Nozzle arrangement

When the jets impinge on the flat surface, after the stagnation region of the flow an acceleration region of high tangential velocity comes. This region can be enlarged by increasing the jet velocity (Mass flow rate) as given by Liu and Lienhard V (1993) and consequently, the heat transfer rate can be enhanced as shown in Figure 55. An acceleration region ends at the edge of hydraulic jump. In chapter five, the variation of the hydraulic jump position with respect to jet velocity and surface velocity are discussed.

Of course, the structure of the hydraulic jump depends upon the surface tension of the liquid [Liu and Lienhard V (1993)]. Which is less interest because here the focus is to enhance the turbulent flow at the surface, so that, one can get the enhanced heat transfer rate. The second parameter is the surface velocity. As seen in the fourth chapter, the direction of surface velocity is same as the flow, and then curvature radius will be more as compared to the opposite direction of the surface velocity and flow velocity. Apart from the jets arrays distribution, these two parameters namely surface velocity and jet velocity are important for the multiple jets interactions at the surface.

Now, the heat transfer rate (which can be expressed as Nusselt number) depends upon the several geometrical and flow parameters, such as ratio of A/d_j, B/d_j, H/d_j, u_{se}/u_f, u_{so}/u_f, Reynolds number of the jet, Re_j and the Prandtl number, Pr. The two correlations can be established for one surface [Equation (5.26-5.27)].

$$Nu_e = CRe_j^{x1}Pr^{x2}\left(A/d_j\right)^{x3}\left(B/d_j\right)^{x4}\left(H/d_j\right)^{x5}\left(u_{se}/u_f\right)^{x6} \tag{5.26}$$

$$Nu_o = CRe_j^{x1}Pr^{x2}\left(A/d_j\right)^{x3}\left(B/d_j\right)^{x4}\left(H/d_j\right)^{x5}\left(u_{so}/u_f\right)^{x6} \tag{5.27}$$

The parameters A and B are shown in Figure 54, H is the water pool height at the flat surface, d_j is the nozzle diameter, u_{se} is the surface velocity at the same direction as flow velocity, and u_{so} is the surface velocity in the opposite of the flow velocity. Nu_e is the Nusselt number for that region where the surface velocity and flow velocity have same direction. Nu_o is the Nusselt number for that region where the surface velocity and flow velocity have opposite direction.

The distribution of the normalized heat transfer coefficient at the jet stagnation region and jet interaction region shows higher heat transfer rate (Figure 55). More uniform heat flux can be produced, by the interaction of the jet at the zone of high tangential velocity which is acceleration zone commenced before the hydraulic jump.

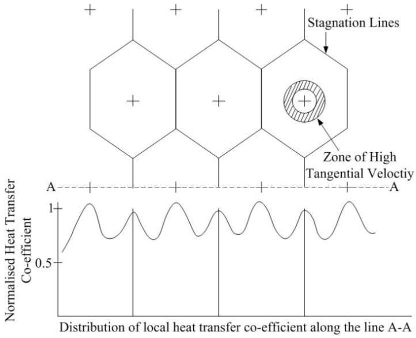

Figure 55 – Flow behavior and heat transfer characteristics

5.4.2. Jets Interactions

In the case of the multiple jets interactions, the production of the turbulent kinetic energy is higher than the single jet. When the jets interact before the occurrence of a hydraulic jump of the individual jet assist to produce more chaotic and turbulent behavior of the flow is evident by a high up wash of the jets as shown in Figure 56. When the jets interact after commencement of the hydraulic jump results in less chaotic and turbulent nature of the flow is obvious for the low jet velocity.

Since, the wall jet velocity is larger than the flow velocity at the hydraulic jump, as the jets interact before the hydraulic jump; the turbulence of the flow enhances the thermal diffusivity. Hence, responsible for the homogeneous heat transfer rate from the heated surface. The optimum arrangement of the multiple jets can ensure the interactions before the occurrence of a hydraulic jump for a wide range of jet velocity. Besides the geometric parameters, the flow parameters also influence the jet interactions such as jet velocity and surface velocity and pool flow velocity. Due to the surface velocity, the location of the hydraulic jump and jet acceleration region cannot remain symmetry with respect to stagnation region of the flow [Gradeck et al., (2006)]. One can control the jet interactions by keeping the constant jet velocity and varying the surface velocity and it's vice-versa. Furthermore, in order to increase the thermal diffusivity one can increase the jet velocity.

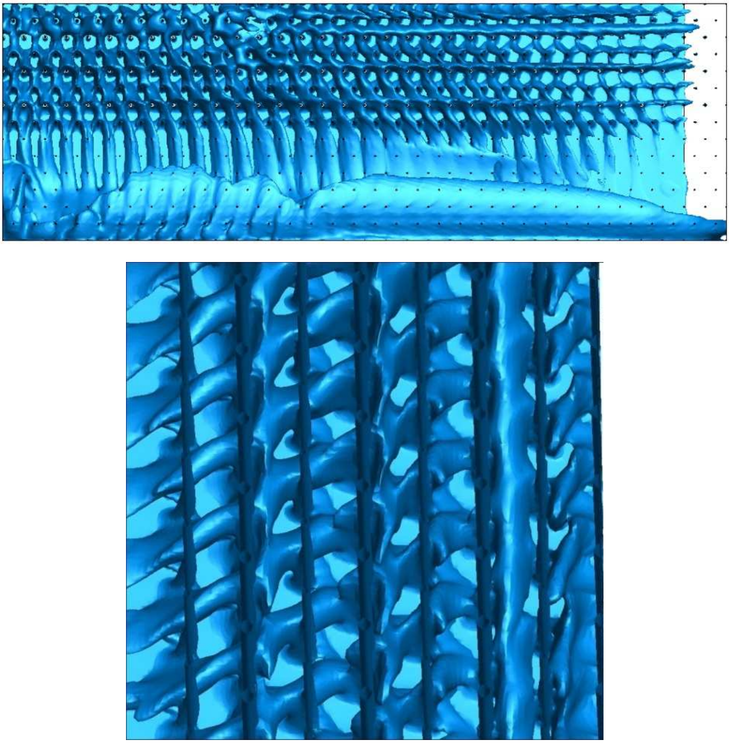

Figure 56 – Contour of iso-surface of water showing the jet interactions after 10 second

5.4.3. Static pressure distribution at the surface

The contours of the hydraulic pressure at the surface (Figure 57) depict the fact that high relative pressure is evident in both the stagnation region and the jet interaction region. It increases effective eddy diffusivity due to pressure redistribution. Consequently, high thermal diffusivity assists the high rate of heat flux. Also, it is evident from the results shown in Figure 57 that higher-pressure peaks can influence appropriately the heat flux; intensification of the flow rate by increasing the jet velocity can enhance the higher-pressure peaks and heat-flux. The hydraulic pressure is not a linear function of the flow rate, but it is proportional to the square of the flow rate. The Chong's [Chong et al., (2008)] experiment shows that after reaching a certain flow rate the hydraulic pressure and water pool height do not increase.

Furthermore, higher the water pool height absorbs more energy due to water jet impingement. Consequently, lower the value of the turbulent kinetic energy and heat-flux removal capacity. Therefore, it can be said that there is optimum water pool height and flow rate for the maximum heat flux removal capacity.

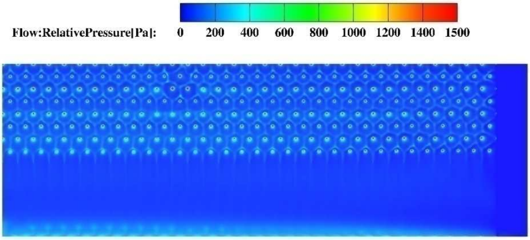

Figure 57 – Contour of relative pressure at the surface

5.4.4. Water pool height

The Figures 58, 59 and 60 depict the iso-surface of water. The iso-surfaces have been plotted by taking the water volume fraction 0.1. The grid cell comprises the volume fraction of water 0.1 regarded as the free surface.

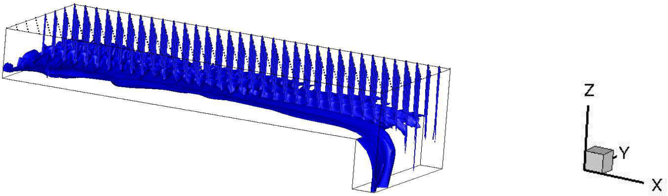

Figure 58 – Iso-surface of water for Case 1

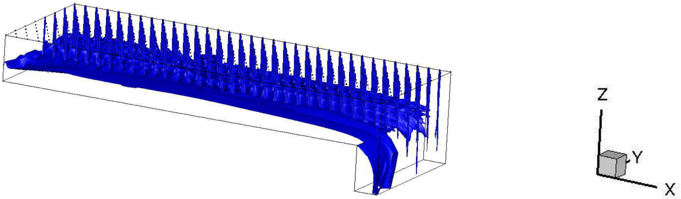

Figure 59 – Iso-surface of water for Case 2

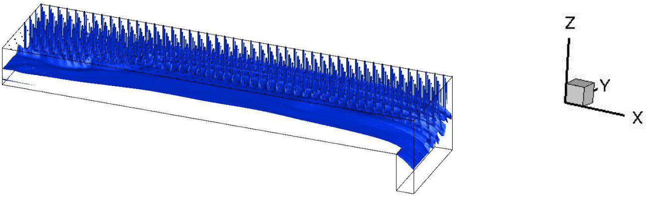

Figure 60 – Iso-surface of water for Case 3

In Figure 61 (*a*-*d*) and 62(*a*-*d*), results have been compared with the theoretical model developed for the pool height and the average velocity of the liquid. It shows in Figure 61 (*a*-*d*) that higher water pool height is evident by increasing the flow rate and the plate width. However, the higher water pool height can create more resistance to escape the vapor, which forms at the vicinity of the heated surface during quenching process. Study of the water pool height can help to develop the heat transfer model for the multiple jets. The effect of the pool height is included in the correlation suggested in equations (5.26) and (5.27).

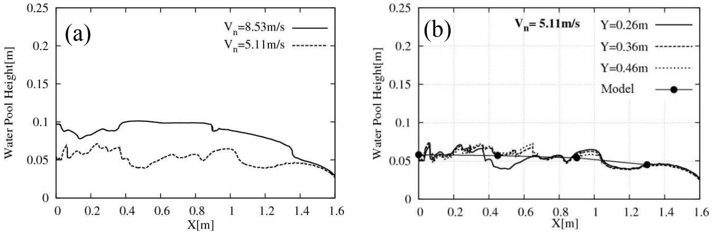

(c)

(d)

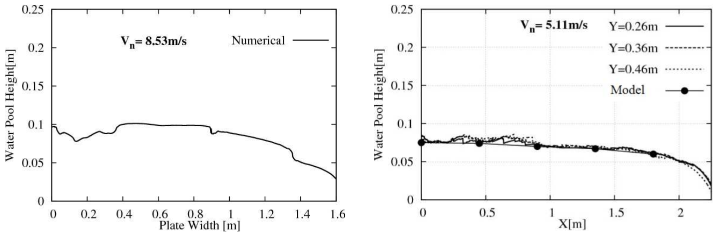

Figure 61 (a-d) – Water pool height at different velocity and different plate width

The wavy nature of the water-air interface advocates the relative pressure difference among stagnation region (underneath the nozzle impingement), wall-jet region, and the jet interaction region

5.4.5. Average velocity of the water pool

The plot of the average velocity profile (Figure 62(*a-d*)) for the different flow rate and different surface width gives a common fact that the velocity gradient near the edge is higher than the far from the edge of the plate. This can be able to drag the vapor until the edge of the plate and help the vapor to escape from the vicinity of the plate. Nevertheless, the driving force to pull out the vapor from middle to the edge of the surface will depend on the dynamic pressure developed by the formation of the vapor at the immediate vicinity of the surface should be higher than the hydraulic pressure at the edge of the surface. Then flow velocity of the water pool can easily drag the vapor from the middle to edge of the surface and higher the water pool velocity will create the higher drag force.

Now, we have learned that the water pool height in one hand can hinder the heat-flux removing capacity by damping the thermal diffusivity. Nevertheless, on the other hand, the higher average velocity of the flow and higher vapor formation permits us to higher drag force to escape the vapor from the edge of the plate. It has been realized that the second phenomena have a dominant effect on heat flux removal velocity for the high initial temperature of the surface. Because, at a high initial temperature of the surface, the vapor formation rate will be high and which supports the flow velocity of the water pool to drag the vapor from the middle of the surface to the edge. However, in the case of the lower initial surface temperature, both factors would be important for the heat-flux. In this research work, the focus is on the higher initial temperature of the surface.

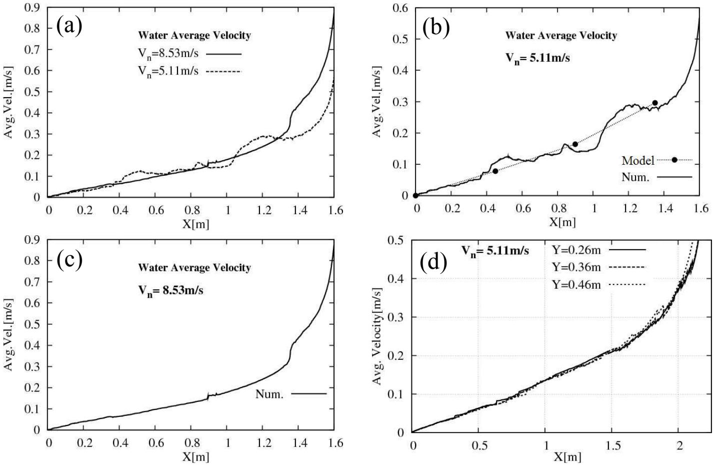

Figure 62 (a-d) – Average velocity of water pool height for different velocity and different plate width

5.5. Heat transfer model for the multiple jets

The analytical model for the quenching of the heated surface through multiple jets system is proposed. The effort is to develop the simplified model for the quenching through the jet impingement onto the flat surface with finite thickness. When the water impinges onto the horizontal plate at a high temperature, the water separates almost equal in the amount on both sides. On one side where the water flows in the direction of the flow and the other side, the water flows in the opposite direction of the plate velocity.

The two-dimensional heat conduction equations calculate temperature history within the plate.

$$\frac{\partial\theta}{\partial t} = \frac{\lambda}{C_{ps}\rho_s}\nabla^2\theta \tag{5.28}$$

Where θ is the temperature of the plate in (K), λ is the conductivity of the plate (W/m. K), C_{ps} is specific heat capacity of the plate (J/kg. K), ρ_s is the plate density in (kg/m^3). The discretization technique is finite difference scheme for above equations. The mesh size on the longitudinal and the plate thickness direction can be taken as h and k. From the hydrodynamic simulation of the multiple jets, the water pool height δ and the pool velocity V_i is known.

Assuming that the thickness of the water film is uniform in the thickness direction, the amount of the temperature rise *Δθ* of water in certain cell per incremental time

$$\Delta t_w = \frac{h}{V_i} \tag{5.29}$$

can be expressed by

$$\Delta\theta = \frac{\alpha_w(\theta_s - \theta_w)\Delta S.\Delta t_w}{C_{pw}\rho_w \Delta V} \tag{5.30}$$

θ_w is the temperature of water in the concerned cell (K)

θ_s is the temperature of the plate surface contacting with the water in the foregoing cell (K)

α_w is the heat transfer coefficient from the plate surface to the water film (W/m^2 K)

C_{pw} is the specific heat of water (J/kg. K)

ρ_w is the density of the cooling water (kg/m^3)

Where ΔS is the contact area of a cell between the water film and plate surface in m^2 and ΔV is the water volume in a cell in m^3. If the cell width of the water film is chosen at unity, we have

$$S = h.1 \text{ and } \Delta V = h.\delta.1$$

This corresponds to the amount of temperature rise of the water film, as the water film progresses from one cell to another cell. Let it now be assumed that the water temperature in the ith cell is θ_w. Thus, the water temperature in the (i+1)th cell reaches (θ_w+$\Delta\theta$) after the lapse of Δt_w. Here, it should be noted that Δt_w is taken to be equal to the period required to shift the water from a cell to the next cell.

In fact, the effect of the thickness of thermal boundary layer δ_t is introduced to the estimation of the temperature change in the cooling water. We now consider the effect of δ_t. The thickness of thermal boundary layer of a laminar flow parallel to a flat plate is commonly given by [Incropera and Dewitt, (1985)].

$$\frac{\delta_t}{x} = 4.87 Re_x^{-1/2} Pr^{-1/3} \tag{5.31}$$

Where, $Re_x = \frac{xV_i}{\nu}$, $Pr = \frac{C_p\mu}{\lambda_w}$

x is the distance measured from the leading edge corresponding to the impinging point

(m)

λ_w is the thermal conductivity of water (W/ (m.K))

μ is the dynamic viscosity of water (kg/(m.s))

ν is the kinematic viscosity of water (m^2/s)

When $\delta > \delta_t$, the temperature rises may be restricted to the thickness at in the water film cell. Let $\delta_{t,i}$ denote the thickness of the thermal boundary layer in the i-th cell. Again, it may be regarded that the temperature rise of the water element within $\delta_{t,i}$ is equivalent to $\Delta\theta$ and the temperature of the element being between $\delta_{t,i}$and δ is kept constant at θ_w on the condition that $\delta > \delta_t$. Thus, the heat balance between the nearest neighboring cells may be formulated as-

$$\theta_{w,i+1} = \frac{\theta_w(\delta_{t,i+1} - \delta_{t,i})}{\delta_{t,i+1}} + \frac{(\theta_{w.i} + \Delta\theta)\delta_{t,i}}{\delta_{t,i+1}} \tag{5.32}$$

Again, we consider the heat transfer coefficient in the wetting and non-wetting zones. We have given it in the form of-

$$\alpha_w = 0.063 \frac{\lambda_w}{x} Re_x^{4/5} Pr^{1/3} \tag{5.33}$$

Using the analytical model one can understand the quenching at different locations of the heated plate. However, the quenching model discussed in chapter four can be also used for prediction of the temperature.

6. Film Boiling Model at Stagnation Region

6.1. Introduction

In the case of the water jet impingement-quenching process, there is much likely a case of film boiling at the stagnation region. It is evident from the fact that, the surface temperature is usually in the range of 900-1100 °C and the water temperature ranges from 25 to 95 °C and the jet velocity ranges from 2 m/s to 10 m/s. It is experimental observation [Gradeck et al., 2006] that when the water temperature goes above 45 °C and jet velocity less than 5 m/s then the film boiling exists. In order to quantify the phenomenon, the jet stagnation region has been considered, because of the maximum heat flux removal capacity from this region. While a jet impacts upon the highly superheated surface, different boiling regime co-exists simultaneously with respect to space and time. It means that at given time for different locations, different boiling regime co-exists and at given a location for a different time there is the existence of the different boiling regime. The boiling regimes are nucleate, transition and film boiling. From transition to film boiling a minimum heat flux arises at a certain temperature, which is regarded as Leidenfrost temperature. At Leidenfrost temperature, the liquid cannot wet the heated surface and a vapor layer between the heated surface and the liquid layer exists termed as film boiling.

Before discussion of the modeling, it is vital importance to discuss the physics of the film boiling at the stagnation region. Due to the high temperature of the surface, vapor generates at a high rate, which can escape through parallel to the surface. In this way, vapor blanket forms at the vicinity of the surface, consequently, the film boiling establishes. Due to the high formation rate of the vapor near the surface, the momentum of the fluid increases and the gravity force due to liquid jet also comes into play; consequently, Rayleigh-Taylor instability establishes in spite of the low jet velocity influences the thermal buoyancy on the film. Therefore, high-frequency oscillation of the liquid-vapor interface enhances the momentum and thermal diffusivity. The flow features come under turbulent in multiphase flow at stagnation region.

In the case of multiphase flow at the stagnation region, there exists the vortex-flow studied by Sakakibara, et al., (1997). Therefore, the turbulent thermal diffusivity determines the heat flux and the temperature at the Leidenfrost point. However, the previous model [Karwa et al., (2011)] does not include the effect of turbulence and reported 46% less wall heat flux and 70% less wall-superheat. The present model considers the turbulence has better agreement with the published experimental results. Especially, the present model provides quite good results for high jet velocity and a high degree of subcooling.

6.2. Theoretical Study

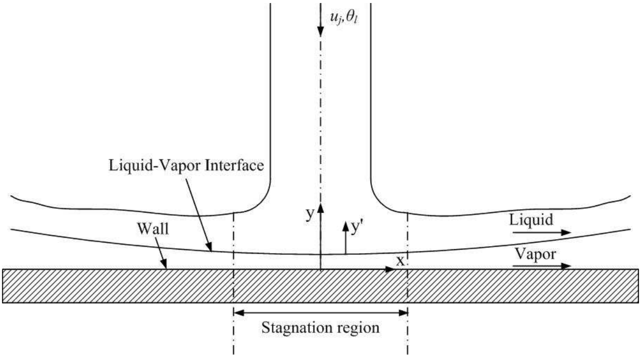

Figure 63 – Film boiling at jet stagnation region

Assumptions for the development of the model are as follows:

1. Flow is assumed at steady state.
2. At the stagnation region, due to multiphase flow and dynamic nature of film boiling the flow attributed turbulent nature.
3. The shear stress at the liquid-vapor interface is zero and the thickness of the velocity boundary layer in the liquid is equal to zero. Therefore, the liquid velocity at the liquid- vapor interface is equal to the free stream velocity.

6.2.1. Model for the Planer Jet

In this section, the flow and energy equation for the planar jet is developed. It anticipates that the stagnation region lies underneath the planar jet of liquid with vapor layer in the immediate vicinity of the surface as in Figure 63. Figure 64 illustrates the streamlines at the stagnation region due to the turbulent multiphase flow the streamlines curvature are more as compared to the laminar case.

The jet stagnation region spans about 1.3 times the jet width in case of vapor layer existing between the heated surface and the liquid layer. The dynamic behavior of the interface enhances the momentum of the flow. Consequently, pressure distribution in the stagnation region anticipates fourth-order polynomial equation:

$$\frac{P}{0.5\rho_l u_j^2} = \left(\frac{x}{1.3w}\right)^2 \left\{\left(\frac{x}{1.3w}\right)^2 - 2\right\} + 1 \tag{6.1}$$

The normalized pressure distribution plotted along the flow direction and given in Figure 65.

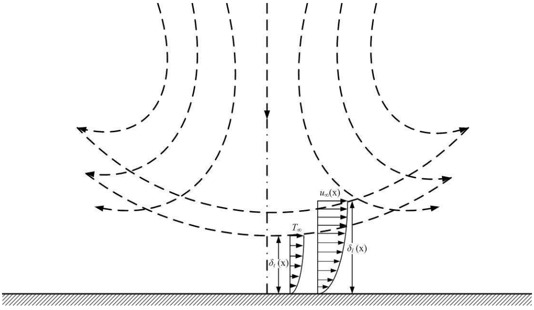

Figure 64 – Boundary layer formation beneath an impinging jet on a flat surface

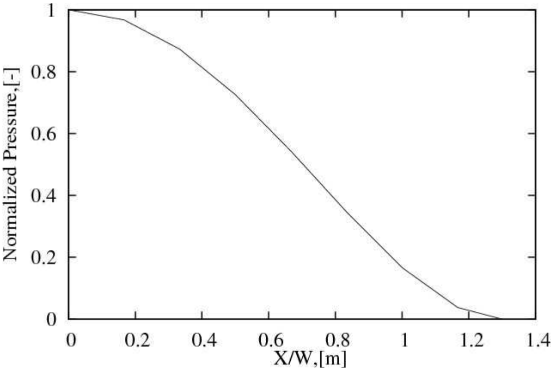

Figure 65 – Normalized Pressure distribution along the wall jet flow direction

Now, momentum equation for the free stream jet states in the following way:

$$\frac{\rho_l}{2}\frac{d(u_\infty^2)}{dx} = -\frac{dp}{dx} \tag{6.2}$$

Subsequently, solving the equations (6.1) and (6.2) the free-stream velocity and velocity gradient can be written as follows.

$$u_\infty = u_j\left[2\left(\frac{x}{1.3w}\right)^2 - \left(\frac{x}{1.3w}\right)^4\right]^{0.5} \quad 0 \le x \le 1.3w \tag{6.3}$$

$$\frac{du_\infty}{dx} = \frac{2u_j^2}{1.3wu_\infty}\left[\left(\frac{x}{1.3w}\right) - \left(\frac{x}{1.3w}\right)^3\right] 0 \le x \le 1.3w \tag{6.4}$$

At this instant, the energy equation can be written in the integral form comprising the additional thermal diffusivity in the liquid layer. The additional thermal diffusivity begets due to the turbulent flow at the stagnation region.

$$\frac{d}{dx}\int_0^{\delta_t(x)} u_\infty(\theta - \theta_\infty)dy' = -(\alpha_l + \alpha_t)\frac{d\theta}{dy'}\bigg|_{y'=0} \tag{6.5}$$

Here, $\delta_t(x)$ is the thickness of the thermal boundary layer.

Now, the third order polynomial determines the temperature profile in the following way:

$$\frac{\theta-\theta_{sat}}{\theta_{sat}-\theta_\infty} = \left(\frac{y'}{2\delta_t}\right)\left[\left(\frac{y'}{\delta_t}\right)^2 - 3\right] \tag{6.6}$$

The above temperature profile must satisfy the following boundary condition (equations 6.7-6.9) at the liquid-vapor interface ($y' = 0$) and at the outer edge of the thermal boundary layer ($y' = \delta_t$)

$$\theta|_{y'=0} = \theta_{sat} \tag{6.7}$$
$$\theta|_{y'=\delta_t} = \theta_\infty \tag{6.8}$$
$$\partial\theta/\partial y'|_{y'=\delta_t} = 0 \tag{6.9}$$

The thermal boundary layer thickness is determined by substituting the temperature profile obtained in equation (6.6), into the energy equation (6.5).

$$\frac{d\delta_t}{dx} = \frac{2(\alpha_l+\alpha_t)}{\delta_t u_\infty} - \frac{1}{2}\frac{\delta_t}{u_\infty}\frac{du_\infty}{dx} \tag{6.10}$$

Due to symmetry condition at the stagnation line at $x = 0$, the left-hand side of the equation (6.10) becomes zero and the thickness of the thermal boundary layer is given by:

$$\delta_t|_{x=0} = \left(\frac{1}{4(\alpha_l+\alpha_t)}\frac{du_\infty}{dx}\bigg|_{x=0}\right)^{-0.5} \tag{6.11}$$

Now, putting the value of the velocity gradient at the stagnation point, from equation (6.3) and (6.4), gives the following equation.

$$\left.\frac{du_\infty}{dx}\right|_{x=0} = \frac{2}{1.3}\frac{u_j}{w} \tag{6.12}$$

Now, the Reynolds number for the planar jet can be written in this manner.

$$Re_l = \frac{\rho_l u_j w}{\mu_l} \tag{6.13}$$

Hence, the following equation determines the thermal boundary layer at the stagnation region.

$$\delta_t|_{x=0} = w\left(\frac{2.6}{Re_l Pr_l}\right)^{0.5} \tag{6.14}$$

Now, rewriting the equation (6.10) including the additional thermal diffusivity as the following way.

$$0.5\frac{d\delta_t^2}{dx} + \frac{\delta_t^2}{u_\infty}\frac{du_\infty}{dx} = \frac{4(\alpha_l+\alpha_t)}{u_\infty} \tag{6.15}$$

The above equation has the following analytical solution.

$$\delta_t(x) = \frac{1}{u_\infty}\left\{8(\alpha_l + \alpha_t)\int_0^\infty u(\xi)d\xi\right\}^{0.5} \tag{6.16}$$

After that, the heat flux distribution at the liquid-vapor interface is computed as:

$$q_{lv} = -(\lambda_l + \lambda_t)\left.\frac{\delta\theta}{\delta y\prime}\right|_{y'=0} = 1.5(\lambda_l + \lambda_t)\frac{\Delta\theta_{sub}}{\delta_t} \tag{6.17}$$

The liquid properties are computed at the given bulk-liquid temperature as:

$$\theta_{i,bulk} = 0.5(\theta_\infty + \theta_{sat}) \tag{6.18}$$

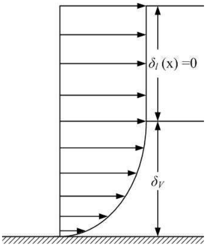

Figure 66 – Limiting flow condition of the vapor layer at the Leidenfrost point

In the stagnation region, the hydrodynamics of the vapor flow considers that the shear stress at the interface and in the liquid layer is invariant as shown in Figure 66. In the vapor layer, the pressure gradient in the normal to the flow is negligible compared to the pressure gradient in the downstream of the flow. The velocity gradient of vapor flow with respect to x is also negligible. Therefore, inside the vapor layer, the momentum equation states in the following way:

$$\mu\frac{\partial^2(u_v)}{\partial y^2}=\frac{dp}{dx} \tag{6.19}$$

The velocity profile must satisfy the following boundary conditions at the wall surface ($y = 0$) and at the liquid-vapor interface ($y=\delta_v$)

$$u_v|_{y=0}=0 \tag{6.20}$$

$$u_v|_{y=\delta_v}=u_\infty \tag{6.21}$$

$$\partial u_v/\partial y|_{y=\delta_v}=0 \tag{6.22}$$

The vapor layer thickness is obtained at the Leidenfrost point as the following way:

$$\delta_v=\ (\rho_l/2\mu_v)(\,du_\infty/dx)|_{x=0})^{-0.5} \qquad 0\le x\le 1.3w \tag{6.23}$$

$$\delta_v|_{x=0}=\ \left(1.3\mu_v w/\rho_l u_j\right)^{0.5} \tag{6.24}$$

$$q_w\approx\{\left((\lambda_l+\lambda_t)\Delta\theta_{sub}\right)/w\}Re^{0.5}Pr^{0.5} \tag{6.25}$$

λ_t (turbulent-thermal-diffusivity) can be determined through the Rayleigh-Taylor instability analysis. The convection and radiation are negligible as compared to the convective heat transfer rate into the liquid. Rather, assumes that the heat transfer between the surface and the liquid takes place via conduction through the vapor layer. The wall superheat calculated from the following expression:

$$\Delta\theta_{sat}=\ q_w\delta_v/\lambda_v=((\lambda_l+\lambda_t)/\lambda_v)\,(\delta_v/w)\,Re^{0.5}Pr^{0.5}\Delta\theta_{sub} \tag{6.26}$$

Furthermore, putting the value of the film thickness from equation (6.23) into equation (6.26) read the following equation:

$$\Delta\theta_{sat} = 1.140((\lambda_l + \lambda_t)/\lambda_v)\,(\mu_v/\mu_l)^{0.5}\, Pr^{0.5}\Delta\theta_{sub}$$

The vapor properties are strong functions of the vapor temperature and computed at the bulk vapor temperature given as:

$$\theta_{v,bulk} = (\theta_w + \theta_{sat})/2 \qquad (6.27)$$

The computation of the vapor layer thickness and wall temperature is initiated with vapor properties calculated at an assumed temperature of 500 K. The properties are iteratively updated with a convergence criterion of 0.005%.

6.2.2. Model for the circular jet

In the case of circular jet impingement, the stagnation region spans, about 1.15 times the jet diameter in the case of the multiphase flow. Pressure distribution follows the fourth order polynomial at the jet stagnation region.

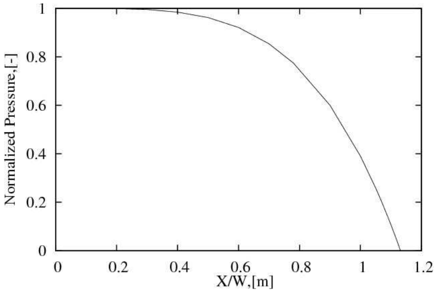

Figure 67 – Normalized pressure distributions along the radial direction of the flow

The pressure distribution along the radial direction is given in the following Figure 67. The pressure distribution is given by the following equation.

$$\frac{P}{0.5\rho_l u_j^2} = 1 - 0.6\left(\frac{r}{D}\right)^4 \qquad (6.28)$$

The free stream velocity of the jet can be determined from Euler's equation as follows:

$$\frac{\rho_l}{2}\frac{d(u_\infty^2)}{dr} = -\frac{dP}{dr} \qquad (6.29)$$

The velocity and velocity gradient are determined using the equations (6.28-6.29) by the following equation:

$$u_\infty = 0.775 u_j \left(\frac{r}{d_j}\right)^2 \qquad 0 \le r \le 1.15 d_j \tag{6.30}$$

$$\frac{du_\infty}{dr} = 1.55 \frac{u_j r}{d_j^2} \qquad 0 \le r \le 1.15 d_j \tag{6.31}$$

The equation for the energy balance in the liquid layer can be formulated in an integral form as follows:

$$\frac{d}{dr}\int_0^{\delta_t(r)} u_\infty(\theta - \theta_\infty)dy' + \int_0^{\delta_t(r)} \frac{u_\infty}{r}(\theta - \theta_\infty)dy' = -(\alpha_l + \alpha_t)\frac{d\theta}{dy\prime}\bigg|_{y'=0} \tag{6.32}$$

The thermal boundary layer thickness defined as:

$$\frac{d\delta_t}{dr} = \frac{4}{2.325}\frac{(\alpha_l+\alpha_t)}{\delta_t u_j}\frac{d_j^2}{r^2} - 1.5\frac{\delta_t}{r} \tag{6.33}$$

Due to symmetry around the stagnation axis, the derivative of the thermal layer thickness should be equal to zero.

$$\frac{d\delta_t}{dr}\bigg|_{r=0} = 0 \tag{6.34}$$

The thickness of the thermal layer is given by the following equation:

$$\delta_t = 1.14 d_j (Re_l Pr_l)^{-0.5} 0 \le r \le 1.15 d_j \tag{6.35}$$

Now, the Reynolds number is defined in this manner.

$$Re_l = \frac{\rho_l u_j d_j}{\mu_l} \tag{6.36}$$

Since the heat flux transported through evaporation and convection is very small, the heat flux distribution at the wall can be computed only by the conduction through the vapor:

$$q_w = q_{lv} = -(\lambda_l + \lambda_t)\delta\theta/\delta y'|_{y'=0} = 1.5(\lambda_l + \lambda_t)\,\Delta\theta_{sub}/\delta_t \tag{6.37}$$

Putting the value of δ_t from equation (6.35) into equation (6.37) then wall heat flux is given by the following equation:

$$q_w = 1.31(\lambda_l + \lambda_t)\,(\Delta\theta_{sub}/d_j) Re_l^{0.5} Pr_l^{0.5} \tag{6.38}$$

Now, for the calculation of the vapor layer, the momentum equation for the vapor layer is simplified as:

$$\mu_v \frac{\partial^2 u_v}{\partial y^2} = \frac{dP}{dr} \tag{6.39}$$

We know the pressure distribution in the radial direction from equation (6.28), after some solving this equation the vapor layer is given by:

$$\delta_v = 1.136\sqrt{\frac{\mu_v d_j}{\rho_l u_j}} = 1.136 d_j Re_l^{-0.5}\left(\frac{\mu_v}{\mu_l}\right)^{0.5} \qquad 0 \le r \le 1.15 d_j \tag{6.40}$$

Now, again putting the value of the vapor layer thickness δ_v from equation (6.40) the wall superheat is given by:

$$\Delta\theta_{sat} = q_w \delta_v/\lambda_v = 1.4886((\lambda_l + \lambda_t)/\lambda_v)\,(\delta_v/w)\,Re^{0.5} Pr^{0.5} \Delta\theta_{sub} \tag{6.41}$$

6.3. Rayleigh-Taylor instability criteria

Rayleigh-Taylor instability theory determines the turbulent thermal diffusivity. The stable system can be defined as when a physical system can withstand a disturbance or return to its original state after small deviation, otherwise, it is said to be an unstable state. Here, the effect of a particular disturbance on the physical state is analyzed.

The disturbance ϕ' is assumed for the basic solution of ϕ and is added to this basic solution. Then $\phi + \phi'$ will be substituted into the governing equations. The ϕ can be velocity, pressure, temperature or any variables. After that, governing equations with ϕ are then subtracted from the governing equation with $\phi + \phi'$, which yields a disturbance equations ϕ' as dependent variables. If the system is stable then it should damp out. Otherwise, if it increases with time, then ϕ is unstable.

It is assumed that the fluid is incompressible, inviscid and immiscible flows in a horizontal tube and the heavier fluid overlays a less dense fluid as in Figure 67. A disturbance $\zeta(x, t)$ at the interface is employed, assuming that interface may become unstable. This instability is called as *Rayleigh-Taylor* instability.

Assuming, that multiphase flows are two-dimensional, the governing equations for this flow as in Figure 67 are given by these equations.

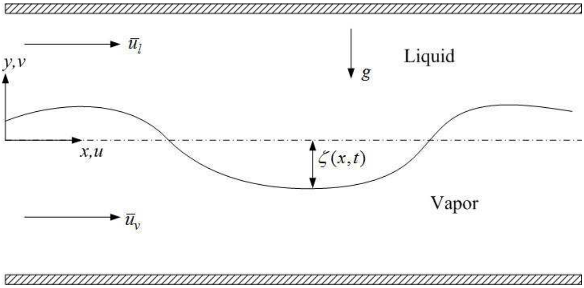

Figure 68 – Rayleigh-Taylor Instability for dense liquid overlay less dense vapor

$$\frac{\partial u}{\partial x} + \frac{\partial v}{\partial y} = 0 \tag{6.42}$$

$$\rho\left[\frac{\partial u}{\partial t} + u\frac{\partial u}{\partial x} + v\frac{\partial u}{\partial y}\right] = -\frac{\partial p}{\partial x} \tag{6.43}$$

$$\rho\left[\frac{\partial v}{\partial t} + u\frac{\partial v}{\partial x} + v\frac{\partial v}{\partial y}\right] = -\frac{\partial p}{\partial y} - \rho g \tag{6.44}$$

The velocities and pressure are decomposed as follows into mean flow component and the perturbed components:

$$u = \bar{u} + u', v = \bar{v} + v', p = \bar{p} + p' \tag{6.45}$$

Substituting equation (6.45) into equation (6.42) - (6.44) and considering the fact that the base flow should satisfy the equation (6.42) - (6.44), now, the equation for the perturbed flow simplifies to

$$\frac{\partial u\prime}{\partial x} + \frac{\partial v\prime}{\partial y} = 0 \tag{6.46}$$

$$\rho\left[\frac{\partial u\prime}{\partial t} + \bar{u}\frac{\partial u\prime}{\partial x}\right] = -\frac{\partial p\prime}{\partial x} \tag{6.47}$$

$$\rho\left[\frac{\partial v\prime}{\partial t} + \bar{u}\frac{\partial v\prime}{\partial x}\right] = -\frac{\partial p\prime}{\partial y} \tag{6.48}$$

The product of perturbation (primed) terms are neglected and also, we found that $\frac{\partial \bar{u}}{\partial x} = \frac{\partial \bar{v}}{\partial y} = \bar{v} = 0$ doing this treatment in the equations (6.46) - (6.48).

Now, differentiating equations (6.47) and (6.48) with respect to x and y, respectively, then adding them and substituting the continuity equations, yields the Laplace equation for the pressure perturbation field:

$$\frac{\partial^2 p\prime}{\partial x^2}+\frac{\partial^2 p\prime}{\partial y^2}=0 \tag{6.49}$$

The shape of the interface at time *t* can be described by this equation:

$$\zeta(x,t)=Ae^{ikx+\omega t} \tag{6.50}$$

And the perturbation quantities v' and p' can be written in the following way:

$$v'(x,y,t)=\hat{v}e^{ikx+\omega t} \tag{6.51}$$

$$p'(x,y,t)=\hat{p}e^{ikx+\omega t} \tag{6.52}$$

Where $\hat{v}$ and $\hat{p}$ are the magnitude of the perturbation.

Employing the Young-Laplace equation and the equation for the curvature of the liquid film, $p_v-p_l=k/R$. Carey and Murray (1989) used the perturbation analysis to obtain the following condition for an unstable interface.

$$|\bar{u}_l-\bar{u}_v|^2>\frac{[\sigma k+(\rho_l-\rho_v)g/k](\rho_l+\rho_v)}{\rho_l\rho_v} \tag{6.53}$$

Where, $k=2\pi/l$ is the wave number, the right side of this inequality has a minimum when the wave number is equal to a critical wave number k_{crit}

$$k_{crit}=\left[\frac{(\rho_l-\rho_v)g}{\sigma}\right]^{0.5} \tag{6.54}$$

The critical wavelength corresponding to the critical wave number is

$$l_c=2\pi\left[\frac{\sigma}{(\rho_l-\rho_v)\gamma_{tot}}\right]^{0.5} \tag{6.55}$$

In Figure 63, it is assumed that a vapor layer exists in the vicinity of the heated surface and then vapor-liquid interface and then a sub-cooled liquid layer exists. As the jet impinges on the heated surface, the liquid has a tendency to penetrate the vapor layer, thus, instigated the unstable interface. Henceforward, it is understood that the inertia force and gravitational force are the causes of the instability. Indeed, the liquid jet acceleration must include also a gravitational force, which is characterized by an equivalent acceleration γ. This jet acceleration can be given by the following equation:

$$\gamma=\frac{u_j^2}{d_j} \tag{6.56}$$

Where u_j is the impinging jet velocity near the stagnation region and the d_j (m) is the hydraulic diameter of the jet, which is equal to jet diameter in the case of the circular jet. Hence, the gravitational acceleration as well as the acceleration due to the jet hydrodynamics, the total acceleration becomes $\gamma_{tot}=\gamma+g$. Then the critical diameter from the equation (6.55) can be written as:

$$d_c = 2\pi\left[\frac{\sigma}{(\rho_l-\rho_v)\gamma_{tot}}\right]^{0.5} \tag{6.57}$$

It is assumed that the turbulence length scale is always less than this critical length scale. Therefore, the turbulence length scale from the above equation can be determined by the following equation:

$$l = \pi\left[\frac{C_1\sigma}{(\rho_l-\rho_v)\gamma_{tot}}\right]^{0.5} \tag{6.58}$$

In the equation (6.58), the value of the C_1 for the planar jet is 0.316228 and for round jet is 0.14121.

The critical wave number at the stagnation region will be

$$k_{crit,\ stag} = d_j\left[\frac{(\rho_l-\rho_v)\gamma_{tot}}{\sigma}\right]^{0.5} \tag{6.59}$$

Yet again, the wave number will be less from the critical wave number in the turbulent film boiling regime at the stagnation region of the jet. Due to high jet acceleration along the impingement region, the value of C_2 will be 0.3 for planar jet and 0.1 for the round jet.

$$k_{stag} = C_2 d_j\left[\frac{(\rho_l-\rho_v)\gamma_{tot}}{\sigma}\right]^{0.5} \tag{6.60}$$

The above constants are determined on the basis of the existing experimental investigations [ref.]. It has been assumed that momentum boundary layer and thermal boundary layer thickness are same, i.e., the Prandtl number for the turbulent flow at stagnation region is around one. Therefore, the turbulent momentum diffusivity assists in finding the turbulent thermal diffusivity of the flow.

Now, the turbulent conductivity will be given by this formula. The vapor generated at the stagnation region is responsible for the generation of the turbulent kinetic energy.

$$\lambda_t = \varepsilon_m \rho_v C_{pv} \tag{6.61}$$

$$\varepsilon_m = k_{stag}\sqrt{l^3\gamma_{tot}} \tag{6.62}$$

Now we can use the equations (6.58), (6.60), (6.61) and (6.62), for turbulent induced conductivity in the above planar jet and round jet analysis to determine the wall superheat and the wall heat flux.

6.4. Results and discussion

Subsequently, formulation of the Leidenfrost phenomenon considers the effect of turbulence to determine the heat flux and wall-superheat. Comparison from the existing literature gives out satisfactory results. From Ref. [Ishigai, (1978)] in Table 7 for jet velocity 2.17 m/s and the water sub-cooling 35 K, the new model under predicts heat-flux only 13.7% to the experimental value. While the model by Ishigai, et al., (1978) under predicted the heat flux up to 60-70%. On the other hand, for jet velocity 1.14 m/s in Ref. [Ishigai, (1978)] in Table 7, present model over predicts the heat flux by 4.5%.

Wall superheat is over predicted around 0.23% and 5.1% in Table 8 in Ref. [Ishigai (1978)] for jet velocity 2.14 m/s and 1.14 m/s respectively. In case of lower jet velocity and water sub-cooling Ref. [Robidou et al., (2002)], [Bogdanic et al., (2009)] and [Seiler et al., (2004)] minimum error in the prediction of heat flux is +1.3% for Ref. [Seiler et al., (2004)] in Table 7, while the maximum error is -31.1% for water sub-cooling 7 K, the jet width and the jet velocity are 0.9 mm and 0.78 m/s. One may overlook this error, because, of the fact that, in actual practice in the steel industry, there are always higher velocity and water sub-cooling.

The present model under predict the wall heat flux by 5.7 % and wall superheat by 20 % in comparison with experimental values by Bogdanic et al., (2009). While the other author's model [Karwa et al., (2011)] predict approximately 12% less wall heat flux and wall superheat 40% less. Hence, the present model under predicts the film thickness 5.2 µm as compared to the experimental results of Bogdanic et al., (2009), which shows the vapour layer around 8±2 µm. Since the present model predicts better wall heat flux and wall superheat, therefore, the vapour film thickness is more reliable than another model. The only paper by Liu, 2003, which have the experimental results for the circular jet impingement. For jet velocity 3 m/s, 10 mm jet diameter and 15 K water sub-cooling, the present model over predicts the heat flux by 13.3% (Table 7), on the other side, for higher sub-cooling around 45 K, the present model under predicts by 11.8%. While Liu's (Liu, 2003) correlation predicts ±25% of the heat flux and ± 30% of wall superheat. While, the present model overestimates only around 1.83% of wall heat flux and 6.38% of wall superheat for 75 K liquid sub-cooling and the jet velocity 3.31 m/s as in Ref. (Hall, et al., 2001). Which are quite good agreements with experiments for prediction of the wall heat flux and wall superheat. It has been recognized from the experiment and the analysis that the wall heat flux and wall superheat are function of the vapour film thickness. As the measurement of the vapor film thickness is quite cumbersome due to the complexity in the measuring technique in such a low thickness of the vapor film exhibiting unstable phenomena. Although, the film thickness along with liquid sub-cooling, wall superheat and the jet velocity have been analyzed. The data for determination of the film thickness has been taken from the Ref. (Liu, 2003).

Figure 69 depicts about the fact that, even for higher sub-cooling 45 K and higher jet velocity 3 m/s, the film thickness is around 9.34 µm, reason may be due to quite a high wall superheat around 750 K. As, one can move to less wall superheat the existence of the vapour film can be seen, because, of the less liquid sub-cooling. Although, the film thickness decreases with decreased wall superheat.

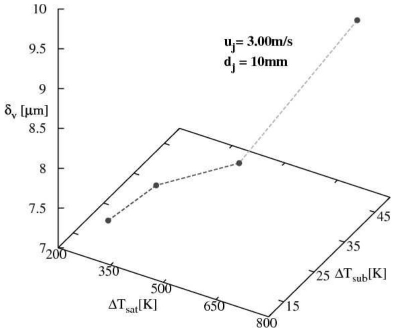

Figure 69 – Film thickness with wall superheat and liquid sub-cooling

Therefore, it can be said that the liquid sub-cooling can also trigger the film boiling phenomena at low wall superheat and at high jet velocity. Since, the effect of jet velocity on the film thickness is as the jet velocity increases the film thickness decreases. As discussed earlier that the less liquid sub-cooling temperature can stimulate the film boiling phenomena even at low temperature of wall. For wall superheat 350 K and sub-cooling 25 K the film thickness is more than the wall superheat 300 K and sub-cooling 15 K. The reason may be due to the higher temperature of liquid (lower sub-cooling temperature) activates the film boiling even at lower wall superheat.

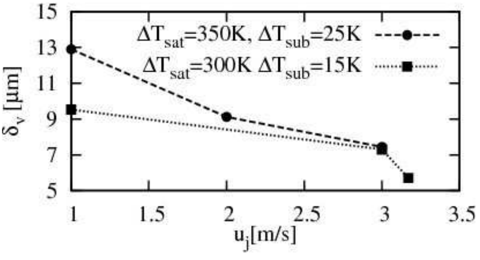

Figure 70 – Film thickness with jet velocity

The wall superheat has a significant effect at low jet velocity, while for higher jet velocity wall superheat (the difference between two experiment is 50 K Figure 70) has less effect. The effect of 10 K sub-cooling difference is not predominant here. This implies that the inertia induced instability plays a significant role for the film thickness at higher jet velocities.

The film thickness in case of the jet velocity 3.31 m/s, liquid sub-cooling 75 K and wall superheat 550 K has been calculated around 1.85 µm. It concludes that, even for high sub-cooling and jet velocity, we cannot neglect the film boiling phenomena.

These are the important conclusions; one can further verify these with more experimental results. Thus far, experimental results published for film boiling phenomena for the jet stagnation region, which derived us from revealing the physics of the flow film boiling phenomena at jet stagnation region to some extent. The above validation of wall heat flux and wall superheat has a quite nice agreement with the experimental results.

Table 7 – Comparison of the wall heat flux with the published data

Ref.	*Parameters,* w or d, u_j ΔT_{sub}	x *(mm)*	$q_{w,}$ measured *(MW/m²)*	$q_{w,}$ predicted *(MW/m²)*	$\left(\frac{q_{w,p}}{q_{w,m}}-1\right)\%$
[55]	6 mm, 2.17m/s, 35K	0≤x≤6	1.53	1.32	-13.7
[55]	5.5mm,1.14m/s, 35K	0≤x≤6	0.88	0.92	+4.5
[103]	0.72mm,0.56m/s, 20K	0	0.87	0.82	-5.7
[103]	0.9mm,0.78m/s, 17K	0	0.94	0.73	-22.3
[103]	0.92mm,0.87m/s, 16K	0	1	0.72	-28
[103]	0.92mm,0.87m/s, 13.5K	0	0.6	0.608	+1.3

[103]	0.9mm, 0.78m/s, 7K	0	0.45	0.31	-31.1
[107]	10mm, 3.0m/s, 45K	0	1.8	1.59	-11.8
[107]	10mm, 3.0m/s, 35K	0	1.1	1.21	+10.6
[107]	10mm, 3.0m/s, 15K	0	0.45	0.51	+13.3
[107]	6.2mm,3.17m/s, 15K	0	0.8	0.66	-17.1
[107]	6.2mm,1m/s, 15K	0	0.4	0.37	-7.4
[43]	4.855mm, 3.31m/s, 75K	0	3.8	3.87	+1.83

Table 8 – Comparison of the wall superheat with the published data

Ref.	*Parameters,* w or d, u_j ΔT_{sub}	x *(mm)*	$\Delta\theta_{sup.measured}$	$\Delta\theta_{sup.predicted}$	*% error*
[55]	6 mm, 2.17m/s, 35K	$0 \leq x \leq 6$	820	821.86	+0.23
[55]	5.5mm,1.14m/s, 35K	$0 \leq x \leq 6$	440	462.45	+5.10
[103]	0.72mm,0.56m/s, 20K	0	280	285.38	+1.92
[103]	0.9mm,0.78m/s, 17K	0	380	268.12	-29.44
[103]	0.92mm,0.87m/s, 16K	0	350	253.16	-27.67
[103]	0.92mm,0.87m/s, 13.5K	0	327	261.40	-20.06
[107]	10mm, 3.0m/s, 45K	0	750	781.69	+4.23
[107]	10mm, 3.0m/s, 35K	0	500	548.86	+9.77
[107]	10mm, 3.0m/s, 15K	0	300	316.75	+5.58
[107]	6.2mm,3.17m/s, 15K	0	300	313.99	+4.65
[107]	6.2mm,1m/s, 15K	0	275	294	+6.91
[43]	4.855mm, 3.31m/s, 75K	0	550	585.10	+6.38

7. Conclusions and Future Recommendations

7.1. Surface quenching through single jet

The computational study has been performed in order to enhance the understanding of the flow quenching phenomena for the single jet impinging onto a heated plate. Temporal evolution of the boundary layer profile demonstrated the dynamic nature of the flow boiling evidenced by the formation, growth and explosion of the vapor bubbles near the surface. The velocity gradient exhibits a linear behavior in the case of a higher vapor volume fraction at the surface. On the other hand, it is non-linear in the case of the vapor-liquid mixture. This behavior is also due to the different heat-transfer mechanism (nucleate boiling, transition boiling and film boiling). The boundary layer profile development, evaluated at different radial positions, indicates that the viscous sublayer and the buffer layer are highly unstable, representing the outcome caused by the boiling of the liquid. The fast cooling from the time of initialization of quenching to 2 *s* is achieved at the stagnation region, while slow cooling rate represents the characteristics of the later time period. It clearly shows the effect of liquid sub-cooling which is initially very high. For a longer time, the liquid forms the vapor layer at the surface being incapable of escaping from the stagnation region. Higher values of heat-flux are found at the jet acceleration region in comparison with wall jet region. For higher jet velocities (7.5 *m/s* and 10 *m/s*), the acceleration region exhibits more intensive heat flux removal from the surface. For higher wall superheat at the initial time, the quenching phenomena are more pronounced at jet stagnation region where the bubble production rate is quite high. Herewith, a more intensive momentum and thermal diffusivity exchange hinder the wall-jet acceleration at the surface after the stagnation region accordingly; this phenomenon enhances the cooling rate at stagnation region for lower jet velocities.

Temporal evolution of the heat transfer mechanism is discussed in detail. For longer times, e.g. around 7 *s*, less number of bubbles are produced leading to a lower vapor fraction generated at the stagnation region. It causes a more intensive wall-jet acceleration and consequently an intensified momentum transport and thermal diffusivity, leading finally to a substantial cooling rate enhancement at the jet acceleration region. In the boiling curve, the shoulder of heat flux is not found for the sub-cooling 75 K. Shoulder of heat flux is commonly achieved for sub-cooling 45 K and 10 K, representing the outcome which can be evidenced in the experiment by Gradeck, et al. (2009). The effect of the sub-cooling on heat flux removal rate from the heated surface is more pronounced than that of the jet velocity. Effect of flow velocity has been examined in detail, which is relevant to the many industrial quenching applications.

Intensive quenching process is consistent with the high rate of sub-cooling and high jet velocities. The surface temperature predicted by quenching model within the impingement region and the consequent wall-jet region agrees reasonably well with the measurements, the outcome being particularly valid at higher jet velocities. However, a steep temperature gradient at the position corresponding to the boiling threshold was not captured under the conditions of the numerical grid resolution adopted. Despite, reasonably good predictions of the wetting front propagation phenomena have been achieved, advocating the necessity for future development of the model.

7.2. Theoretical and numerical study of the hydrodynamics of the multiple jets

A theoretical model for the determination of the pool height for the given mass flow rate is proposed. The model results are compared to those obtained from the CFD study showing good agreement. The flow characteristics are also analyzed resulting in the maximum value of the non-dimensional mass flow rate corresponding to 0.3849 for the non-dimensional height around 0.66. This implies that for certain liquid pool height the flow rate becomes maximum. This can be useful for determination of the optimum flow rate and the liquid pool height. It has been realized that the honeycomb-like nozzle array distribution can enhance the heat-transfer rate, because, this exhibited the most intensive interactions of the jets. Intensification of the jet interactions is also of importance in relation to the heat transfer rate enhancement. It is especially the case if the jet interactions take place before the hydraulic jump appearance, which, on the other hand, could create a high level of up wash. Static pressure distribution on the surface affected the heat flux removal rate by a corresponding liquid-pool height level. The liquid pool height in one hand can hinder the heat-flux removing capacity by damping the thermal diffusivity. However, on the other hand, the higher average velocity of the flow and higher vapor formation rate permitted higher drag force to enable escape of the vapor from the edge of the plate. Therefore, the high average velocity of the flow is a desirable feature for fast removal of heat flux at the high initial temperature of the surface. Because, at a high initial temperature of the surface, the vapor formation rate will be appropriately high supporting the flow velocity of the water pool to drag the vapor from the middle of the surface to the edge. Nevertheless, in the case of the lower initial surface temperature, both factors would be less important for the removal of heat-flux. Apart from these studies, a model for the prediction of the temperature for multiple jets impingement on the heated surface is proposed, which can be useful for the engineering purposes.

7.3. Model for film boiling at stagnation region considering the effect of instability

The model for the prediction of the heat flux and surface temperature is developed for the film boiling at stagnation region. The interface between the liquid and vapor is highly unstable. This instability affects the turbulence increase and, consequently, the increase in the thermal diffusivity. A significant improvement in the prediction of the heat flux and the wall superheat was illustrated in direct comparison with available experimental results. Moreover, the model shows lower error for higher jet velocities and higher sub-cooling. The results for the film thickness in terms of the jet velocity, wall superheat and liquid sub-cooling enable important conclusions to be drawn.

7.4. Future Recommendations

Having the computational database obtained by the present research about the influence of the boundary layer development and associated turbulence structure, one can work on a reformulation of the quenching model. Another aspect can also be included, representing the boiling-front propagation characteristics. Further experimental studies for the model validation would be necessary, keeping in mind the transient nature of the quenching phenomenon, which is certainly difficult to reproduce correctly. Knowledge of the flow parameters as well as thermal and material properties of solid surface is of decisive importance. The model should be developed for a larger range of operating parameters such as jet velocity, sub-cooling intensity, wall-superheat in terms of different surface thermal properties. Testing the quenching model should be performed by computing the multiple jet process keeping in mind that the relevant phenomena are much richer in comparison with the single jet. It relates especially to very complex hydrodynamics. As shown presently, the jet interactions, liquid pool height and the associated mean velocity and turbulent kinetic energy may contribute significantly to the heat transfer process. The non-linear dependence of these parameters on the complex hydrodynamics along with the boiling at the surface is evident.

Fast cooling of the surface starting from very high initial temperatures may lead to film boiling. An analytical model, proposed in the present work, should be validated experimentally; furthermore it can be done accounting for a wide range of operating parameters.

Introduction of the surface roughness effects in the wall–function method can mimic the multiphase flow near the surface more generally. It can be implemented along with the boiling front propagation characteristics.

List of Figures

List of Tables

References

[1] Akio, F., Sadanori, I., Yoshimich, H., Toru, M., Yoichi, M., Shozo, I. (2002), EP Patent Application EP 1 210 993 A1.

[2] Andreani, M. and Yadigaroglu, G., (1992), "Difficulties in modelling dispersed-flow film boiling", Wärme- und Stofffübertragung, **27**, pp. 37-49.

[3] Auracher, H., Buchholz, M., (2005), "Experiments on The Fundamental Mechanisms of Boiling Heat Transfer", *J. of the Brazilian Society of Mechanical Science & Engineering*, Jan-March, **XXVII** (1), 2005.

[4] Auracher, H., Marquardt, W., (2004), "Heat transfer characteristics and mechanisms along entire boiling curves under steady-state and transient conditions", Int. J. Heat Fluid Flow, **25**, pp. 223–242.

[5] Avdeev, A. A., Zudin, Y. B., (2005), "Inertial-thermal governed vapor bubble growth in highly superheated liquid", Heat Mass Transfer, **41**, pp. 855–863.

[6] AVL FIRE Manual, (2009), AVL List GmbH, Graz

[7] Azuma, T., Hoshino, T., (1984), "The radial flow of thin liquid film", Trans. Jpn. Mech. Engrs., **50**, pp. 974–1136.

[8] Banerjee, D., and Dhir, V. K., (2001)^1,"Study of subcooled film boiling on a horizontal disc: Part I—Analysis", J. Heat Transf., **123**, pp. 271-284.

[9] Banerjee, D., and Dhir, V. K., (2001)^2, "Study of subcooled film boiling on a horizontal disc: Part 2—Experiments", J. Heat Transf., **123**, pp. 285-293.

[10] Basara B. Jakirlic, S., (2003),"A new hybrid turbulence modelling strategy for industrial CFD," Int. J. Numer. Meth. Fluids, **42**, pp. 89–116.

[11] Baumeister, K. J., Hamill, T. D., (1967), "Laminar flow analysis of film boiling from a horizontal wire", NASA TN D-4035.

[12] Behnia, M., and Parneix, S. Durbin, P.A., (1998), "Prediction of heat transfer in an axisymmetric turbulent jet impinging on a flat plate", International Journal of Heat Mass Transfer, **41**(12), pp. 1845-1855.

[13] Biswas, S. K., Chen, S-J., Satyanarayana, A., (1997), "Optimal temperature tracking for accelerated cooling processes in hot rolling of steel", Dynamics and Control, **7**, pp. 327-340

[14] Bogdanic, L., Auracher, H., Ziegler, F., (2009), “Two-phase structure above hot surfaces in jet impingement”, Heat Mass Transfer, **45**, pp. 1019-1028.

[15] Bohr, T., Dimon, P., Putkaradze, V., (1993), “Shallow water approach to the circular hydraulic jump”, J. Fluid Mech. **254**, pp. 635–648.

[16] Borisenko, A.I., and Tarapov, I.E, (1968), "Vector and tensor analysis with applications", Prentice Hall, Inc., Englewood Cliffs, N.J., USA.

[17] Borzi, A., "Swift AMG", Tech. Report AST-2000-009, Graz, 2000.

[18] Bromely, L. A., (1950), “Heat transfer in stable film boiling” Chem. Eng. Prog. **58**, pp. 67-72.

[19] Buyevitch, Y. A., Ustinov, V.A., (1994), “Hydrodynamic conditions of transfer processes through a radial jet spreading over a flat surface”, Int. J. Heat Mass Transfer, **37** (1), pp. 165–173.

[20] Carey, G.F., Murray, P., (1989), “Perturbation analysis of a shrinking core”, Chemical Engineering Science, **44**(4), pp. 979-983.

[21] Casey, M., Wintergerste, T., (2000), “ERCOFTAC Special Interest Group on “Quality and Trust in Industrial CFD-Best practice guidelines”, ERCOFTAC.

[22] Castrogiovanni, A., Sforza, P.M., (1997), “A Genetic Algorithm Model for High Heat Flux Flow Boiling”, Experimental Thermal and Fluid Science, **15**, pp. 193-201.

[23] Cho, M. J., Thomas, B.G., Lee, P. J., (2008), “Three-Dimensional numerical study of impinging water jets in runout table cooling processes”, Metallurgical and Materials Transactions B, **39**B, pp. 593–602

[24] Chou, X. S., Sankaran, S., Witte, L. C., (1995), “Subcooled flow film boiling across a horizontal cylinder: Part II--Comparison to Experimental Data”, J. Heat Transf., **117**, pp. 175–178.

[25] Chou, X. S., Witte, L. C., (1995), “Sub-cooled flow film boiling across a horizontal cylinder: Part I- Analytical Model”, J. Heat Transfer, **117**, pp. 167–174.

[26] Coury, G. E., Duckler, A. E., (1970), “Turbulent film boiling on vertical surfaces. A study including the influence of interfacial waves”, Proceedings of Int. Heat Transfer Conf., Paris, Paper No. B.3.6.

[27] Demirdzic, I., Lilek, Z., Peric, M. (1993) "A collocated finite volume method for predicting flows at all speeds", Int. Journal for Numerical Methods in Fluids, **16**, pp. 1029-1050.

[28] Durbin, P.A. (1995) "Separated flow computations with the k-ε-v^2 model", AIAA Journal, **33**, pp. 659-664.

[29] Esmaeeli, A., Tryggvason, G., (2004), “Computations of film boiling. Part I: numerical method” International Journal of Heat and Mass Transfer, **47**, pp. 5451–5461.

[30] Esmaeeli, A., Tryggvason, G., (2004), “Computations of film boiling. Part II: numerical method” International Journal of Heat and Mass Transfer, **47**, pp. 5463–5476

[31] Faghri, A., Zhang, Y., (2010), ‘Transport Phenomena in Multiphase Systems’, Elsevier Inc.

[32] Ferziger, J., Peric, M., 1997, "Computational methods for fluid dynamics", Springer, Berlin.

[33] Filipovic, J., Viskanta, R., and Incropera, F. P., (1993), “Similarity solution for laminar film boiling over a moving isothermal surface”, Int. J. Heat Mass Transf, **36**(12), pp. 2957-2963.

[34] Filipovic, J., Viskanta, R., and Incropera, F. P., (1994), “An analysis of subcooled turbulent film boiling on a moving isothermal surface”, Int. J. Heat Mass Transf, **37**(17), pp. 2661-2673.

[35] Frigg, R., (2004), “In what sense is the Kolmogorov-Sinai entropy a measure for chaotic behaviour? - Bridging the gap between dynamical systems theory and communication theory”, Journal for the Philosophy of Science, **55**, pp. 411-434.

[36] Fuchang, Xu., Mohamed S. Gadala, (2006), “Heat transfer behavior in the impingement zone under circular water jet”, Int. J. Heat and Mass Transf., **49**, pp. 3785–3799.

[37] Fuchs, T., Kern, J., Stephan, P., (2006), “A transient nucleate boiling model including microscale effects and wall heat transfer”, ASME Journal of Heat Transfer, **128**, pp. 1257-1265.

[38] Fujimoto, H., Hatta, N., and Viskanta, R., (1999), “Numerical simulation of convective heat transfer to a radial free surface jet impinging on a hot solid”, Heat and Mass Transf., **35**, pp. 266-272.

[39] Gambill, W. R. and Lienhard, J. H., (1989), “An upper bound for the critical boiling heat flux”, ASME J. Heat Transfer, **111** (3), pp. 815-818.

[40] Gaskell, P.H., Lau, A.K.C., (1988), "Curvature-compensated convective transport: SMART, A new boundedness preserving transport algorithm". Int. J. for Numerical Methods in Fluids, **8**, pp. 617-641.

[41] Gradeck, M., Kouachi, A, Dani, A., Arnoult, D., Borean, J. L., (2006), “Experimental and numerical study of the hydraulic jump of an impinging jet on a moving surface”, Exp. Thermal Fluid Sci., **30**, pp. 193-201.

[42] Gradeck, M., Kouachi, A., Lebouché, M., Volle, F., Maillet, D., Borean, J. L., (2009), “Boiling curves in relation to quenching of a high temperature moving surface with liquid jet impingement”, Int. J. Heat Mass Transf, **52**, pp. 1094–1104.

[43] Hall, D. E., Incropera, F. P., Viskanta, R., (2001), “Jet impingement boiling from a circular free-surface jet during quenching: Part 1—Two-phase jet”, Journal of Heat Transfer, **123**, pp. 911-917.

[44] Hamill, T. D., and Baumeister, K. J. (1967), ‘‘Effect of subcooling and radiation on film-boiling heat transfer from a flat plate,’’ NASA TND D-3925.

[45] Hanjalic, K., Popovac, M., Hadziabdic, M., (2004), “A robust near-wall elliptic-relaxation eddy-viscosity turbulence model for CFD”, Int. J. Heat Fluid Flow, **25**(6), pp. 1047-1051.

[46] Harten, A., (1983), "High-resolution schemes for hyperbolic conservation laws". J. of Computational Physics, **49**, pp. 357-393.

[47] Hatta, N., and Osakabe, H., (1989), “Numerical modelling for cooling a laminar water curtain”, ISIJ International, **29**(11), pp. 919-925.

[48] Hatta, N., Tanaka, Y., Takuda, H., Kokado, J-I., (1989), “A numerical study on cooling process of hot steel plates by a water curtain”, ISIJ International, **29**(8), pp. 673-679.

[49] Herman, J.C., (2001), Iron making and Steel making, **28**, pp. 159–63.

[50] Hirt, C.W., Nichols, B.D., (1981), “Volume of fluid (VOF) method for the dynamics of free boundaries”, J. Comput. Phys., **39**,pp. 201–225.

[51] Hsu, Y.Y., Westwater, J.W., (1960), “Approximate theory for film boiling on vertical surfaces”, Chem. Eng. Progress Symp. Ser. **56**, pp. 15–24.

[52] https://www.thermalfluidscentral.org/encyclopedia/index.php/Pool_Boiling_Regimes

[53] Hua, T.C., Xu, J.J., (2000), “Quenching boiling in subcooled liquid nitrogen for solidification of aqueous materials”, Materials Science and Eng. *A*, **292**, pp.169-172.

[54] Incropera, F., DeWitt, D. P., (1985): Fundamentals of Heat and Mass Transfer, John Wiley &Sons, New York, 317.

[55] Ishigai, S., Nakanishi, S., Ochi, T., (1978), “Boiling heat transfer for a plane water jet impinging on a hot surface”, Proc. 6th Int. Heat Transfer Conf., Toronto, Canada, pp. 445-450.

[56] Islam, A., Monde, M., Woodfield, P. L., and Mitsutake, Y., (2008), “Jet impingement quenching phenomena for hot surfaces well above the limiting temperature for solid–liquid contact”, Int. J. Heat and Mass Transf., **51**, pp. 1226–1237.

[57] Karki, K.C., Patankar, S.V., (1989) "Pressure-based calculation procedure for viscous flows at all speeds in arbitrary configurations", AIAA Journal, **27**, pp. 1167-1174.

[58] Karwa, N., Gambaryan-Roisman, T., Stephan, P., Tropea, C., (2011), “A hydrodynamic model for sub-cooled liquid jet impingement at the Leidenfrost condition”, Int. J. Thermal Sci., **50**, pp. 993-1000.

[59] Kim, J., Huh, C., Kim, M. H., (2007), “On the growth behavior of bubbles during saturated nucleate pool boiling at sub-atmospheric pressure”, Int. J. Heat and Mass Transf., **50**, pp. 3695–3699.

[60] Koldin, A. V., and Platonov, N. I., (2008), “A study of heat transfer in the surface layer of metal during the Impingement of a Liquid Jet”, Therm. Eng., **55**(3), pp. 223–227.

[61] Kromhout, J. A., Kamperman, A. A., Kick, M., Mensonides, F., (2006), Iron making and Steelmaking, **33**, pp. 362–366.

[62] Kraatz, D. B., Mahajan, I. K., "Small hydraulic structures", Food and Agriculture Organisation of the United Nations, Rome 1975.

[63] Launder, B.E. and Spalding, D.B. (1974). "The numerical computation of turbulent flows", Computer Methods in Applied Mechanics and ing, **3** (2), pp. 269–289.

[64] Lienhard IV, J. H., Lienhard V, J. H., 2011, A Heat Transfer Hand Book, 4th Edition, MA: Phlogiston Press, Cambridge, Massachusetts, USA, pp. 269-386.

[65] Liu, Z. D., Fraser, D., Samarasekera, I. V., (2002), "Experimental study and calculation of boiling heat transfer on steel plates during runout table operation", Canadian Metallurgical Quarterly, **41**(1), pp. 63-74.

[66] Liu, X., Lienhard V, J.H., (1993), "The hydraulic jump in circular jet impingement and in other thin liquid films", Experiments in Fluids, **15**, pp. 108-116.

[67] Liu, M-Y., Qiang, A-H., Sun, B-F., (2006), "Chaotic characteristics in an evaporator with a vapor-liquid-solid boiling flow", Chemical Engg. and Processing: Process Intensification, **45**(1), pp. 73-78.

[68] Liu, Z. D., Samarasekera, I.V., (2004), J. Iron Steel Res. Int., **11**, pp. 15–23.

[69] Liu, Z. -H. , Wang, J., (2001), "Study of film boiling heat transfer for water jet impinging on high temperature flat plate", Int. J. Heat and Mass Transf.,**44**, pp. 2475-2481.

[70] Liu, Z. -H., (2003), "Prediction of minimum heat flux for water jet boiling on a hot plate", J. Thermo physics Heat Transfer, **17**(2), pp. 159-165.

[71] Liu, Z. -H., Tong, T-F., Qui, Y-H., (2004), "Critical heat flux of steady boiling for subcooled water jet impingement on the flat stagnation zone", J. Heat Transf., **126**, pp. 179-183.

[72] Liu, Z., Qiu, Y., (2008), "Nucleate boiling on the super hydrophilic surface with a small water impingement jet", International Journal of Heat and Mass Transfer, **51**, pp. 1683-1690.

[73] Liu, Z-.H. , Wang, J., (2001), "Study of film boiling heat transfer for water jet impinging on high temperature flat plate", Int. J. Heat and Mass Transf., **44**, pp. 2475-2481.

[74] Lucas, A., Simon, P., Bourdon, G., Herman, J. C., Riche, P., Neutjens, J., Harlet, P., (2004), Steel Res. Int., **75**, pp. 139–46.

[75] Malmazet, E., Berthoud, G., (2009), “Convection film boiling on horizontal cylinders”, Int. J. Heat and Mass Transf., **52**, pp. 4731–4747.

[76] Mann, M., Stephan, K. Stephan, P., (2000), “Influence of heat conduction in the wall on nucleate boiling heat transfer”, International Journal of Heat and Mass Transfer, **43**, pp. 2193-2203.

[77] Meduri, P. K., Warrier, G. R., Dhir, V. K., (2009), “Wall heat flux partitioning during subcooled forced flow film boiling of water on a vertical surface”, Int. J. Heat and Mass Transf., **52**, pp. 3534–3546.

[78] Mitsutake, Y., Monde, M., (2003), “Ultra high critical heat flux during forced flow boiling heat transfer with an impinging jet”, Transactions of ASME, **125**, pp. 1038–1045.

[79] Miyasaka, Y., Inada, S, and Owase, Y., (1980), “Critical heat flux and subcooled nucleate boiling in transient region between a two-dimensional”, Journal of Chemical Engineering of Japan, **13**(1), pp. 29-35.

[80] Monde, M., (1985), “Critical heat flux in saturated forced convective boiling on a heated disk with an impinging jet a generalized correlation”, Wärme- und Stoffübertragung, **19**, pp. 205-209.

[81] Mozumder, A. K., Monde, M., Woodfield, P. L., Islam, M., A., 2006, “Maximum heat flux in relation to quenching of a high temperature surface with Liquid Jet Impingement”, International Journal of Heat and Mass Transfer, **49**, pp. 2877–2888.

[82] Mozumder, A. K., Woodfield, P. L., Islam, M., A., Monde, M., (2007), “Maximum heat flux propagation velocity during quenching by water jet impingement”, International Journal of Heat and Mass Transfer, **50**, pp. 1559–1568.

[83] Mukherjee, A., Kandlikar, S. G., (2005), “Numerical simulation of growth of a vapour bubble during flow boiling of water in a micro channel”, Microfluid Nanofluid, **1**, pp. 137–145.

[84] Nagendra, H. R., (1971), “Transient-forced convection film boiling on an isothermal flat plate”, NASA TN D-6554.

[85] Nakoryakov, V. E., Pokusaev, B. G., Troyan, E. N., (1978), “Impingement of an axisymmetric liquid jet on a barrier”, Int. J. Heat Mass Transf., **21**, pp. 1175–1184.

[86] Naudascher, E., (1987), “Hydraulik der Gerinne und Gerinnebauwerke”, Springer-Verlag Wien.

[87] Nishio, S., Gotoh, T., Nagai, N., (1998), “Observation of boiling structures in high heat-flux boiling”, Int. J. Heat and Mass Transf., **41**, pp. 3191-3201.

[88] Nukiyama, S., (1934), “Maximum and minimum values of heat q transmitted from metal to boiling water under atmospheric pressure”, J. Japan Soc. Mech. Engrs., 37, pp. 367-374. (Reprinted in Int. J. Heat Mass Transfer, 27(7), pp. 959-970, 1984.)

[89] Ohtake, H., Koizumi, Y., (2004), “Study on propagative collapse of a vapor film in film boiling (mechanism of vapor-film collapse at all temperature above the thermodynamic limit of liquid superheat)”, Int. J. Heat and Mass Transf., **47**, pp. 1965–1977.

[90] Omar, A.M.T., Hamed, M. S., and Shoukri, M., (2009), “Modeling of nucleate boiling heat transfer under an impinging free jet”, Int. J. Heat Mass Transfer, **52**, 5557–5566.

[91] Pan, Y., Stevens, J., Webb, B. W., (1992), “Effect of nozzle configuration on transport in the stagnation zone of axisymmetric, impinging free surface liquid jets. Part 2—Local heat transfer”, J. Heat Transf., **114**, pp. 880–886.

[92] Papell, S. S., (1971), “Film boiling of cryogenic hydrogen during upward and downward flow”, NASA TM X- 67855.

[93] Patankar, S.V., (1980), "Numerical Heat Transfer and Fluid Flow″, McGraw-Hill, New York.

[94] Patankar, S.V., Spalding, D.B., (1972), "A calculation procedure for heat, mass and momentum transfer in three-dimensional parabolic flows", Int. J. Heat Mass Transfer, **15**, pp. 1787-1806.

[95] Peric, M., (1985), "A Finite Volume Method for the Prediction of Three-Dimensional Fluid Flow in Complex Ducts". PhD Thesis, University of London.

[96] Popovac, M., Hanjalic, K. (2005), “Compound Wall Treatment for RANS Computations of Complex Turbulent Flows”: *3rd M.I.T. Conference on Computational Fluid and Solid Mechanics*, Boston.

[97] Qiu, Y-H., Liu, Z-H.,(2005), “Critical heat flux of steady boiling for saturated liquids jet impinging on the stagnation zone”, International Journal of Heat and Mass Transfer, **48**, pp. 4590-4597

[98] Ramstorfer, F., Breistschadel, B., Steiner, H., Bree, G., (2005), “Modelling of the near-wall liquid velocity field in subcooled boiling flow”, Proc. ASME Summer Heat Transfer Conf., San Fransico, CA, July 2005, HT2005-72182.

[99] Ranz, W. E., Marshall, W. R. JR., (1952),"Evaporation from drops", Chemical Engineering Progress, **48**, pp. 141-146.

[100] Rayleigh, L., (1917), “On the pressure developed in a liquid during the collapse of a spherical cavity”, Philos. Mag, 34, pp. 94–98.

[101] Rhie, C.M., Chow, W.L., (1983), "Numerical study of the turbulent flow past an airfoil with trailing edge separation". AIAA J.,**21**, pp. 1525-1532.

[102] Rivallin, J., Viannay, S., (2001), “General Principles of Controlled Water Cooling for Metallurgical on-line Hot Rolling Processes: Forced Flow and Sprayed Surfaces with Film Boiling Regime and Rewetting Phenomena”, Int. J. Therm. Sci., **40**, pp. 263–272.

[103] Robidou, H., Auracher, H., Gardin, P., and Lebouche, M., (2002), Controlled cooling of a hot plate with water jet, Exp. Therm. and Fluid Sci., 26, pp. 123-129.

[104] Ruspini, L.C., Marcel, C. P., Clausse, A., (2014),”Two-phase flow instabilities: A Review”, International Journal of heat and Mass Transfer, **71**, pp. 521-548.

[105] Sakakibara, J., Hishida, K., Maeda, M., (1997), “Vortex structure and heat transfer in the stagnation region of an impinging plane jet (simultaneous measurements of velocity and temperature fields by digital particle image velocimetry and laser-induced fluorescence)”, Int. J. Heat Mass Transfer, **40**, pp. 3163-3176.

[106] Sarma, P.K., Subrahmanyam, T., Rao, V.D., Bergles, A.E., (2001), “Turbulent film boiling on a horizontal cylinder”, Int. J. Heat and Mass Transf., **44**, pp. 207–214.

[107] Seiler-Marie, N., Seiler, J.-M., Simonin, O., (2004), “Transition boiling at jet impingement”, Int. J. Heat and Mass Transf., **47**, pp. 5059–5070.

[108] Sekiguchi, K., Anbe, Y., Imanari, H., (2004), “Temperature control of hot strip finishing mill with inter stand cooling”, Trans. Institute of Electrical Engineers of Japan, **124** (2), pp. 190–95.

[109] Sengupta, J., Thomas, B.G., Wells, M.A., (2005), “Use of water cooling during the continuous casting of steel and aluminum alloys”, Metallurgical and Materials Transactions A-Physical Metallurgy and Material Science, **36A** (1), pp. 187–204.

[110] Shigechi, T., Kawae, N., Tokita, Y., Yamada, T., “Film boiling heat transfer from a horizontal circular plate facing downward”, JSME International Journal, series II, **32**(4), pp. 646-651

[111] Shu, J-.J, and Wilks, G., (2008), “Heat Transfer in the flow of a cold, axisymmetric vertical liquid jet against a hot horizontal plate”, J. Heat Transf., 130, pp. 012202-1– 012202-11.

[112] Smith, A. M. O. and Cebeci, T., (1967), “Numerical solution of the turbulent boundary layer equations”, Douglas aircraft division report DAC-33735.

[113] Smith, M.A., Weinzierl, K., (2007), Iron Steel Technol., **4**, pp. 108–18

[114] Son, G., Dhir, V. K., (1998), “Numerical simulation of film boiling near critical pressures with a level set method”, J. Heat Transf., **120**, pp. 183– 192.

[115] Son, G., Dhir, V. K., (2008), “Three-dimensional simulation of saturated film boiling on a horizontal cylinder”, Int. J. Heat and Mass Transf., **51**, pp. 1156–1167.

[116] Son, G., Ramanujapu, N., Dhir, V. K., (2002), “Numerical simulation of bubble merger process on a single nucleation site during pool nucleate boiling”, J. Heat Transf., **124**, pp. 51- 62.

[117] Stephan, P., Hammer, P., (1994), “A new model for nucleate boiling heat transfer,” Wärme und Stoffübertragung, **30**, pp.119-125.

[118] Stevens, J., Webb, B. W., (1991), “Local heat transfer coefficients under an axisymmetric single-phase liquid jet”, J. Heat Transfer, **113**, pp. 71–78.

[119] Stevens, J., Webb, B. W., (1993), “Measurements of flow structure in the radial layer of impinging free-surface liquid jets”, Int. J. Heat and Mass Transf., **36**(15), pp. 3751-3758.

[120] Sun, C.G., Han, H. N., Lee, J. K., Jin, Y. S., Hwang, S. M., (2002), “A finite element model for the prediction of thermal and metallurgical behavior of strip on run-out-table in hot rolling” ISIJ Int., **42** (4), pp. 392–400.

[121] Suryanarayana, N. V., Merte, H. Jr., (1972), “Film boiling on vertical surfaces”, ASME J. Heat Transfer, **94**, pp. 371–384.

[122] Sweby, P.K., (1984), "High resolution schemes using flux limiters for hyperbolic conservation laws". SIAM Journal Numer. Anal., **21**, pp. 995-1011.

[123] Timm, W., Weinzierl, K. Leipertz, A., (2003), “Heat transfer in subcooled jet impingement boiling at high wall temperatures”, International Journal of Heat and Mass Transfer, **46**, pp. 1385–1393.

[124] Tong, A., (2003), “A Numerical study on the hydrodynamics and heat transfer of a circular liquid jet impinging on to a substrate”, Numerical Heat Transfer Part A, 44, pp. 1-19.

[125] Tsay, J.Y., Yan, Y.Y., Lin, T.F., (1996), “Enhancement of pool boiling heat transfer in a horizontal water layer through surface roughness and screen coverage”, Heat and Mass Transf., **32**, pp.17-26

[126] Ungar, E. K., Eichhorn, R., (1996), “Transition boiling curves in saturated pool boiling from horizontal cylinders”, J. Heat Transfer, 118, pp. 654-661.

[127] Versteeg, H. K. and Malalasekera, W., (1995), “An Introduction to Computational Fluid Dynamics-The finite volume method”, Longman Scientific & Technical.

[128] Wang, X. S., Dagan, Z., and Jiji, L. M., (1989), “Heat transfer between a circular free impinging jet and a solid surface with non-uniform wall temperature or wall heat flux-l. Solution for the stagnation region”, Int. J. Heat and Mass Transf., **32**(7), pp. 1351-1360

[129] Wang, X., and Monde, M., (1997), “Critical heat flux in forced convective subcooled boiling with a plane wall jet (effect of subcooling on CHF)”, Heat and Mass Transf., **33**, pp. 167– 175.

[130] Wang, X., Monde, M., (2000), “Critical heat flux in forced convective subcooled boiling with a plane jet (Revised correlation for saturation condition)”, Heat and Mass Transf., **36**, pp. 97- 101

[131] Warming, R.F., Beam, R.M., (1976) “Upwind Second Order Difference Schemes and Applications in Aerodynamic Flow.” AIAA J., **14**, pp. 1241-1249

[132] Watson, E. J., (1964), “The radial spread of a liquid jet over a horizontal plane”, J. Fluid Mech., **20**, pp. 481–495

[133] Witte, L. C., Lienhard, J. H., (1982), “On the existence of two transition boiling curves”, Int. J. Heat Mass Transfer, **25**, pp. 771-779.

[134] Wolf, D. H., Viskanta, R., Incropera, F. P., (1990), “Local convective heat transfer from a heated surface to a planar jet of water with a non-uniform velocity profile”, J. Heat Transf. **112**, pp. 899–905

[135] Wolf, D. H., Viskanta, R., Incropera, F.P., (1995), “Turbulence dissipation in a free-surface jet of water and its effect on local Impingement Heat Transfer from a Heated Surface: Part 2---Local Heat Transfer”, J. Heat Transf, **117**, pp. 95-103.

[136] Woodfield, P. L., Monde, M., Mozumder, A. K., (2005), “Observations of high temperature impinging-jet boiling phenomena”, Int. J. Heat Mass Transf, **48**, pp.2032–2041.

[137] Yakhot, V., Orszag, S.A., Thangam, S., Gatski, T.B. & Speziale, C.G. (1992), "Development of turbulence models for shear flows by a double expansion technique", Physics of Fluids A, **4** (7), pp. 1510-1520.

[138] Yaminsky, V.V., (2006), “Bubble vortex at surfaces of evaporating liquids”, Journal of Colloid and Interface Science, **297** (1), pp. 251-260.

[139] Yuan, M. H., Yang, Y. H., Li, T. S., Hu, Z. H., (2008), “Numerical simulation of film boiling on a sphere with a volume of fluid interface tracking method”, Int. J. Heat and Mass Transf., **51**, pp. 1646–1657.

[140] Zuber, N., (1958), “On the stability of boiling heat transfer”, Trans ASME, **80**, pp. 711-720.

[141] Zürcher, O., Thome, J. R. Favrat, D., (2000), “An onset of nucleate boiling criterion for horizontal flow Boiling”, Int. J. Therm. Sci. **39**, pp. 909–918.

[142] Zumbrunnen, D. A., (1991), “Convective heat and mass transfer in the stagnation region of a laminar planar jet impinging on a moving surface”, J. Heat Transf., **113**, pp. 563–570.

[143] Zumbrunnen, D. A., Incropera, F. P., Viskanta, R., (1992), “A laminar boundary layer model of heat transfer due to a non-uniform planar jet impinging on a moving plate”, Wärme- und Stofffübertragung, **27**, pp. 311-319.

Appendix

Boundary layer profile at different time level at different locations of the plate are given in the Figure 71-72.

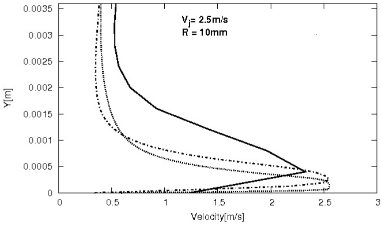

Figure 71 – Boundary layer profile at Solid-Line (–) 10.0 s, dash-dot-dash (-.-) 10.5 s, dot-dot (.....) 11.0 s

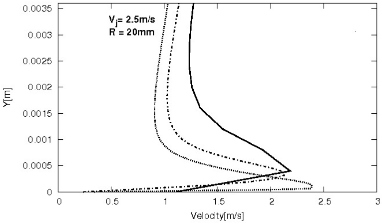

Figure 72 – Boundary layer profile at Solid-Line (–) 20.0 s, dash-dot-dash (-.-) 20.5 s, dot-dot (...) 21.0 s

Turbulent kinetic energy at different time level at different locations of the plate are given in the Figure 73-75.

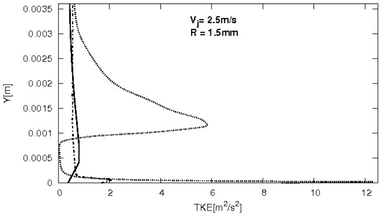

Figure 73 – TKE at Solid-Line (–) 1.5s, dash-dot-dash (-.-) 2.0s, dot-dot (.....) 2.5s

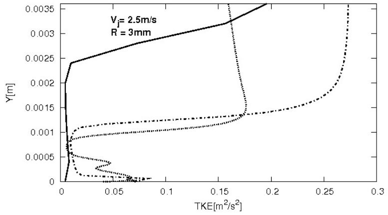

Figure 74 – TKE at Solid-Line (–) 3.0s, dash-dot-dash(-.-) 3.5s, dot-dot (.....) 4.0s

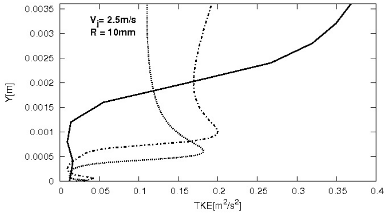

Figure 75 – TKE at Solid-Line (–) 10.0s, dash-dot-dash (-.-) 10.5s, dot-dot (.....) 11.0s

Cooling of the surface with respect to time at different locations are given in the Figure 76.

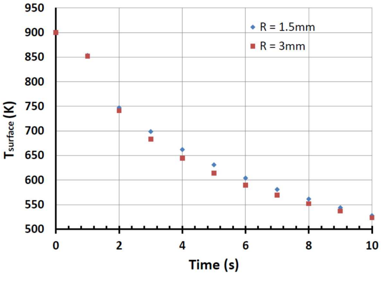

Figure 76 – Cooling curve for the jet velocity 2.5 m/s and initial temperature of the plate is 900 K

The details of the boiling curves for the wall-superheat at 700 K and jet velocity 2.5 m/s are given in Figure 77 (a-b). The wall-superheat of critical heat flux is 850 K for the boiling at stagnation region, but for the acceleration region of the jet is more than 850 K. Since, the sub-cooling of the liquid increases as the flow and boiling-front progress to downstream. At the wall jet region (r > 4 mm), the influence of the liquid sub-cooling is less and shows less variation of the critical wall superheat. Such type of behavior is also seen in some experimental data of Gradeck et al., 2009.

The boiling curve at the wall jet region shows the shoulder of heat flux at the critical wall-superheat.

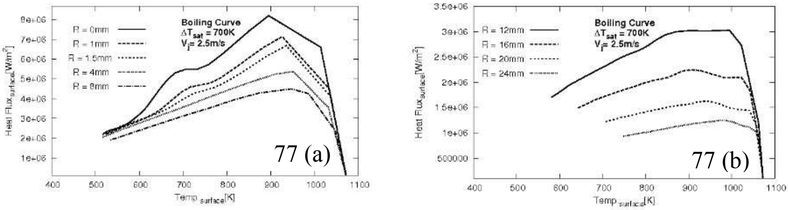

Figure 77 (a-b) – Boiling curves at wall-superheat 700 K and jet velocity 2.5 m/s and water sub-cooling temperature 45 K

Further improvements in the quenching model can be done through incorporations of the artificial surface roughness in the wall-function in order to mimic the bubble formation, merger, and collapse mechanism at the vicinity of the surface during the quenching process.

Hydraulic jump positions for the moving surface are shown in the following Figures A8.

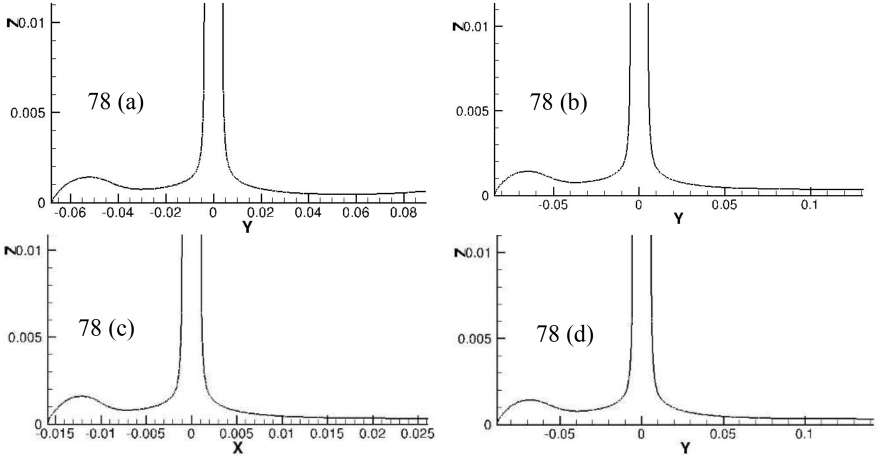

Figure 78 (a-d) – Iso-surface of the hydraulic jump for the moving surface

Lebenslauf

Persönliche Daten

Name: Maharshi Subhash

Adresse: House Number-727, Lane Nr. 7
Lajpat Rai Marg, Subhash nagar
Dehradun-248002, Uttarakhand, India.

E-mail: maharshisubhash@gmail.com
Geburtsdatum, Ort: 25.03.1983, India
Familienstand: verheiratet, since 2011
Sprachen: English, German (very basic), Italian (A1 level), Hindi

Studium und Arbeitserfahrung

Seit 07/2015	*Assistant Professor*, *Department of Mechanical and Automobile Engg*. Graphic Era University, Dehradun-248002, India
12/2012 – 06/2015	University of Modena and Reggio Emilia, *Research Associate in Department of Science and Methods in Engg. Responsible for design of ACHEON Nozzle for Novel Propulsion system for V/STOL funded by 7th Framework program of EU (European Union)*
06/2008 – 03/2012	Technische Universität Darmstadt *Wissenschaftlicher Mitarbeiter am Fachgebiet für Strömungslehre und Aerodynamik (SLA)*
07/2007 – 05/2008	University of Petroleum and Energy Studies, India *Lecturer, courses taught Aerodynamics I, IC Engine, Transport Phenomena,and Fluidization and Mixing*
07/2005 – 06/2007	Indian Institute of Technology Roorkee, India *Chemical Engg.(Spl. CFD) (M.Tech)9.18/10*
10/2001 – 06/2005	Azad Institute of Engg. & Tech. Lucknow, India *Mechanical Engg. (B.Tech First Honours) 79%*